

Copyright

by

Vikram Gopalakrishnan Sundararajan

2010

**The Thesis Committee for Vikram Gopalakrishnan Sundararajan  
Certifies that this is the approved version of the following thesis:**

**Topology Optimization for Additive Manufacturing of Customized  
Meso-Structures using Homogenization and Parametric Smoothing  
Functions**

**APPROVED BY  
SUPERVISING COMMITTEE:**

**Supervisor:**

---

Carolyn C. Seepersad

---

Richard H. Crawford

**Topology Optimization for Additive Manufacturing of Customized  
Meso-Structures using Homogenization and Parametric Smoothing  
Functions**

**by**

**Vikram Gopalakrishnan Sundararajan, B.E.**

**Thesis**

Presented to the Faculty of the Graduate School of

The University of Texas at Austin

in Partial Fulfillment

of the Requirements

for the Degree of

**Master of Science in Engineering**

**The University of Texas at Austin**

**December 2010**

## **Dedication**

To my mother Sitalakshmi Sundararajan and late father Sundararajan Tiruvengadam for their blessing, love and support.

## **Acknowledgements**

I would like to thank my advisor, Dr. Carolyn C. Seepersad for her extraordinary dedication and invaluable suggestions to help me reach where I am today. She has been a constant source of inspiration for me to work harder towards the goals of my thesis in the past two years.

I would, also, like to thank Dr. Richard Crawford for his patience with my questions on parametric curves and valuable suggestions that have helped me improve the contents of this thesis.

Charlie Manion for his dedication and assistance with the fabrication and experimental testing aspects of this project.

I am grateful to Mark E. Phillips for training me on the SLS machine and Danny Jares for his ideas on experimental set up and metrology associated with this work.

I would finally like to thank my lab mates at the PPMD lab, David Shahan, Andrew Tilstra, Pete Backlund, Cassandra Telenko, Nathan Putnam, Matt Saunders, Ray Ely, Lia Kashdan, Julia Rourke, Danny Johnson and Jordan Mathews whose friendly character and useful feedback have gone a long way in keeping me enthusiastic about my work.

December 3, 2010

## **Abstract**

# **Topology Optimization for Additive Manufacturing of Customized Meso-Structures using Homogenization and Parametric Smoothing Functions**

Vikram Gopalakrishnan Sundararajan, M.S.E

The University of Texas at Austin, 2010

Supervisor: Carolyn Conner Seepersad

Topology optimization tools are useful for distributing material in a geometric domain to match targets for mass, displacement, structural stiffness, and other characteristics as closely as possible. Topology optimization tools are especially applicable to additive manufacturing applications, which provide nearly unlimited freedom for customizing the internal and external architecture of a part. Existing topology optimization tools, however, do not take full advantage of the capabilities of additive manufacturing. Prominent tools use micro- or meso-scale voids or artificial materials to parameterize the topology optimization problem, but they use filters, penalization functions, and other schemes to force convergence to regions of fully dense (solid) material and fully void (open) space in the final structure as a means of

accommodating conventional manufacturing processes. Since additive manufacturing processes are capable of fabricating intermediate densities (e.g., via porous mesostructures), significant performance advantages could be achieved by preserving and exploiting those features during the topology optimization process. Towards this goal, a topology optimization tool has been created by combining homogenization with parametric smoothing functions. Rectangular mesoscale voids are used to represent material topology. Homogenization is used to analyze its properties. B-spline based parametric smoothing functions are used to control the size of the voids throughout the design domain, thereby smoothing the topology and reducing the number of required design variables relative to homogenization-based approaches. Resulting designs are fabricated with selective laser sintering technology, and their geometric and elastic properties are evaluated experimentally.

## Table of Contents

List of Tables .....	xi
List of Figures .....	xii
Chapter 1: Additive Manufacturing and its Implications for Product Design – An Overview .....	1
1.1 Motivation for the Proposed Research.....	1
1.2 Chapter Objectives.....	1
1.3 Introduction to Additive Manufacturing.....	2
1.3 Popular AM Methods.....	3
1.4 Selective Laser Sintering (SLS).....	4
1.5 Advantages of SLS Over Other Methods .....	7
1.6 Design Customization Using SLS .....	7
1.7 Design Tool with Material Mesostructure Parameters .....	10
1.8 Problems with Existing Design Tools.....	11
1.9 Research Objectives.....	12
1.10 Thesis Overview .....	13
Chapter 2: Topology optimization for Designed Meso-structure .....	15
2.1 Chapter Objectives.....	15
2.2. Introduction to Topology Optimization .....	15
2.3 Topology Optimization Methods.....	17
2.4 Homogenization – The Selected Approach for Mesostructure Design ..	31
2.5 Literature Review on Design Methodologies for Customized Mesostructures .....	32
2.6 Summary .....	34
Chapter 3: Homogenization with Design Variable Reduction – Theory and Implementation Details .....	35
3.1 Chapter Objectives.....	35
3.2 Theory of Homogenization .....	36
3.3 Relating Homogenized Model with Macroscopic Equilibrium Equations	45



3.4 Validation of Derived Homogeneous Coefficients.....	53
3.5 Design Variable Reduction Using a Parametric Scheme on the Homogenization Approach.....	59
3.6 Summary.....	73
Chapter 4: Design Optimization by Homogenization – Problem cases, Solutions and Results.....	74
4.1 Chapter Objectives.....	74
4.2 Problem Selection for Design Optimization.....	74
4.3 Description of the Test Problems.....	75
4.4 Optimization Setup for Test Problems.....	77
4.5 Performance Evaluation of Solutions From the Homogenization Routine.....	88
4.6 Verification of Deformation Displacement with Ansys Models.....	92
4.7 Summary.....	96
Chapter 5: Fabrication of Designed Mesostructure through SLS and Experimental Testing of Parts – Details and Results.....	98
5.1 Chapter Objectives.....	98
5.2 Conversion of Design Solutions to CAD Models.....	98
5.3 Design for Fabrication and Testing.....	101
5.4 Final Dimensions of Fabricated Parts.....	113
5.5 Fabricated Parts.....	114
5.6 Experimental Testing Results.....	117
5.8 Summary.....	123
Chapter 6: Conclusions and Directions for Future Work.....	125
6.1 Summary of Contributions.....	125
6.2 Unresolved Issues Associated with the Current Work.....	129
6.3 Avenues for Future Work.....	130

Appendix A.....	131
Appendix B.....	134
References.....	154
Vita.....	161

## List of Tables

Table 3.1: Derived symmetric stiffness matrix terms for a rectangular element.....	50
Table 3.2: Comparison of computed coefficients with results of the HOMOG code [68] for plane stress 2D model .....	54
Table 4.1 Summary of the problem parameters for the optimization routine.....	88
Table 4.2: Comparison of design solutions – SIMP vs. HOMOG with B-Spline .....	90
Table 4.3: Performance parameters of SIMP solution recomputed on HOMOG-B analysis routine .....	91
Table 4.2 Verification of results – ANSYS & MATLAB .....	95
Table 5.1: Sinterstation HiQ build parameters for Nylon-11 powder .....	103
Table 5.2: Results of the experimental study.....	104
Table 5.3: Load – Displacement results for experimentally tested parts.....	119

## List of Figures

Figure 1.1: Schematic Sketch of SLS (Bourell 1990).....	5
Figure 1.2: Parts from the SLS machine [21, 22 & 23].....	6
Figure 1.3 Cell structures studied by Cheah a) three hexagonal prisms b) five rhombic decahedrons.....	8
Figure 1.4: Examples of material design through cellular topologies [29, 30 & 31] .....	9
Figure 1.5: Design Tool accommodation for SLS capabilities – a) conventional truss type topology b) Topology with material mesostructure.....	10
Figure 2.1: Shape variation without topology change [33].....	15
Figure 2.2: Inputs for a topology optimization procedure .....	16
Figure 2.3: A cantilever beam optimized for b) 80% c) 60% d) 40% and e) 20% volume fractions [32].....	17
Figure 2.4: Ground structures for an 8 x 6 nodal layout of a plane truss a) neighbors connected – 137 links b) all possible connections – 730 links [38].....	19
Figure 2.5: Construction of a rank-2 layered material [43] .....	24
Figure 2.6: a) A square unit cell with 60° hole orientation b) A grid with a square unit cell at 0° hole orientation .....	24
Figure 2.7: Schematic showing the definition of level set function in the design domain.....	26
Figure 2.8: Chromosome array mapping to a topology .....	30
Figure 3.1: A locally periodic function on the macro( $x$ ) and meso( $x$ ) scales [43].....	37
Figure 3.2: Plane elasticity element showing the stress component directions .....	39
Figure 3.3: Normal loading and boundary conditions to determine $E_1^H$ and $\nu_{12}^H$ .....	41
Figure 3.4: Shear loading and boundary conditions to determine $G_{12}^H$ .....	42
Figure 3.6: Mesostructure unit for density calculation .....	43
Figure 3.7: Square grid – a) Homogenized model b) ANSYS model with a zoomed view of the elements in the solid regions.....	55
Figure 3.8: Error in maximum displacement of the homogenized model measured against the ANSYS model of the same problem for plane strain assumption .....	56
Figure 3.9: Error in maximum displacement of the homogenized model measured against the low density model of the same problem for plane strain assumption.....	58
Figure 3.10: Classification of parametric surfaces .....	61
Figure 3.11 A B-spline surface with its control points and control polygon [73] .....	62
Figure 3.12 Two surfaces with the same control net and order but different parameter values in their knot vectors a) open uniform - [0 0 0 0 1 2 2 2 2] b) periodic non uniform – [0 1 2 3 4 5 5 5 5].....	66
Figure 3.13 Measuring densities as surface heights from a datum plane at $z=0$ .....	67
Figure 4.1: A simply supported beam – MBB problem.....	76
Figure 4.2: Symmetric half beam – MBB problem .....	76
Figure 4.3: Cantilever beam problem .....	77
Figure 4.4 Steps in the optimization procedure .....	80
Figure 4.5: Steps in optimization with the B-spline smoothing scheme.....	81
Figure 4.6: Minimum density mesostructure units possible on the SLS .....	85

Figure 4.7: SIMP solution for the MBB beam problem – Full beam and half beam.....	88
Figure 4.8: Homogenization with B-spline smoothing solution for the MBB beam problem – Full beam and half beam.....	89
Figure 4.9 Cantilever problem – a) Homogenization with B-spline smoothing solution (Homog-B) b) SIMP solution .....	90
Figure 4.10 Density to mesostructure geometry conversion .....	93
Figure 4.11 ANSYS MBB Models a) HOMOG b) SIMP .....	94
Figure 4.12 ANSYS Cantilever Models a) HOMOG b) SIMP .....	95
Figure 5.1: Steps in the conversion of Optimization results to CAD model – Illustration with an MBB case.....	99
Figure 5.2 CAD models for the SIMP and the HOMOG-B design methods – MBB beam .....	100
Figure 5.3: CAD models for the SIMP and the HOMOG-B design methods – Cantilever beam.....	101
Figure 5.4: Sinterstation HiQ machine showing build chamber view direction adopted in this work.....	102
Figure 5.5: Sample specimens (top) and their zoomed views (below) with their relative orientations in the build chamber indicated by matching numbers .....	103
Figure 5.6: Smallest achievable density for 5mm mesostructure unit size.....	105
Figure 5.7 Schematic sketch of the MBB beam with mounts for the experimental study on hole size deviations .....	106
Figure 5.8: Error in measured hole sizes on the actual part against the CAD model for different hole size ranges .....	107
Figure 5.9: Test part on the Instron 3-point bending equipment .....	108
Figure 5.10: Comparison of numerical routines with experimental values for the MBB beam in the hole size deviation study .....	109
Figure 5.11: Mount designs for the MBB beam .....	110
Figure 5.12 Test set up equipment – Dial Indicator, MBB SIMP case and weights .....	111
Figure 5.13: Front view of the provision for clamping space at the left end and top view of the load mount design at the right end of the cantilever beam .....	112
Figure 5.14: Cantilever beam test set up – Dial Indicator, Vise blocks, weights and clamp at the top.....	112
Figure 5.15: Dimensions of the MBB beam – SIMP and HOMOG-B.....	113
Figure 5.16: Dimensions of the Cantilever beam – SIMP and HOMOG-B.....	114
Figure 5.17 Arrangement of parts in the build chamber.....	115
Figure 5.18: Fabricated parts - Cantilever, MBB beams and Tensile specimens .....	116
Figure 5.19: Schematic for orientation of tensile specimens inside the build chamber .	117
Figure 5.20: Tensile test results giving young’s modulus for the specimens .....	118
Figure 5.21: Comparison of experimental results with numerical models .....	121
Figure 5.22: Error percentage results for different cases against numerical models .....	122

# **Chapter 1: Additive Manufacturing and its Implications for Product Design – An Overview**

## **1.1 MOTIVATION FOR THE PROPOSED RESEARCH**

Engineering design has historically been focused on furnishing design solutions that are amenable to conventional manufacturing practices. In the last two decades, state of the art manufacturing methods based on additive manufacturing techniques have gained prominence and broadened the scope of feasible part geometries. It is now possible to introduce designed microstructure and mesostructure (an identifiable pattern in the millimeter scale) into part designs with the help of additive manufacturing methods – a capability that was not available with conventional fabrication techniques. Therefore, design engineers are no longer constrained to simplified geometries. This expanded design search space made available to design engineers cannot be capitalized upon until design tools are updated to keep pace with the advancements in the manufacturing area.

It is the aim of this research to develop a design tool that can help a designer tailor material meso-structure and investigate the potential benefits for product design of this leap in fabrication capabilities offered by additive manufacturing.

## **1.2 CHAPTER OBJECTIVES**

An overview of additive manufacturing is provided followed by a discussion on the SLS manufacturing process. The capabilities of SLS for novel material designs are described and the need for design tools that take advantage of these strengths are highlighted in this chapter. Finally, a set of research objectives to be addressed in this work are provided.

### **1.3 INTRODUCTION TO ADDITIVE MANUFACTURING**

Additive Manufacturing (AM) refers to all those techniques where a component is fabricated incrementally by adding material to conform to the geometry of the part specified in a CAD model without any need for custom tools or dies [79]. In contrast, traditional material removal methods (turning, milling etc.) and manufacturing techniques apply force or heat to deform a material (forging, casting, drawing or extrusion). AM has also been frequently referred to by other terms – Additive Fabrication, Solid Freeform Fabrication, Rapid Prototyping (RP) and Desktop Manufacturing. The greatest advantages are the quick turn around and minimal scrap, if any. More importantly, they have negligible production set up time for design changes in the part, making them well suited for prototyping applications. These techniques introduced in the 1980s have since seen rapid progress both in terms of commercial acceptance and applicability to wide areas. From fragile prototypes to evaluate the look and feel of the product in the early 90s, contemporary applications include functional models, patterns for tooling & metal castings and even non-engineering applications like skeletal models for aiding physicians before surgical operations.

Many methods of AM have been tested and improved but the most popular techniques that survived the rigors of market expectations include Stereolithography (SLA), Selective Laser Sintering (SLS), 3D Printing (3DP) and Fused Deposition Modeling (FDM). Details of other RP techniques such as Laminated Object Manufacturing (LOM), Solid Ground Curing (SGC), Ballistic Particle Manufacturing (BPM), Ink Jet Printing (IJP) etc. can be found in [1, 2 & 3].

The basic idea in AM is to start from a base material that could be in a solid, powder, liquid or resin form and selectively process it by means of light, heat, or adhesion to take the shape of the part to be fabricated. Selective laser sintering (SLS) is

the method of fabrication used in this work. A brief overview of the other methods - SLA, FDM & 3D printing are presented before discussing SLS in detail.

### **1.3 POPULAR AM METHODS**

Stereolithography (SLA) [4], a technique successfully commercialized by 3D Systems in 1986, involves the photo-polymerization of a liquid resin layer on a platform by UV light. After one layer thickness of the resin has been cured by a UV laser beam, the next layer of resin to be cured is added onto the top of the present layer by moving the platform down with the help of a programmed actuator. The strength of stereolithography lies in its ability to build parts accurately with details on the order of a few micrometers (by a two photon polymerization process), a feature that is not possible with other techniques [5]. Stereolithography is also superior to other AM methods in providing a very smooth surface finish. The biggest limitation of stereolithography lies in the limited choice of materials it can process.

Fused deposition modeling (FDM) is a non-laser based technique patented in 1989 by Scott Crump [6] of Stratasys, Inc. The apparatus works on the idea of depositing a layer of molten material on to a base plate that solidifies quickly and allows subsequent layers of material to adhere and solidify onto the first layer, forming the part in the process. The material is brought to its molten state by means of an electric heater inside a dispensing head that leads up to a dispensing nozzle to deposit the material layer. The dispensing head is fed with a reel of the solid material from a spool at a controlled rate. The success of FDM lies in the ability to guard the temperature of the molten fluid to within a narrow limit above the molten temperature, so that the material is not too viscous and can be quickly cooled to solidification temperature. The advantage of FDM is that it



is tidy, representing the closest AM process that is truly oriented towards desktop manufacturing. It uses cheap, non-toxic, biodegradable materials and supports different colors for the fabricated parts. The most striking limitations of FDM are the poor surface finish of the fabricated parts and the directional dependence of the material properties. Further, there are a number of FDM characteristic errors that need careful tuning of the process parameters [7].

3D Printing (3DP) was patented in 1994 by Sachs *et al.* [8]. This method operated on the principle of binding a layer of powder with a binder that was printed in the form of a jet in accordance to the geometry of the part specified in the CAD model. Soligen was the first manufacturer to successfully convert this idea into a marketable product for application in fabrication of prototypes for production tooling. The apparatus consists of a feed mechanism for the powder on the bottom plate and an inkjet head that can move in the x-y direction to spray the binder. A piston allows for the z-movement of the part bed. The powder, unaffected by the binder, serves as temporary support before it is removed in the post-processing stage. Usually, the powder that is held by the binder is heated to give more stability to the part. The biggest advantage of 3DP is its ability to process metals and at a rate much faster than other methods, although a post-processing sintering step is required. Colored parts are achieved very easily with 3DP because color can be applied directly to the binder fluid as opposed to a separate coloring stage in other techniques [9].

#### **1.4 SELECTIVE LASER SINTERING (SLS)**

Selective laser sintering, a technique patented in 1988 by Deckard [10], involves the application of a laser beam (CO<sub>2</sub>) to sinter (fuse) powder particles of a particular

layer. From the second layer onwards each layer is further fused to bond with powder of the preceding layer in accordance to the geometry specified in the CAD model. There are two pistons – one to hold the part and the other to feed more powder for successive layers. A roller drum helps feed powder from the second piston onto the first. The part bed is initially heated to a temperature close to the melting temperature of the powder before the laser starts scanning the powder layers. This minimizes large stresses from thermal gradients on successive layers as they are being sintered. Radiant heat panels are usually mounted around the powder bed to raise the temperature of the powder bed. Once the part has been fabricated and cooled, unsintered powder can be removed in the post-processing stage. A schematic sketch is shown in Figure 1.1.

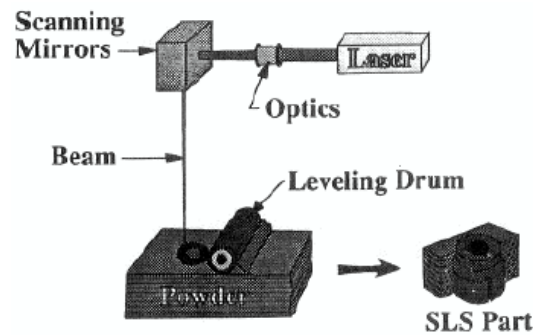


Figure 1.1: Schematic Sketch of SLS (Bourell 1990)

One of the greatest advantages of SLS is its flexibility for processing a wide range of materials. SLS has been successfully used with polymers, polyamides, ceramics and metals [11 & 12]. SLS is capable of producing functional parts with sound mechanical characteristics very close to that achieved by conventional manufacturing techniques. One of the major concerns with SLS is part accuracy. Accuracy is affected by a number

of process parameters like laser scan speed, powder bead temperature profile, powder condition, shrinkage etc., each of which is being actively studied [13, 14, 15 & 16]. While laboratory fabrication allows for careful control of these parameters and production of multiple test parts to get the best part quality, successful commercialization of SLS depends on the ability to produce high accuracy functional parts consistently for any geometric shape [17]. Thus, robust computer models that can relieve a user of the skill and expertise to set up appropriate process parameters for improving part accuracy are being developed [18 & 19]. Other limitations of SLS include the need to sieve powder agglomerates to prepare them to be recycled, post process parts to improve surface finish, and long hours to cool parts for certain materials like wax [17 & 20].

SLS parts find applications in automotive and aerospace industry, tissue engineering, tooling inserts, tools for injection molding and die casting applications. Some applications are shown in Figure 1.2.

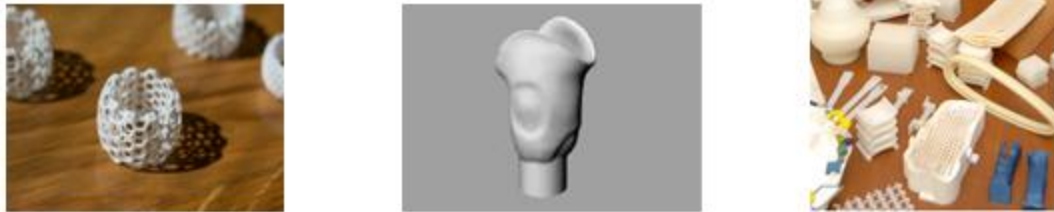


Figure 1.2: Parts from the SLS machine [21, 22 & 23]

The first image shows a jewelry prototype fabricated using the SLS technique for an individual user by Shapeways, representing a typical RP production service business concept. The second image shows a functional model of a compliant below-the-knee prosthetic developed at the University of Texas at Austin. The third image shows a

number of models – a foot pedal, an airfoil cross-section etc. fabricated as a part of class projects at the University of Texas at Austin using the SLS technique.

### **1.5 ADVANTAGES OF SLS OVER OTHER METHODS**

Of the four methods – SLA, SLS, FDM and 3DP, 3DP is fairly new and relatively less mature. Both SLA and FDM are constrained by the range of materials that they can process. It turns out that different grades of commercially available Nylon powder that SLS can process have very good properties for fabricating functional parts. Further, there is extensive research available on the errors encountered in the SLS process and most of these can be anticipated and accounted for by fine tuning the process parameters [13]. Since the goal of this research is to study design improvements for functional parts, SLS, being one of the well studied methods for creating functional parts, is selected as the method of fabrication for all design solutions in this work.

### **1.6 DESIGN CUSTOMIZATION USING SLS**

Custom complicated geometries are easily produced in SLS. In conventional manufacturing, cost is directly related to the complexity of part design, but, in SLS cost is more directly related to the volume of the part than its complexity. This eliminates the “design for manufacture” constraint on the designer, making it convenient for him/her to be more imaginative and generate designs that exploit the capabilities of SLS [24]. In fact, the designer can lay down different functional specifications for the same part at different regions because it is possible to tailor the part to be relatively strong or compliant in different areas.

SLS allows material composition to be controlled or a characteristic microstructure to be built into the geometry of the part to achieve spatial variation of properties within the structure. Since the dimensions of characteristic structure are on the order of a couple of hundred micro meters, it is appropriate to shed the micro prefix and introduce a meso prefix to the scale under discussion. For the rest of the thesis, the material architecture is referred to by the term material mesostructure. The goal of finding a suitable structure for a desired functional performance is now a material geometry design optimization problem. This idea was discussed by Crawford *et al.* [25]. Tissue engineering specialists were quick to leverage this theme and Cheah *et al.* showed the effectiveness of SLS in fabricating scaffolds with prescribed strength and stiffness properties [26, 27 & 28]. Some cell structures used by Cheah *et al.* are shown in Figure 1.3.



Figure 1.3 Cell structures studied by Cheah a) three hexagonal prisms b) five rhombic decahedrons

Although there was a latent need for a convenient manufacturing process to design porous structures that mimic bone tissues of the human body, there is no reason why material geometry design should be limited to tissue engineering applications. It could be extended to aerospace, structural, automobile and other engineering applications. The power of CAD tools combined with the availability of SLS for

controlled mesostructure that can operate directly on CAD files prove to be a boon for design engineers grappling with the need for a sophisticated manufacturing technology for manipulating material internal architecture.

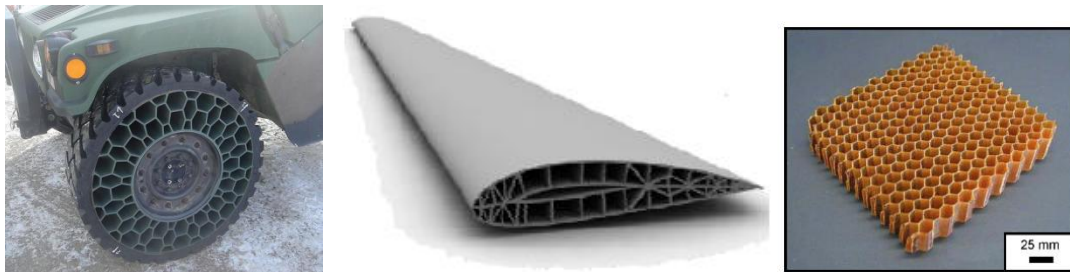


Figure 1.4: Examples of material design through cellular topologies [29, 30 & 31]

The first image in Figure 1.4 shows a macrostructure built of hexagonal cell structures that serve to withstand the tough riding conditions for a military vehicle without requiring air for inflation. The second image is that of a deployable wing structure for an unmanned aerial vehicle built using lattice skins through SLS fabrication. The third image is that of a sandwich core structure using miniature cell structures for increased impact energy absorption.

From the examples above, it is very clear that there is a definite advantage in organizing material systematically at small length scales and the improved strength characteristics obtained from such an arrangement were studied in [30]. The structures shown above in Figure 1.4 can be categorized as cellular structures because of their thin walls although SLS has no necessity to conform to the thin wall requirements of cellular structures. Walls could be made thick or thin as desired. Designers can choose to disperse both thin and thick walls within the design domain if needed. This flexibility enables designers to move from macro scale features to meso scale designs in a seamless fashion to meet performance objectives within the design region.

## 1.7 DESIGN TOOL WITH MATERIAL MESOSTRUCTURE PARAMETERS

The design community is now facing the challenge of exploiting the far reaching capabilities of SLS and updating its tools to provide tailored mesostructures as solutions to a wide variety of engineering problems. The new design tool should be capable of distributing material inside the design domain without the need for a truss type topology separating solid from void shown in Figure 1.5.

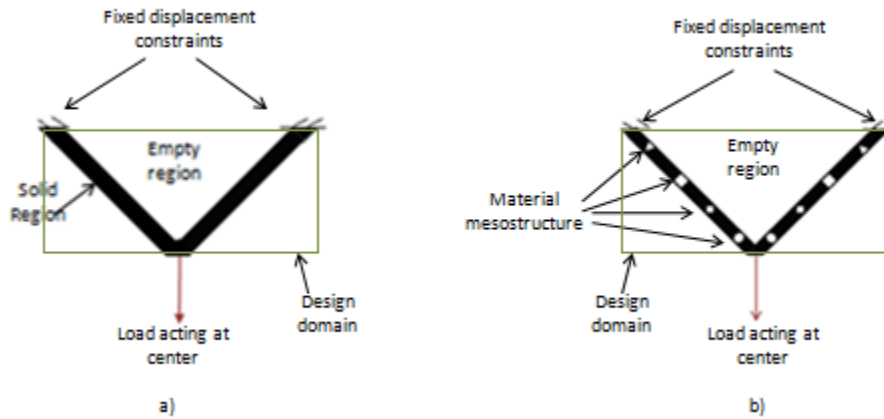


Figure 1.5: Design Tool accommodation for SLS capabilities – a) conventional truss type topology b) Topology with material mesostructure

The requirements for the improved design tool can be summarized as follows:

1. Determine strategic areas where material will be distributed to maximize performance
2. Distribute material in quantities of a repeatable mesostructure unit.
3. Allow the mesostructure units to be porous with pore or hole sizes ranging from zero to the size of the mesostructure unit itself. This results in the ability to construct a solid design region by distributing solid through the entire mesostructure and a void region by distributing no material inside the

mesostructure. Characteristic structure with hole sizes in the intermediate range clearly is the distinguishing feature of this tool that requires SLS capabilities.

4. Treat the shape and orientation of the hole inside the mesostructure as variables that can be captured from a set of standard options – square, hexagon, triangle etc. for shapes and  $0^\circ$ ,  $60^\circ$ ,  $90^\circ$ ,  $120^\circ$  etc. for orientation.
5. Allow material properties to be expressed as a function of the geometry of the mesostructure. This is referred to in the literature as parameterizing the material domain. A solid mesostructure will have the properties of the material used in the SLS process whereas porous mesostructures will have different properties based on the shape and size of the holes or pores.

## **1.8 PROBLEMS WITH EXISTING DESIGN TOOLS**

Conventional design tools fail to account for variable mesostructure in the final part because the solutions were intended for traditional manufacturing methods. The most relevant tools for mesostructure design are based on “topology optimization” methods. In particular, there are approaches within topology optimization (SIMP and homogenization) that support the material parameterization concept discussed in section 1.7. Details of these methods are provided in subsequent chapters. For the purpose of the discussion here, it is important to know that these approaches implement a heavy penalization scheme for intermediate densities or pore/hole sizes in the final stage of optimization, thus forcing the design solutions to segregate fully into solid and fully void regions as shown in Figure 1.5a manufacturable with subtractive processes. It is this



penalization that has to be eliminated so as to customize the design tool to reflect SLS capabilities.

## **1.9 RESEARCH OBJECTIVES**

The development of the design tool for all class of engineering problems using the set of all possible mesostructure shapes and orientations is beyond the scope of this work. This work is limited to one single mesostructure shape and orientation – square mesostructure with  $0^\circ$  hole orientation and is applied to a single application problem – plane elasticity.

The first objective of this research is to develop an equivalent material model for the square mesostructure. This equivalent material model possesses the capability to express material properties of interest in a plane elasticity problem as a function of the size of the square hole within the square mesostructure unit. This is called the homogenized material model. The model is validated with sample problems and by comparing model coefficients determined by previous authors in this field.

The second objective of this research is to employ these computed equivalent properties from the homogenized material model in an optimization routine to obtain mesostructure design solutions for standard beam problems. It is the hypothesis of this research that improved design solutions can be obtained by designing the mesostructure, rather than just the macrostructure. The two categories of designs are generated, and their elastic structural properties are compared to investigate the hypothesis.

The third objective of this research is to study the fabrication characteristics of SLS for mesostructure designs and validate the calculations of the developed design tool through experimental testing. The dimensional accuracy of the parts from SLS is

measured and mechanical behavior under different loads from experimental testing is compared with the numerical results from the design tool.

## **1.10 THESIS OVERVIEW**

This thesis consists of six chapters. In chapter one, the research is motivated, including an introduction to additive manufacturing and a discussion of, - the opportunities for novel design capabilities with SLS fabrication, the problems with existing design tools, the requirements of an updated design tool, and the resulting research objectives.

In chapter two, a detailed review of the current design methodologies based on topology optimization is provided. The suitability of the approaches in topology optimization for additive manufacturing based designs is discussed. A literature review of current design methodologies for customized mesostructure designs fabricated with AM techniques is provided in this chapter. The inherent drawbacks of these methodologies and the unique advantage of the homogenization method of topology optimization for customized mesostructure design are outlined.

In chapter three, the application of homogenization method to mesostructure design is explained and the procedure to derive an equivalent material model is described. Further, a novel strategy to reduce the increase in number of design variables in the homogenization method by integrating it with a parametric smoothing scheme is discussed.

In chapter four, the optimization routine is discussed and the obtained design solutions are provided. The mesostructure design solutions are compared with non-mesostructure designs for subtractive processes.

In chapter five, the fabrication parameters for part designs and experimental set up are discussed. The validation of the design tool with experimental results is provided.

In chapter six, a list of accomplishments of the current work and the directions for future work are discussed.

## Chapter 2: Topology optimization for Designed Meso-structure

### 2.1 CHAPTER OBJECTIVES

The goal of this chapter is to select from among the several topology design techniques in the literature, a technique that is the best fit for material mesostructure design of a plane elasticity optimization problem. The necessary characteristic of a best fit topology design technique is that it should be capable of expressing material behavior as a function of the underlying mesostructure geometry. Towards this goal a review of topology optimization that includes a formal definition, the different topology design techniques, and their strengths and weakness for mesostructure design are provided. Further, a review of current literature in the design methodologies for mesoscale customization of a material design problem is provided outlining their limitations and motivating the use of the selected best topology design method for mesostructure design to address these limitations.

### 2.2. INTRODUCTION TO TOPOLOGY OPTIMIZATION

Topology design involves the determination of features such as the number and location of holes and the geometric connectivity of the material domain [32 & 33].



Figure 2.1: Shape variation without topology change [33]

Often in engineering usage the above definition is relaxed to include not only the connectivity of discontinuities but also the shape, size and distribution of these holes. The ideal topology for a particular design problem is not known a priori but emerges as a solution of the design optimization procedure [33]. Topology optimization takes as input the external loads on a given material and an allowable volume fraction of the design space that can be filled with this material.

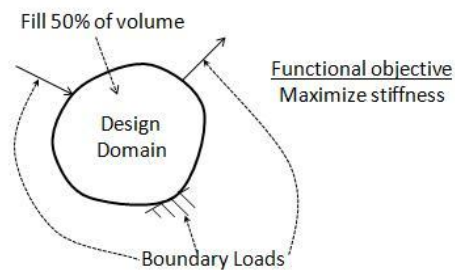


Figure 2.2: Inputs for a topology optimization procedure

The topology optimization procedure then determines the characteristic material distribution of the design space that results in the best objective function value while preserving all constraints in the problem definition. For a given set of external conditions different topologies can be generated depending on how much volume fraction is available for design. The material distribution of a cantilever beam optimized for maximum stiffness under different volume fraction constraints is shown in Figure 2.3. It can be seen that lower volume fractions result in a more truss-like structure.

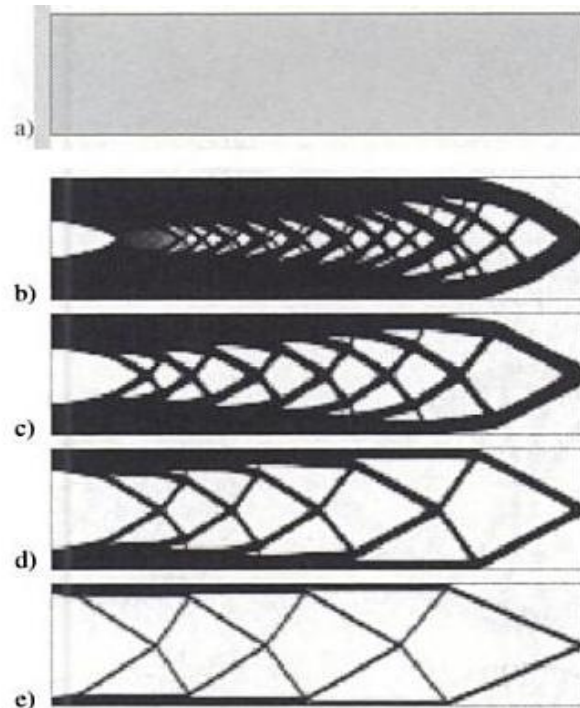


Figure 2.3: A cantilever beam optimized for b) 80% c) 60% d) 40% and e) 20% volume fractions [32]

### 2.3 TOPOLOGY OPTIMIZATION METHODS

Several methods have been proposed for implementing topology optimization to determine material distribution on a given design domain. Some of the popular methods in the literature include the following:-

- 1) Ground Structure Approach
- 2) Solid Isotropic Material with Penalization (SIMP)
- 3) Homogenization
- 4) Level Set Method

- 5) Evolutionary Structural Optimization (ESO)
- 6) Genetic Algorithms

All these methods with the exception of the level set approach were first developed for structural engineering problems, but have now been successfully extended to vibration analysis, fluid flow and heat transfer areas among others. The details of each of these methods are presented next.

### **2.3.1 Ground Structure Approach**

This method was one of the earliest approaches discussed first by Dorn *et al.* [34] followed by a number of authors in [35, 36 & 37] for truss topology design. In this method an initial structure with  $n$ -nodal points and  $m$ -links between the nodal points serves as the starting point for optimization. For a good structural performance, the larger the number of given nodal points the better. The cross-sectional areas of the links are the design variables. The task of optimization is to find the sub-structure of this ground structure that is the most optimal solution to the problem. In order to ensure that the most optimal solution is contained in the ground structure, a “complete ground-structure”- one which requires ‘ $m$ ’ to be the set of all possible connections between given ‘ $n$ ’ nodal points; is usually chosen as the starting point. The number of links, then, equals  $n(\frac{n-1}{2})$ .

Removal of a particular link from the ground structure introduces new discontinuities in the design region resulting in a topology change. Optimization determines which links can be removed while still achieving good structural performance under the specified constraints. For instance, if the goal is to design a structure with minimum compliance for a specified constraint on the maximum weight of the structure, then removing a particular link will cause changes in the nodal displacement values of the structure. These changes

are directly related to the compliance function of the structure causing an increase or decrease in its value, in effect guiding the optimization toward optimal topology changes within the design domain. The Figure 2.4 shows two possible ground structures for a plane truss.

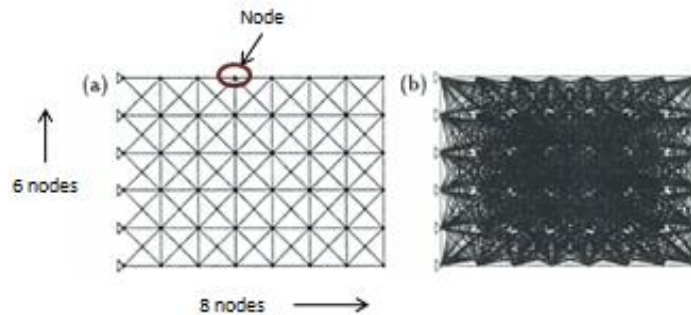


Figure 2.4: Ground structures for an 8 x 6 nodal layout of a plane truss a) neighbors connected – 137 links b) all possible connections – 730 links [38]

The ground structure approach has some disadvantages. As the number of nodal points increase, the number of design variables which is equal to the number of bars quickly becomes unmanageable. The addition and removal of links should be handled with caution as it could result in singular finite element matrices due to lack of connectivity to some nodes. Most algorithms handle this by removing elements and nodes only in periodic intervals after the optimization algorithm converges. A ground structure is still a valuable approach for low volume fraction problems for two reasons. Firstly, the optimization simplifies to the task of ascertaining which links need to be removed. Secondly, truss type topologies can be easily translated to manufacturable designs given the length and cross-sectional areas of the link elements. But, for our purpose of introducing characteristic mesostructures into the design domain the ground structure approach is clearly not a good candidate fit.



### 2.3.2 Solid Isotropic Material with Penalization (SIMP) Approach

The idea of parameterizing the design domain rather than solving a discrete on-off problem in the field of topology optimization was first documented by Bendsoe [39 & 40] in the late 1980's. Consequently two methods, namely, SIMP and homogenization, received much attention in the early 1990's. The SIMP method, also called the power law method, the direct approach, or the artificial density method, works by keeping a fixed finite element discretization and associating with each finite element a density function  $\rho(x)$  whose values lie between 0 and 1. A zero denotes a void and a 1 denotes a solid. Intermediate values create an artificial material that can be interpreted as a material mesostructure with holes as discussed by Rozvany *et al.* [41]. The final design solution possesses black regions (denoting solid regions), white regions (denoting voids) and grey regions (denoting intermediate densities). Several techniques were proposed to suppress or filter these grey (porous) regions to eliminate intermediate densities from the final design solution as they were impractical to fabricate with traditional manufacturing techniques. A review of these filtering schemes is available in [32].

The introduction of intermediate densities created a continuum topology optimization problem. Since the finite element discretization is kept fixed, the degree of grayness of these elements should be responsible for an objective value change. The material properties of a particular element are a function of its density so that element densities can be used as design variables to adjust the performance of the design. Thus, if the solid ( $\rho(x) = 1$ ) material property, say, Young's modulus in structural optimization is denoted by  $E_s$  then the young's modulus of elements with intermediate densities is given by  $E_i = E_s * \rho_i(x)$  where the subscript 'i' denotes a particular element. The goal of optimization is to determine the density distribution that solves a minimization or maximization problem with respect to the performance of the design.

As already noted, grey areas were introduced only to simplify the mathematics of the problem, but, for a manufacturer of the early 1990's, grey areas in the design solution were physically undefined. In order to drive the final solution away from the grey areas while solving a continuum topology optimization problem a large penalization parameter, - ' $p$ ,' is applied to the density of the element so that intermediate density elements have discounted stiffness. Thus, the fundamental equation that characterizes a SIMP approach is given by Equation 2.1.

$$E_i = \rho_i(x)^p E_s \quad ; \quad Vol = \int_{R^3} \rho(x) dx \quad (2.1)$$

where  $E_i$  is the young's modulus of the ' $i^{th}$ ' element in the design domain,  $\rho_i$  is the artificial density parameter for the ' $i^{th}$ ' element,  $p$  is the penalization parameter for intermediate densities (usually,  $p \geq 3$ ),  $E_s$  is the solid material young's modulus,  $Vol$ , is the total volume from distributed material in the design domain,  $R^3$  denotes a three dimensional design region and ' $x$ ' denotes the coordinate points in space for the centroid of a material element.

The SIMP approach has the following important advantages:

- 1) It uses a simple parameterization technique that is very easy to implement.
- 2) It has been extensively studied and applied to problems with complicated design conditions.
- 3) It uses only one design parameter, the density, for each element and thus requires less storage space and computational effort.

In spite, of these advantages, the SIMP technique is very effective only so long as the final goal is to obtain a black and white design. This is because a simple pre-multiplication of the properties with the density parameter  $\rho_i(x)$  ( $E_i = \rho_i(x)E_s$ ) is a

very inaccurate estimation of material properties for the mesostructure unit and therefore gray areas must not be retained in the SIMP method by setting a ' $p$ -value' closer to one. The SIMP method eliminates intermediate densities by raising them to a high power ' $p$ ' and thus overcomes both the inaccuracy of the parameterization model at intermediate densities and the difficulty of fabricating those intermediate densities with conventional non-additive manufacturing processes.

The 'black and white' quality of the final solution is largely dependent on proper choice of the penalization parameter, which has been a subject of research. In one case, Allaire [42] points out that the homogenization method can yield better solutions in terms of patterns and details than the SIMP approach although the objective criterion of compliance minimization is comparable in both cases. One explanation given by Allaire is that the concept of mesostructure is more weakly enforced in the SIMP approach than in homogenization. In general there is consensus in the fact that there is no implicit/explicit representation for the mesostructure in the SIMP approach. Thus, although the idea of material parameterization in SIMP is attractive for a mesostructure supportive design tool, the properties calculated using a power law equation do not apply if the underlying geometry of the mesostructure must be modeled accurately.

### **2.3.3 Homogenization Approach**

The homogenization method extends the idea of material design parameterization from SIMP by more rigorously defining a mesostructure that is smaller than the size of the finite element mesh. A mesostructure with a definite geometry in the homogenization method more clearly defines the physical meaning of intermediate density regions in the solution of a topology optimization procedure. Macroscopic material property

expressions (constitutive equations) are derived as a function of the geometry of the underlying mesostructure. To further make the mapping from the macroscopic scale to the mesostructure scale mathematically tractable, periodicity constraints are imposed in the neighborhood of every mesostructure unit also called a unit cell. The ratio of the dimensions of the macro and meso scales is left to the discretion of the designer and is called the magnitude or scaling factor. The periodicity constraints ensure that uniform boundary conditions apply to all meso scale units. This leaves scope for smooth variation in the densities of neighboring unit cells as long as the designer can make sure that the characteristic length of heterogeneities is small enough that no appreciable change in the boundary conditions of the unit cells is observed.

There have been two popular theories to define what constitutes a mesostructure. The first theory proposes the use of composite material matrix of hard and soft materials. Depending on the relative distribution of hard and soft materials different intermediate densities can be obtained. Some authors have also suggested the use of different ranks of composite materials, thus, introducing more than one level of hard/soft material distribution. One obvious disadvantage is that the complexity of the mathematical derivation of the homogenized properties increases considerably. A detailed description of the mathematical description of rank layered materials for homogenization is available in [43].

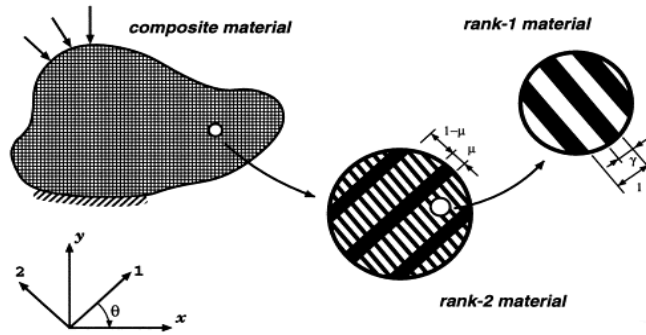


Figure 2.5: Construction of a rank-2 layered material [43]

The second theory proposes the use of holes inside a mesostructure unit so that hole sizes can correspond to different intermediate densities. In fact, as pointed out by Rozvany [43], the second theory is only a specific case of the first theory where the soft material is replaced by a void.

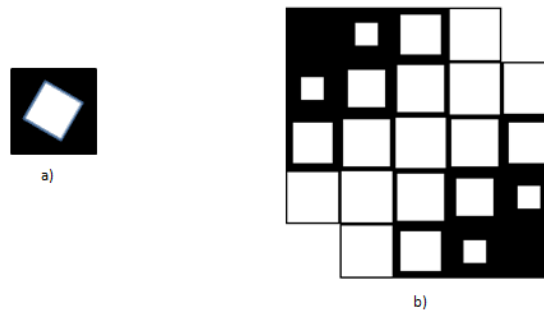


Figure 2.6: a) A square unit cell with  $60^\circ$  hole orientation b) A grid with a square unit cell at  $0^\circ$  hole orientation

In both theories, orientation of the layers or holes also has a significant effect on the material properties. For the hole theory, an additional parameter is the shape of the hole (square, triangle, hexagonal, kagome etc.). The fundamental equation governing the homogenization method for a one dimensional elasticity problem is given in Equation 2.2.

$$\begin{aligned}
\sigma(x) &= E^H \frac{du(x)}{dx} & \frac{d\sigma(x)}{dx} + \hat{F} &= 0 \\
E^H &= \left(1/\frac{1}{Y} \int_0^Y \frac{dy}{E(y)}\right) & \hat{F} &= \left(1/\frac{1}{Y} \int_0^Y F(y)dy\right)
\end{aligned} \tag{2.2}$$

where, ‘ $x$ ’ and ‘ $y$ ’ represent the macroscopic and mesoscopic scales respectively, ‘ $\sigma$ ’ represents the stress,  $E^H$  represents the homogenized young’s modulus for the mesostructure element, ‘ $E$ ’ represents the young’s modulus of the solid material, ‘ $F$ ’ represents the loads acting on the solid boundaries,  $\hat{F}$  represents the homogenized loads on the mesostructure unit. The integral equations in Equation 2.2 simply mean that the properties of each unit are adjusted for the size and the geometry of the hole within it.

One of the biggest strengths of the homogenization approach is conceptual clarity in the form of porous mesostructure for intermediate densities, but, to account for the cost of manufacturing these porous mesostructures, penalization schemes were again introduced on the final solution. In effect, the porous mesostructures were used only to create a continuous (rather than binary on-off) topology optimization problem, despite the effort spent on deriving the homogenized or equivalent material properties. This has led the optimization community to vote in favor of the SIMP approach as the most convenient material interpolation scheme especially after the public access to the 99-line SIMP implementation code by Sigmund [44] and the powerful constrained optimization solver based on the Method of Moving Asymptotes by Svanberg [45]. When the goal is not so much to obtain a black and white design, however, and there is a need to capture the mesostructure geometry information, the homogenization approach proves to be the ideal candidate upon which a design methodology can be formulated.

### 2.3.4 Level Set Method

The level set method is an alternative approach to material interpolation schemes first introduced by Oshner and Sethian [46] for tracking moving velocity fronts and subsequently extended to topology optimization problems in [47, 48]. In this method, a level set function is defined on an admissible shape in a fixed topology of a bounded domain as given in Equation 2.3. The level set function definition is shown in Figure 2.7.

$$\left\{ \begin{array}{l} \varphi(x) = 0, \quad x \in \partial\Omega \\ \varphi(x) < 0, \quad x \in \Omega \\ \varphi(x) > 0, \quad x \in \bar{\Omega} \end{array} \right\} \quad (2.3)$$

where, ‘ $\varphi$ ’, is the level set function, ‘ $x$ ’ is the coordinate of the centroid of a material element, ‘ $\partial\Omega$ ’ is the boundary separating the void region from a solid region, ‘ $\Omega$ ’, is the solid region and  $\bar{\Omega}$  is the void region. If we denote the design domain by ‘ $Q$ ’, then  $\Omega$  also represents an admissible shape in this design domain i.e.  $\Omega \subset Q \in R^d$ .

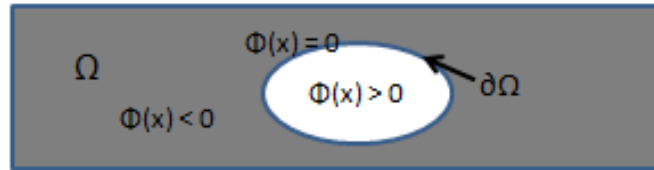


Figure 2.7: Schematic showing the definition of level set function in the design domain

The topological derivative of an objective criterion, say, compliance, governs the step size in topology changes (nucleation of new holes) during each iteration. The topological derivative of an objective criterion ‘ $J$ ’ is given by the topological asymptotic expansion in Equation 2.4.

$$J(\Omega_\rho) = J(\Omega) + \rho^d D_T J(x_0) + o(\rho^d) \quad (2.4)$$

where,  $\Omega_p$  is the domain of the new topology,  $\Omega$  is the domain of the old topology,  $\rho$ , is the new set of holes in  $\Omega_p$  that differentiates it from the domain  $\Omega$ ,  $D_T$  is the topological gradient of the objective criterion  $J$  with respect to the hole sets, ' $d$ ' is the dimension of the problem and  $o(\rho^d)$  represents the higher order terms.

The change or movement in boundary of ' $\Omega$ ' along the gradient descent direction  $-\frac{\partial J}{\partial \Omega}$  is equivalent to transporting the level set function ' $\phi$ ' by Equation 2.5.

$$\frac{\partial \phi}{\partial t} - v|\nabla \phi| = 0 \quad (2.5)$$

where, ' $\phi$ ', is the level set function, ' $t$ ' represents the descent step in the gradient algorithm and ' $v$ ' represents the gradient of the objective function in a direction parallel to the normal of the domain ' $\Omega$ '. The level set function is a more a direct description for the location of holes in the current domain of a topology.

The topological perturbations between iterations are kept small by placing a small limit on the amount of material that can be removed in any particular iteration. In order to avoid converging to a local minimum, Allaire [49] suggested coupling shape derivatives with topological derivatives and performing an optimal number of boundary variations between each topology change. Also, usually a weak material is substituted for a hole in order to keep the algorithm numerically stable.

The difficulty with the level set approach is that the solution is different for different starting points. Thus, a good initial guess is required to get comparable solutions with the homogenization technique for at least some of the 2-d problems as shown in [49]. The level set approach is also highly sensitive to a number of algorithmic parameters like the ratio of the modulus of the stiff to weak material and number of boundary variations between each topology change. This high sensitivity leads to



convergence to local optimum solutions. Thus, the robustness of the method is a primary issue. The level set method is still in the nascent stage of development and a thorough understanding of its merits and limitations are required before it can find a widespread application to even topology optimization problems. Thus, it is not a very good fit for our purpose.

### **2.3.5 Evolutionary Structural Optimization**

The evolutionary structural optimization (ESO) method, a misnomer, is a variation of the Fully Stressed Design (FSD) concept belonging to the class of so called hard-kill methods for topology optimization problems. In a fully stressed design approach all structural elements are at their maximum permissible stress limits. ESO was first discussed by Xie & Steven [50] and has since received much attention mainly because it is a zero order method – one that does not require the computation of objective function derivatives. It is based on the idea of “iteration wise optimal element change” (IOEC), a term introduced by Rozvany [51], by evaluating a criterion function on each element and minimizing (maximizing) it. A more correct terminology for the ESO called Sequential Element Rejection and Admission (SERA) was also coined in the same paper [51]. Most ESO algorithms use stress constraints as the criteria and perform element rejections based on these criteria during every iteration. An element rejection approach cannot benefit the purpose of characteristic mesostructure design because the optimization reduces to the task of finding a subset of the parent topology that contains the solution to the problem – a strategy that was also the concept behind the ground structure methodology. Further, the use of stress constraints to reject elements assumes that there is a definite relationship between satisfying stress constraints and an improvement in the objective function value

which is not necessarily true in all problems. Thus, there are inherent issues with the ESO technique that render it unsuitable as a method for mesostructure design.

### **2.3.6 Genetic Algorithms**

The methods discussed so far were all deterministic and, with the exception of ESO, gradient based, i.e. the change in the value of design variables was guided by the objective sensitivity. The downside to using a deterministic approach is the requirement for calculating gradients for objective and constraint functions. The application of genetic algorithms (GA) for topology optimization is a stochastic approach that can be applied to search for a global optimum, solve complicated objective functions and constraints, or be easily extended to solve non-linear elasticity problems. GA is based on the Darwinian theory of the survival of the fittest. Its application to topology design was first studied by Chapman [52] and subsequently by other authors [53, 54, 55 & 56]. GA works on the principle of crossover of chromosomes (representing values of design variables) of a particular generation (iteration). A crossover is a technique of using two sets of design variable values (two chromosomes) and applying a recombination scheme to yield one or more chromosomes. The probability of crossover for chromosomes with the highest fitness values is usually very high so that solution quality improves in successive generations. Mutation rates are used to steer clear of local minima.

The following parameters are required to conduct a GA based optimization

- 1) Fitness function
- 2) Population size
- 3) Starting Population
- 4) Crossover operator

- 5) Probability of crossover
- 6) Selection scheme
- 7) Probability of mutation
- 8) Fitness scaling parameter

The proper choice of the above parameter values is extremely important for the success of the GA and is also problem specific. Thus, considerable experience based on trial and error is required to set up a GA implementation. A chromosome in the context of topology optimization can be thought of as a sequence of zeros and ones representing the presence or absence of material at a point. The chromosome information is called the genotype.

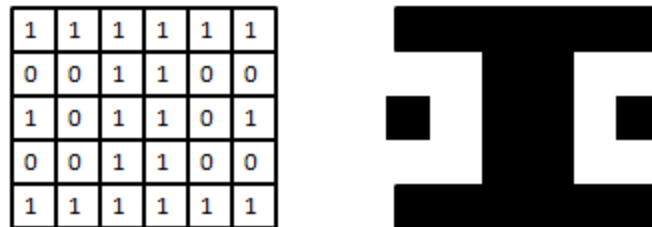


Figure 2.8: Chromosome array mapping to a topology

As can be seen from Figure 2.8 a one-to-one mapping of the chromosome to a topology can result in isolated pockets of material or sometimes starting from a random array of zeros and ones may not connect the load with the constraint boundaries. In order to avoid such anomalies, a design connectivity step is performed to map the chromosome to a topology. The design connectivity matrix also called the phenotype will add material whenever the element is a seed element (element on which constraints, loads are specified) and a void whenever a particular element does not share a line with any other element. The finite element analysis computes the fitness function, say, compliance with

the phenotype information of a chromosome. This fitness value can be used by the optimization procedure to determine how many times this particular parent can cross.

One of the biggest disadvantages of genetic algorithms is that they consume large computational resources even for a fairly simple problem. Thus, unless deterministic approaches cannot solve a particular problem, the use of GA for the same is not the preferred method.

#### **2.4 HOMOGENIZATION – THE SELECTED APPROACH FOR MESOSTRUCTURE DESIGN**

From the discussion on the different topology design techniques, the material parameterization schemes SIMP and homogenization clearly stand out from the rest as prospective candidates for developing a mesostructure supportive design tool. The rest of the methods - ground structure, ESO, level sets and GA, lack the sophistication to support adjustment of mesostructure units that is characteristic a of mesostructure topology design process. Between SIMP and homogenization, SIMP is the easier to implement but is not accurate enough as its governing design equations rely on an abstract density distribution, which is not explicitly linked to the mesostructure geometry. Therefore, homogenization is the clear winner and is the method adopted for the developed design tool in this work. The flip side to choosing the homogenization approach is the increased number of design variables that keep track of the geometry information as opposed to a single density variable in the SIMP method. This issue will be addressed during the development of the design tool.

## **2.5 LITERATURE REVIEW ON DESIGN METHODOLOGIES FOR CUSTOMIZED MESOSTRUCTURES**

The earliest discussion on the fabrication of topology design solutions using AM techniques can be traced to the work by Dutta *et al.* [57]. A recursive mask and deposit (MD) method for designs by the homogenization method was outlined. A five phase task list encompassing the derivation of homogenization based designs, substitution of grey areas with multi-material composition, geometry determination, fabrication through the MD method and mechanical testing was envisioned. Our work falls on similar lines of [57] while differentiating itself through perforations introduced by a square hole, fabrication with a more practical and commercially successful SLS method, testing and evaluation for performance parameters with black-white distribution solutions. It is to be noted that Johanson *et al.* [58] worked subsequently on an extension of [57] discussing black and white material distribution in the end solution ignoring the possibility for a mesostructure design.

Hollister *et al.* [59] used 3D printing to study an inverse homogenization design problem. Their work discussed the determination of a mesostructure hole shape for stated elastic properties that matched the tissue stiffness of human bones so that fabricated parts are compatible for enabling bone repair and growth. This work [59] while discussing the application of homogenization design method for parts from additive manufacturing is peripheral to the central theme of mesostructure driven material distribution optimization. There is a need to study the application of the direct homogenization procedure for problems outside of tissue engineering and that is the focus of this thesis.

Seepersad *et al.* [60] discussed the application of ground structure approach for the design of cellular structures, but, a ground structure approach merely allows for the removal of links to create cellular units and as such doesn't provide the ability to

parametrically vary the material distribution in the design domain. It offers a rough estimate for the geometry of designed mesostructures [61]. Wang *et al.* [61] suggested a unit truss approach where struts from a central node with their cross-sectional areas as design variables were used as mesostructure units. The unit truss approach is more computationally efficient than the ground structure approach of [60] but still is not as accurate as the homogenization method when it comes to representation of a parameterized mesostructure. Following the unit truss, Rosen [62] studied an octet unit truss approach using the cross-sectional areas of the truss elements of an octet link structure as design variables. Parametric modeling using truss elements between Bezier surface patches were also presented by Wang in [63]. Optimization was again governed by diameter of the truss elements. It is to be noted that [60, 61, 62 & 63] were all motivated by truss structures for mesostructure customization and were inferior to homogenization in terms of the extent of material parameterization that can be achieved. Further, most of the existing research using cellular structures or truss elements for mesostructure design has had to compromise between spending a lot of effort on designing a single truss unit or limiting their applicability to perfectly periodic, thin walled structures. For instance, Gibson and Ashby [64] discussed a set of simple relations between solid material properties and cellular material properties based on wall thickness and orientation inside the cellular structures. Unfortunately, these are valid only so long as the wall thickness would result in density values less than 0.2 and the cell structure is perfectly periodic. The homogenization procedure can go beyond these limitations by characterizing the entire range of densities and at the same time taking relatively less effort to design a single mesostructure unit.

Chen & Wang [65] discussed a design tool for performance tailored mesostructure design that is complimentary to some of the ideas discussed in this work.

Chen *et al.* discuss the approach of numerically evaluating the influence of varying the dimensions of certain structural parameters of a spring unit design on its maximum central displacement for an applied load. This information is used to fix the most influential parameters as design variables for the spring mesostructure unit and model its central displacement as a function of the geometry of these variables. Further, equivalent modulus values were derived using this model for the spring unit. This in essence is one of the alternative ways to perform homogenization without recourse to advanced mathematics. A single mesostructure unit was then fabricated using SLS to verify the displacement model predictions. In this work, a similar approach is adopted for the square mesostructure unit but we go one step further by integrating a design variable reduction scheme with our numerical model and also experimentally validating our design tool solutions to some standard problems obtained with optimization algorithms.

## **2.6 SUMMARY**

At this stage, we have taken forward the design tool requirements specified in Section 1.7 and used them to develop a case for the selection of homogenization as the best methodology for mesostructure designs for plane elasticity. A critical review of the existing topology optimization procedures and custom mesostructure design techniques was provided. The suitability of homogenization through its unique clarity of mesostructure definition and ability to parameterize the entire material density range was discussed in this chapter.

In the next chapter, the development of the design tool based on homogenization will be covered with insights into a novel design variable reduction procedure for homogenization.

## **Chapter 3: Homogenization with Design Variable Reduction – Theory and Implementation Details**

### **3.1 CHAPTER OBJECTIVES**

The primary goal of this chapter is to elucidate the implementation details for a mesostructure design tool based on the homogenization method. The material parameterization concept of homogenization allows the designer to keep the finite element discretization of the design domain fixed as different topologies evolve during optimization. This saves substantial computational effort spent in re-meshing the design domain every time the hole size in the mesostructure units change. To capture the geometry information of the mesostructure accurately, the homogenization method uses three design variables – shape, size and orientation of the hole per mesostructure unit. Thus, the number of design variables multiplies three times as fast as the number of mesostructure units increasing the computational overhead during optimization. A second goal of this chapter is to tackle this problem of large number of design variables by integrating a B-spline based parameterization scheme with the homogenization procedure. The parameterization scheme also serves the purpose of smoothing the mesostructural topology to avoid sharp changes in mesostructural topology which render the periodicity assumptions of homogenization invalid.

The contents of this chapter include a description of the homogenization procedure for the square mesostructure, derivation of plane stress and plane strain constitutive coefficients using homogenized properties, a set of validation procedures for the derived equivalent (homogenized) material properties, a literature review on design variable reduction techniques, and advantages and implementation details of the B-spline smoothing scheme for integration with homogenization based optimization.



## **3.2 THEORY OF HOMOGENIZATION**

Homogenization was first described for use in mechanics and electromagnetism to find homogeneous properties of a macrostructure with heterogeneous microstructures [66]. There are two ways to perform homogenization – one is to use a mathematical formulation and the second is to conduct experimental tests on select cases of mesostructure boundaries and interpolate these cases for the entire range of mesostructure densities. Each method has its own advantage. The mathematical formulation enables any arbitrarily shaped hole in the mesostructure unit to be treated through a set of integral equations. The disadvantage of this approach is that although in this work shape and orientation have been already been fixed, time consuming integral evaluations still have to be conducted on each mesostructure unit. A polynomial fit on a set of computational data, on the other hand, is easier to construct and evaluate than a set of integral equations if the shape and orientation of the hole are known a priori. The mathematical theory of homogenization for topology optimization is well established in the literature [40, 42, & 43] and will not be discussed here. Instead for completeness, the fundamental assumptions under which the homogenization approach is valid and, the results of the mathematical derivations for a 1-D problem are presented and the homogenized material properties for a 2D problem are presented as derived from curve fits to data from a set of computational experiments.

### **3.2.1 Fundamental assumption of homogenization**

Homogenization models for macrostructure are accurate only when the macrostructure can be characterized by a smoothly varying periodic function. A smoothly varying periodic function is also called a locally periodic function. The periodic pattern can be identified by looking at a scale that is significantly smaller than the macro scale.

This smaller scale is called the “meso” scale in this work. The ratio of the length of the unit vector in the meso scale to the length of the unit vector in macro scale is given by the parameter  $\epsilon$  i.e. when the macro scale is viewed under a microscope with a magnification factor  $\epsilon$  the mesoscale characteristics are obtained.

$$\hat{x} = \frac{x}{\epsilon} \quad (3.1)$$

$$F(x + \epsilon\hat{x}) = F(x) \quad (3.2)$$

where, ‘ $x$ ’ and  $\hat{x}$  represent the dimensions in the macro scale and meso scale respectively, ‘ $\epsilon$ ’ is the magnification factor and ‘ $F$ ’ is a locally periodic function shown in Figure 3.1.

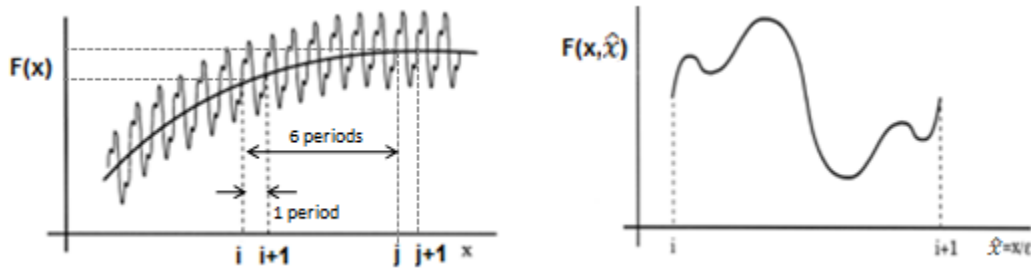


Figure 3.1: A locally periodic function on the macro( $x$ ) and meso( $\hat{x}$ ) scales [43]

It can be observed that in a close neighborhood – for two points separated by one fundamental period distance,  $i$  and  $i+1$ , the function values do not show significant difference but between  $i$  and  $j$  which are homologous points (points separated by multiples of the fundamental period) the function value shows significant difference. Again between points  $j$  and  $j+1$ , separated by a single period distance, the function value is almost the same. This is the meaning of a smoothly varying locally periodic function.

### 3.2.2 Elasticity problem definition – 1D and 2D

The mathematical representation based on homogenized material properties for a 1D problem is given in Equation 3.3.

$$\begin{aligned} \sigma(x) &= E^H \frac{du(x)}{dx} & \frac{d\sigma(x)}{dx} + \hat{F} &= 0 \\ E^H &= \left(1/\frac{1}{\hat{x}} \int_0^{\hat{x}} \frac{d\hat{x}}{E(\hat{x})}\right) & \hat{F} &= \left(1/\frac{1}{\hat{x}} \int_0^{\hat{x}} F(\hat{x})d\hat{x}\right) \end{aligned} \quad (3.3)$$

where, ‘ $x$ ’ and  $\hat{x}$  represent the macroscopic and mesoscopic scales respectively,  $\hat{X}$  is the characteristic mesoscale dimension, ‘ $\sigma$ ’ represents the stress,  $E^H$  represents the homogenized young’s modulus for the mesostructure element, ‘ $E$ ’ represents the young’s modulus of the solid material, ‘ $F$ ’ represents the loads acting on the solid boundaries,  $\hat{F}$  represents the homogenized loads on the mesostructure unit.

For a two dimensional problem, there are three stress values to be considered  $\sigma_{xx}$  the stress on the area perpendicular to the x-axis for a load in the x-direction,  $\sigma_{yy}$  the stress on the area perpendicular to the y-axis for a load in the y-direction,  $\sigma_{xy}$  the shear stress on the area perpendicular to the x-axis for a load in y-direction which is equal to the shear stress ( $\sigma_{yx}$ ) on a area perpendicular to the y-axis for a load in the x-direction. Correspondingly there are two values of young’s moduli and one shear modulus,  $E_1$  and  $E_2$  (1 denotes the x –direction and 2 denotes the y-direction), which represent the young’s moduli and  $G_{12}$  represents the shear modulus. In addition to these material moduli the Poisson’s ratio ( $\nu$ ) accounts for the lateral contraction during longitudinal extension. The stress vectors and the principal directions are shown in Figure 3.2.

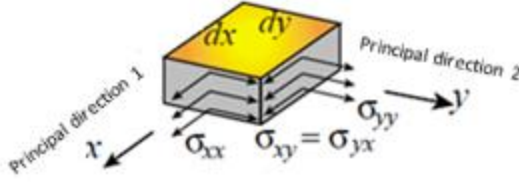


Figure 3.2: Plane elasticity element showing the stress component directions

The equilibrium equations for a 2D elasticity problem are given in Equation 3.4.

$$\frac{\partial \sigma_{xx}}{\partial x} + \frac{\partial \sigma_{xy}}{\partial y} + f_x = 0 \quad \frac{\partial \sigma_{xy}}{\partial x} + \frac{\partial \sigma_{yy}}{\partial y} + f_y = 0 \quad (3.4)$$

where,  $\sigma_{xx}$ ,  $\sigma_{xy}$ ,  $\sigma_{yy}$ , are the stress quantities as defined before, ' $f_x$ ' is the load in the x-direction and ' $f_y$ ' is the load in the y-direction.

The relation connecting stress quantities with material properties are given in Equation 3.5.

$$\begin{matrix} \sigma_{xx} \\ \sigma_{yy} \\ \sigma_{xy} \end{matrix} = \begin{bmatrix} D_{11} & D_{12} & 0 \\ D_{12} & D_{22} & 0 \\ 0 & 0 & D_{66} \end{bmatrix} \begin{Bmatrix} \varepsilon_x \\ \varepsilon_y \\ 2\varepsilon_{xy} \end{Bmatrix} \quad (3.5)$$

where,  $D_{11}$ ,  $D_{22}$ ,  $D_{12}$ ,  $D_{66}$  are called the terms of the constitutive matrix and their relation to the material properties depends on whether a plane stress or plane strain model is used for a two dimensional analysis of the elasticity problem.  $\varepsilon_x$  and  $\varepsilon_y$ , are the normal strain components and  $\varepsilon_{xy}$  is the shear strain component due to the applied loads in the x and y directions.

A plane stress approximation assumes that the thickness along the z-direction is very small in comparison to the x-y lengths of the geometry. This implies that the stress in the z-direction is negligible and can be ignored. A plane strain approximation model assumes that the length along the z-direction is infinitely long when compared to the

other two directions. This implies that the strain along the z-direction is negligible and can be ignored. These two models help convert a three dimensional problem to a two dimensional plane provided their assumptions are true. They determine the relationship between constitutive coefficients and material properties as shown in Equations 3.6 and 3.7.

Plane Stress:

$$D_{11} = D_{22} = \frac{E_1}{1-\nu^2}; D_{12} = \nu D_{11}; D_{66} = G_{12} \quad (3.6)$$

Plane Strain:

$$D_{11} = D_{22} = \frac{E_1(1-\nu)}{1-\nu-2\nu^2}; D_{12} = \frac{\nu E_1}{1-\nu-2\nu^2}; D_{66} = G_{12} \quad (3.7)$$

It is to be noted that since a square mesostructure is used in this work,  $E_1$  is automatically equal to  $E_2$  and this equality has been used in Equations 3.6 and 3.7 to eliminate  $E_2$ . Therefore, the homogenized properties of all these material parameters ( $E_1$ ,  $\nu$  and  $G_{12}$ ) need to be derived as a function of the mesostructure variables to represent a plane elasticity optimization problem. In this work the derivation of homogenized properties for both plane stress and plane strain approximation models are carried out.

### 3.2.3 Computational method for derivation of homogenized properties

A finite element model of a single mesostructure at different hole sizes is constructed and analyzed in ANSYS Mechanical 12.1 [78]. The important parameters for the model include the mesh size and the appropriate homogeneous boundary conditions on the mesostructure unit. Sun *et al.* [67] discussed the boundary conditions for a representative volume element for homogenizing a composite material structure. These

boundary conditions are valid for our purpose of homogenizing a mesostructure as it is the special case of a two material composite system where one of the materials is replaced by a void. The boundary conditions for normal loading are shown in Figure 3.3

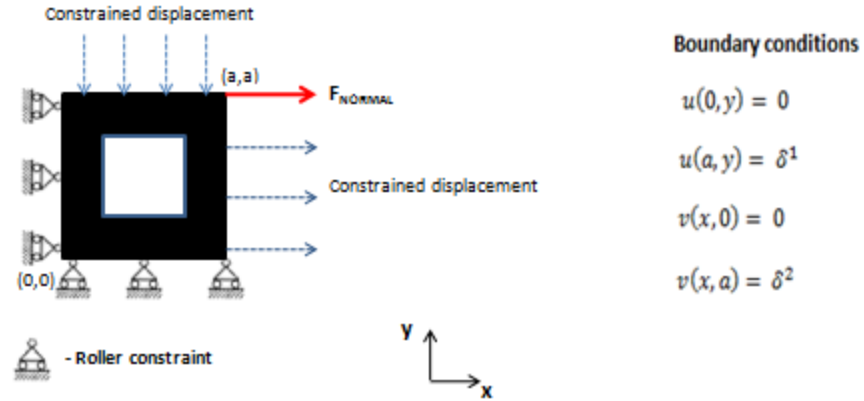


Figure 3.3: Normal loading and boundary conditions to determine  $E_1^H$  and  $\nu_{12}^H$

The rightmost plane of the mesostructure is constrained to have a uniform x-displacement represented by  $u(a,y)$  and the topmost plane is constrained to have a uniform y-displacement represented by  $v(x,a)$ . The leftmost plane is constrained to have zero x-displacement while the bottommost plane is constrained to have zero y-displacement. These conditions enable us to calculate the Young's modulus and Poisson's ratio of the material.

The homogenized Young's modulus in the x-direction is given by the Equation 3.8.

$$E_1^H = \frac{\sigma_{xx}}{\epsilon_{xx}} = \frac{F_{Normal}}{(a * 1) \frac{\delta^1}{a}} = \frac{F_{Normal}}{\delta^1} \quad (3.8)$$

The homogenized Poisson's ratio is given by the Equation 3.9.

$$\nu_{12}^H = -\frac{\varepsilon^{22}}{\varepsilon^{11}} = -\frac{\frac{\delta^2}{a}}{\frac{\delta^1}{a}} = -\frac{\delta^2}{\delta^1} \quad (3.9)$$

The loading and boundary conditions for the determination of homogenized shear modulus are given in Figure 3.4.

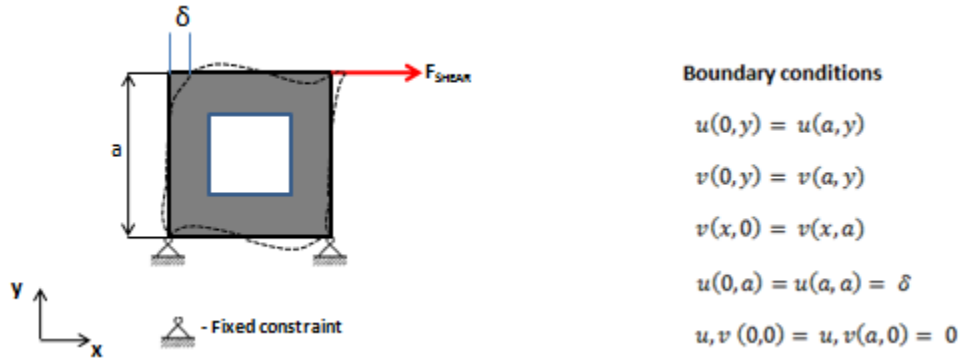


Figure 3.4: Shear loading and boundary conditions to determine  $G_{12}^H$

The bottommost and topmost planes of the mesostructure have uniform  $y$  displacements. The rightmost and leftmost planes have uniform  $x$  and  $y$  displacements. Zero  $x$ - $y$  constraints are applied to the corner points in the bottommost plane to eliminate rigid body motion. These conditions allow us to determine the shear modulus of the material.

The homogenized shear modulus is given by Equation 3.10.

$$G_{12}^H = \frac{\sigma_{12}}{\gamma_{12}} = \frac{F_{Shear}}{(a * 1) \frac{\delta}{a}} = \frac{F_{Shear}}{\delta} \quad (3.10)$$

A very fine mesh was used to run the computational model so that acceptable accuracy in the estimation of the displacement values was obtained. This is particularly important as the experiment is repeated for very large hole size values when the walls of

the mesostructure become very thin. A meshed mesostructure unit in ANSYS Mechanical 12.1 is shown in Figure 3.5.

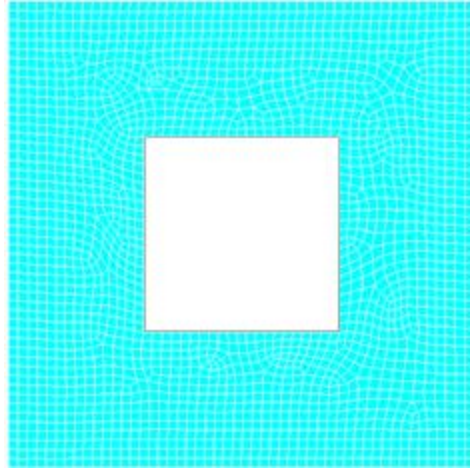


Figure 3.5: Finite element mesh of the mesostructure in ANSYS Mechanical 12.1

Each hole size can be mapped to a density value between 0 and 1.0 using Equation 3.11.

$$\rho = 1 - \frac{\tilde{a}_h^2}{a^2} \quad (3.11)$$

where,  $\tilde{a}_h$  is the hole size and  $a$  is the mesostructure size as shown in Figure 3.6.



Figure 3.6: Mesostructure unit for density calculation



Fifty computational experiments were performed in ANSYS that correspond to fifty different density values separately for the two models – plane stress and plane strain. The resulting modulus and Poisson’s ratio values using Equations 3.8, 3.9 and 3.10 for the two different models were independently interpolated to construct a set of polynomial functions given in Equation 3.12 for each model that can be used to obtain the property values for any hole size. These are the equations for the homogenized properties of our plane elasticity problem.

$$\begin{aligned}
E_1^H(\rho_h) &= \sum_{i=0}^N E_1^H{}_i \prod_{\substack{j=0 \\ j \neq i}}^N \frac{(\rho_h - \rho_0)(\rho_h - \rho_1) \dots (\rho_h - \rho_{j-1})(\rho_h - \rho_{j+1})(\rho_h - \rho_N)}{(\rho_j - \rho_0)(\rho_j - \rho_1) \dots (\rho_j - \rho_{j-1})(\rho_j - \rho_{j+1})(\rho_j - \rho_N)} \\
\nu_{12}^H(\rho_h) &= \sum_{i=0}^N \nu_{12}^H{}_i \prod_{\substack{j=0 \\ j \neq i}}^N \frac{(\rho_h - \rho_0)(\rho_h - \rho_1) \dots (\rho_h - \rho_{j-1})(\rho_h - \rho_{j+1})(\rho_h - \rho_N)}{(\rho_j - \rho_0)(\rho_j - \rho_1) \dots (\rho_j - \rho_{j-1})(\rho_j - \rho_{j+1})(\rho_j - \rho_N)} \\
G_{12}^H(\rho_h) &= \sum_{i=0}^N G_{12}^H{}_i \prod_{\substack{j=0 \\ j \neq i}}^N \frac{(\rho_h - \rho_0)(\rho_h - \rho_1) \dots (\rho_h - \rho_{j-1})(\rho_h - \rho_{j+1})(\rho_h - \rho_N)}{(\rho_j - \rho_0)(\rho_j - \rho_1) \dots (\rho_j - \rho_{j-1})(\rho_j - \rho_{j+1})(\rho_j - \rho_N)}
\end{aligned} \tag{3.12}$$

where,  $E_1^H(\rho_h)$ ,  $\nu_{12}^H(\rho_h)$ ,  $G_{12}^H(\rho_h)$  are polynomial functions to determine the corresponding material properties for any arbitrary density value between 0 and 1.0,  $N$  represents the number of data points (50 in this case),  $E_1^H{}_i$ ,  $\nu_{12}^H{}_i$ ,  $G_{12}^H{}_i$  are the property values at data points given by  $\rho_h$ .

The different density values and their displacements under loads have been provided in a tabular form in Appendix A.

### 3.3 RELATING HOMOGENIZED MODEL WITH MACROSCOPIC EQUILIBRIUM EQUATIONS

In order to make use of the homogenized material properties in the macrostructure of the plane elasticity problem, a finite element procedure must be derived to model the macrostructure as an assembly of mesostructure units with elastic properties defined by Equation 3.12. The derivation of this finite element discretization scheme is described here.

Equations 3.4 and 3.5 can be combined to rewrite the governing equilibrium equations as in Equation 3.13.

$$\begin{aligned}\frac{\partial}{\partial x} \left( D_{11} \frac{\partial u}{\partial x} + D_{12} \frac{\partial v}{\partial x} \right) + \frac{\partial}{\partial y} \left( D_{66} \frac{\partial u}{\partial y} + D_{66} \frac{\partial v}{\partial x} \right) + f_x &= 0 \\ \frac{\partial}{\partial x} \left( D_{66} \frac{\partial u}{\partial y} + D_{66} \frac{\partial v}{\partial x} \right) + \frac{\partial}{\partial y} \left( D_{12} \frac{\partial u}{\partial x} + D_{22} \frac{\partial v}{\partial y} \right) + f_y &= 0\end{aligned}\tag{3.13}$$

where,  $u$  and  $v$  represent the displacement in the x-direction and y-direction respectively,  $f_x$  and  $f_y$  are the body loads.

Equation 3.13 is a second order partial differential equation (pde) that can be solved by the virtual displacement method. In the virtual displacement method the solution to a pde is obtained by multiplying it with a fictitious virtual displacement function and integrating the resulting equation in its weak form. The weak form of a differential equation is a method of converting a higher order pde into a product of lower order pdes using the product rule in calculus.

$$\int U dV = \int UV - \int v dU\tag{3.14}$$

Multiplying the pair of equations in 3.13 with separate virtual displacements  $w_1$  and  $w_2$ , we get Equation 3.15.

$$\begin{aligned}
w_1 \frac{\partial}{\partial x} \left( D_{11} \frac{\partial u}{\partial x} + D_{12} \frac{\partial v}{\partial x} \right) + w_1 \frac{\partial}{\partial y} \left( D_{66} \frac{\partial u}{\partial y} + D_{66} \frac{\partial v}{\partial x} \right) + w_1 f_x &= 0 \\
w_2 \frac{\partial}{\partial x} \left( D_{66} \frac{\partial u}{\partial y} + D_{66} \frac{\partial v}{\partial x} \right) + w_2 \frac{\partial}{\partial y} \left( D_{12} \frac{\partial u}{\partial x} + D_{22} \frac{\partial v}{\partial y} \right) + w_2 f_y &= 0
\end{aligned} \tag{3.15}$$

Taking the integral on both sides of Equation 3.15 and applying the product rule in equation 3.14, we get Equation 3.16.

$$\begin{aligned}
&\int w_1 \left( D_{11} \frac{\partial u}{\partial x} + D_{12} \frac{\partial v}{\partial x} \right) n_x ds - \int \frac{\partial w_1}{\partial x} \left( D_{11} \frac{\partial u}{\partial x} + D_{12} \frac{\partial v}{\partial x} \right) dx dy + \\
&\int w_1 \left( D_{66} \frac{\partial u}{\partial y} + D_{66} \frac{\partial v}{\partial x} \right) n_y ds - \int \frac{\partial w_1}{\partial y} \left( D_{66} \frac{\partial u}{\partial y} + D_{66} \frac{\partial v}{\partial x} \right) dx dy + \int w_1 f_x dx dy = 0 \\
&\int w_2 \left( D_{66} \frac{\partial u}{\partial y} + D_{66} \frac{\partial v}{\partial x} \right) n_x ds - \int \frac{\partial w_2}{\partial x} \left( D_{66} \frac{\partial u}{\partial y} + D_{66} \frac{\partial v}{\partial x} \right) dx dy + \\
&\int w_2 \left( D_{12} \frac{\partial u}{\partial x} + D_{22} \frac{\partial v}{\partial y} \right) n_y ds - \int \frac{\partial w_2}{\partial y} \left( D_{12} \frac{\partial u}{\partial x} + D_{22} \frac{\partial v}{\partial y} \right) dx dy + \int w_2 f_y dx dy = 0
\end{aligned} \tag{3.16}$$

where, 's' represents the surface boundary,  $n_x$  and  $n_y$  represent the normal vectors to the surface in the 'x' and 'y' directions respectively.

The terms that have the normal vectors defined to the surface  $ds$  represent the boundary integrals and the terms that have integrals defined in infinitesimal areas  $dx dy$  constitute the quantities in the interior region of the domain. The Equation 3.16 assumes a unit thickness for the elements in the z-direction and can be pre-multiplied with the thickness  $h_e$  for other thickness values.

The equation can be solved numerically using a computer if the problem is decomposed into a finite space by the discretizing the design domain into a set of N-discrete points. These points are called nodes in the finite element terminology. In order to obtain displacement values between these nodal points a bilinear interpolation scheme

is used as given in Equations 3.17 and 3.18. A bilinear interpolation scheme requires values at four nodal points constituting a subdivision scheme based on an assembly of rectangular units. The four corner points of the rectangle represent the four nodal values. This representation is also convenient for our mesostructure design driven by square shapes. In the derivation, we use rectangular units but they can be easily converted to square sub units by assuming equal sides.

$$u = \sum_{j=1}^N u_j^e \psi_j^e(x, y); v = \sum_{j=1}^N v_j^e \psi_j^e(x, y) \quad (3.17)$$

$$\begin{bmatrix} \psi_1 & \psi_3 \\ \psi_2 & \psi_4 \end{bmatrix} = \begin{bmatrix} (1 - \frac{x}{a})(1 - \frac{y}{b}) & (1 - \frac{x}{a})\frac{y}{b} \\ \frac{x}{a}(1 - \frac{y}{b}) & \frac{x}{a}\frac{y}{b} \end{bmatrix} \quad \begin{array}{c} \psi_2 \quad a \quad \psi_4 \\ \square \\ \psi_1 \quad b \quad \psi_3 \end{array} \quad (3.18)$$

where, ‘ $u$ ’ and ‘ $v$ ’ denote the displacement values in the ‘ $x$ ’ and ‘ $y$ ’ direction,  $u_j^e$  and  $v_j^e$  represent the nodal displacement values of a particular rectangular subunit called an element in finite element terminology. For our case, an element will correspond to a single square mesostructure unit within the design domain.  $\psi_j^e$  for  $j$  equals 1 to 4 represent the basis functions for the bilinear interpolation as given in 3.18. ‘ $x$ ’ and ‘ $y$ ’ in Equation 3.18 denote the coordinates of a point within the rectangular element.

Substituting 3.17 and 3.18 back into 3.16 and adopting a matrix notation we get Equations 3.19 and 3.20.

$$\begin{bmatrix} [K^{11}] & [K^{12}] \\ [K^{21}]^T & [K^{22}] \end{bmatrix} \begin{Bmatrix} \{u\} \\ \{v\} \end{Bmatrix} = \begin{Bmatrix} \{F^1\} \\ \{F^2\} \end{Bmatrix} \quad (3.19)$$

$$\begin{aligned}
K^{11} &= \sum_{i=1}^{\text{No. Elements}} \sum_{j=1}^{\text{No. Elements}} \int h_e \left( D_{11} \frac{\partial \psi_i}{\partial x} \frac{\partial \psi_j}{\partial x} + D_{66} \frac{\partial \psi_i}{\partial y} \frac{\partial \psi_j}{\partial y} \right) dx dy \\
K^{12} &= \sum_{i=1}^{\text{No. Elements}} \sum_{j=1}^{\text{No. Elements}} \int h_e \left( D_{12} \frac{\partial \psi_i}{\partial x} \frac{\partial \psi_j}{\partial y} + D_{66} \frac{\partial \psi_i}{\partial y} \frac{\partial \psi_j}{\partial x} \right) dx dy \\
K^{22} &= \sum_{i=1}^{\text{No. Elements}} \sum_{j=1}^{\text{No. Elements}} \int h_e \left( D_{66} \frac{\partial \psi_i}{\partial x} \frac{\partial \psi_j}{\partial x} + D_{22} \frac{\partial \psi_i}{\partial y} \frac{\partial \psi_j}{\partial y} \right) dx dy
\end{aligned}$$

$$\begin{aligned}
\begin{Bmatrix} u \\ v \end{Bmatrix} &= \begin{Bmatrix} u_1 \\ v_1 \\ u_2 \\ v_2 \\ \vdots \\ u_n \\ v_n \end{Bmatrix}; \quad F^1 = \sum_{i=1}^{\text{No. Elements}} \left( \int_{\Omega_e} h_e \psi_i f_x dx dy + \int_{\Gamma_e} h_e \psi_i t_x ds \right) \\
&\quad F^2 = \sum_{i=1}^{\text{No. Elements}} \left( \int_{\Omega_e} h_e \psi_i f_y dx dy + \int_{\Gamma_e} h_e \psi_i t_y ds \right)
\end{aligned}$$

(3.20)

where,  $h_e$  denotes the thickness of the rectangular element in the z-direction and we assume an uniform thickness for all elements,  $t_x$  and  $t_y$  denote the forces acting on the design domain boundary also called traction forces.

It has to be borne in mind that as the  $(u, v)$  matrix is assembled as a set of x-y displacements of the nodal points in a specific order, the load vector and the stiffness matrix ( $K$ ) elements should be consistent with this order. The terms of the  $[K]$  matrix in Equation 3.19 are called the stiffness matrix terms. Equation 3.19 represents the global stiffness matrix for the macrostructure as it is formed by assembling individual stiffness matrix terms of each rectangular element in the discretized space.

For a single element, each of  $K^{11}$ ,  $K^{12}$  and  $K^{22}$  will be a 4x4 matrix thus resulting in an 8x8 element stiffness matrix with 8 degrees of freedom (4 in x and 4 in the y-direction). Often for a single element the matrix notation takes the form given in

Equations 3.21 and 3.22. The superscript 'e' is attached to the matrix quantities to identify them as rectangular element matrices and differentiate them from terms of Equations 3.19 and 3.20.

$$[K^e] \{\Delta^e\} = \{f^e\} + \{Q^e\} \quad (3.21)$$

$$[K^e] = \int [B^e]^T [D^e] [B^e] dx dy \quad (3.22)$$

$$[B^e] = \begin{bmatrix} \frac{\partial}{\partial x} & 0 \\ 0 & \frac{\partial}{\partial y} \\ \frac{\partial}{\partial x} & \frac{\partial}{\partial y} \end{bmatrix} \begin{bmatrix} \psi_1 & 0 & \psi_2 & 0 & \psi_3 & 0 & \psi_4 & 0 \\ 0 & \psi_1 & 0 & \psi_2 & 0 & \psi_3 & 0 & \psi_4 \end{bmatrix} \quad (3.23)$$

Substituting 3.18 in 3.23, we get Equation 3.24.

$$[B^e] = \begin{bmatrix} -\frac{1}{a} (1 - \frac{y}{b}) & 0 & \frac{1}{a} (1 - \frac{y}{b}) & 0 & -\frac{1}{b} \frac{y}{a} & 0 & \frac{1}{b} \frac{y}{a} & 0 \\ 0 & -\frac{1}{b} (1 - \frac{x}{a}) & 0 & -\frac{1}{b} \frac{x}{a} & 0 & \frac{1}{b} (1 - \frac{x}{a}) & 0 & \frac{1}{b} \frac{x}{a} \\ -\frac{1}{b} (1 - \frac{x}{a}) & -\frac{1}{a} (1 - \frac{y}{b}) & -\frac{1}{b} \frac{x}{a} & \frac{1}{a} (1 - \frac{y}{b}) & \frac{1}{b} (1 - \frac{x}{a}) & -\frac{1}{b} \frac{y}{a} & \frac{1}{b} \frac{x}{a} & \frac{1}{b} \frac{y}{a} \end{bmatrix} \quad (3.24)$$

$$[D^e] = \begin{bmatrix} D_{11} & D_{12} & 0 \\ D_{21} & D_{22} & 0 \\ 0 & 0 & D_{66} \end{bmatrix} \quad (3.25)$$

$$\Delta^e = \{u_1 v_1 u_2 v_2 u_3 v_3 u_4 v_4\}^T; \{f^e\} = \int_{\Omega_e} h_e [\psi^e]^T \begin{Bmatrix} f_x \\ f_y \end{Bmatrix} dx dy; \{Q^e\} = \int_{\Gamma_e} h_e [\psi^e]^T \begin{Bmatrix} t_x \\ t_y \end{Bmatrix} ds \quad (3.26)$$

Using Equations 3.22, 3.24 and 3.25, it is possible to derive all the 8 x 8 entries of the stiffness matrix for a particular rectangular element. The stiffness matrix is symmetric. Therefore, not all terms have to be derived ( $K_{ij} = K_{ji}$ , for  $i \neq j$  and  $K_{ii} = K_{11}$ ). The derived element stiffness matrix terms are shown Table 3.1.

$K_{11}$	$\frac{D_{11}^e b}{3a} + \frac{D_{66}^e a}{3b}$	$K_{34}$	$\frac{D_{11}^e b}{3a} + \frac{D_{66}^e a}{3b}$
$K_{12}$	$\frac{D_{12}^e}{4} + \frac{D_{66}^e}{4}$	$K_{35}$	$-\frac{D_{11}^e b}{6a} - \frac{D_{66}^e a}{6b}$
$K_{13}$	$\frac{D_{11}^e b}{6a} - \frac{D_{66}^e a}{3b}$	$K_{36}$	$\frac{D_{12}^e}{4} + \frac{D_{66}^e}{4}$
$K_{14}$	$-\frac{D_{11}^e b}{4} + \frac{D_{66}^e}{4}$	$K_{37}$	$-\frac{D_{11}^e b}{3a} + \frac{D_{66}^e a}{6b}$
$K_{15}$	$-\frac{D_{11}^e b}{3a} + \frac{D_{66}^e a}{3b}$	$K_{38}$	$-\frac{D_{12}^e}{4} + \frac{D_{66}^e a}{4}$
$K_{16}$	$\frac{D_{12}^e}{4} - \frac{D_{66}^e a}{4}$	$K_{45}$	$\frac{D_{21}^e}{4} + \frac{D_{66}^e}{4}$
$K_{17}$	$-\frac{D_{11}^e b}{6a} - \frac{D_{66}^e a}{6b}$	$K_{46}$	$-\frac{D_{22}^e a}{6b} - \frac{D_{66}^e b}{6a}$
$K_{18}$	$-\frac{D_{12}^e}{4} - \frac{D_{66}^e}{4}$	$K_{47}$	$\frac{D_{21}^e}{4} - \frac{D_{66}^e}{4}$
$K_{22}$	$\frac{D_{22}^e a}{3b} + \frac{D_{66}^e b}{3a}$	$K_{48}$	$\frac{D_{22}^e a}{6b} - \frac{D_{66}^e b}{3a}$
$K_{23}$	$\frac{D_{12}^e}{4} - \frac{D_{66}^e}{4}$	$K_{56}$	$-\frac{D_{12}^e}{4} - \frac{D_{66}^e}{4}$
$K_{24}$	$-\frac{D_{22}^e a}{3b} + \frac{D_{66}^e b}{6a}$	$K_{57}$	$\frac{D_{11}^e b}{6a} - \frac{D_{66}^e a}{3b}$
$K_{25}$	$-\frac{D_{21}^e}{4} + \frac{D_{66}^e}{4}$	$K_{58}$	$\frac{D_{12}^e}{4} - \frac{D_{66}^e}{4}$
$K_{26}$	$\frac{D_{22}^e a}{6b} - \frac{D_{66}^e b}{3a}$	$K_{67}$	$-\frac{D_{21}^e}{4} + \frac{D_{66}^e}{4}$
$K_{27}$	$-\frac{D_{21}^e}{4} - \frac{D_{66}^e}{4}$	$K_{68}$	$-\frac{D_{22}^e a}{3b} + \frac{D_{66}^e b}{6a}$
$K_{28}$	$-\frac{D_{22}^e a}{6b} - \frac{D_{66}^e b}{6a}$	$K_{78}$	$\frac{D_{12}^e}{4} + \frac{D_{66}^e}{4}$

Table 3.1: Derived symmetric stiffness matrix terms for a rectangular element

The  $[D^e]$  matrix in Equation 3.25 is the constitutive matrix expression that provides us the underlying mechanism to connect the material properties of the homogenized mesostructures with the macro scale behavior of the macrostructure for

applied loads in macro scale. The rectangular elements of the finite element procedure can be very easily replaced by the square mesostructure units with the homogenized material properties from Equation 3.12. Equation 3.22 can be rewritten as a stiffness matrix equation for a mesostructure element using Equation 3.27.

$$[K^{eH}]_{mn} = \int [B^e]^T [D^{eH}] [B^e] dx dy \quad (3.27)$$

where,  $[D^{eH}]$  is now the homogenized constitutive matrix terms derived using relations specified in Equations 3.28, 3.29 and 3.30,  $[K^{eH}]$  is the homogenized element stiffness matrix and m, n denote the node numbers associated with a mesostructure element in the global numbering scheme used for the macrostructure.

$$[D^{eH}] = \begin{bmatrix} D_{11}^H & D_{12}^H & 0 \\ D_{12}^H & D_{22}^H & 0 \\ 0 & 0 & D_{66}^H \end{bmatrix} \quad (3.28)$$

Plane Stress:

$$D_{11}^H = D_{22}^H = \frac{E_1^H}{1 - \nu^{H2}}; \quad D_{12}^H = \nu^H D_{11}^H; \quad D_{66}^H = G_{12}^H \quad (3.29)$$

Plane Strain:

$$D_{11}^H = D_{22}^H = \frac{E_1^H (1 - \nu^H)}{1 - \nu^H - 2\nu^{H2}}; \quad D_{12}^H = \frac{\nu^H E_1^H}{1 - \nu^H - 2\nu^{H2}}; \quad D_{66}^H = G_{12}^H \quad (3.30)$$

Equation 3.27 can be applied to each mesostructure unit in the design domain and the stiffness matrices of the individual mesostructure units can be summed up to obtain the global stiffness matrix for the macrostructure as given in Equation 3.31.



$$[K_{mn}]_{Global} = [K_{mn}]_{Global} + \sum_{i=1}^{No. of Elements} [K^{eH}_{mn}]^i \quad (3.31)$$

where,  $[K_{mn}]_{Global}$  represents the global stiffness matrix of the macrostructure,  $[K^{eH}_{mn}]^i$  represents the stiffness matrix of ' $i^{th}$ ' mesostructure unit in the macrostructure and  $m, n$  denote the node numbers of the four nodes in the  $i^{th}$  mesostructure unit in the global numbering scheme used for the macrostructure.

The global stiffness matrix in Equation 3.31 can be used in the macroscopic equilibrium equation as given in Equation 3.32.

$$[K_{mn}]_{Global} \{u_{mn}\}_{xy} = \{f_{mn}\}_{xy} \quad (3.32)$$

where,  $\{u_{mn}\}_{xy}$  is a column vector consisting of the  $u, v$  displacements in the  $x$  and  $y$  directions respectively of the  $m * n$  nodes and  $\{f_{mn}\}_{xy}$  is a column vector consisting of the loads acting in the  $x$  and  $y$  directions respectively on the  $m * n$  nodes in the design domain. Again, it is important that the order of arrangement of the  $m * n$  nodes be consistent in all the terms of the Equation 3.32.

Equations 3.32, 3.31, 3.27 and Table 3.1 with homogenized coefficients given by 3.28, 3.29 and 3.30 can be used to solve any plane elasticity problem with mesostructure elements. These equations are complete set of governing equations for our mesostructure supportive design tool based on homogenization approach. To solve an optimization problem based on these equations, an objective criterion must be defined that can be computed from the displacement values obtained by solving these governing equations. We will present methods to validate our obtained homogenized constitutive coefficients  $[D^{eH}]$  in the next section.

### **3.4 VALIDATION OF DERIVED HOMOGENEOUS COEFFICIENTS**

#### **3.4.1 Comparison with HOMOG code**

The success of the optimization procedure relies heavily on the fitness of the homogenization material model in providing a good estimation of the material properties. Therefore, it is of utmost importance that design engineer validates the derived homogenized coefficients and makes sure that the approximation is good enough for the problems in which they will be employed. Three methods for validation are discussed. The first method involves the comparison of results with HOMOG code available in [68]. The HOMOG code developed by Hassani solves the homogenized properties for a square mesostructure with a rectangular hole. The polynomial functions for a plane stress approximation model are provided. The difference between our work and the HOMOG code is that for a set hole size values this work uses a computational approach and the HOMOG code evaluates mathematical integrals to determine the homogenized coefficients. Further, the HOMOG code does not handle a plane strain approximation model. In this work polynomial functions were formulated for both models and their corresponding constitutive matrix terms have been computed.

Since the results in [68] were tabulated in the form of hole size values for a mesostructure size of one unit and our functions in Equation 3.12 are represented in terms of density of mesostructure cells, we convert the results of [68] into density values using Equation 3.11. The Table 3.2 shows the values of the derived coefficients from the results in [68] and the computed coefficients in this work for ten different density values.

Density	Computed Coefficients			HOMOG code		
	$D_{11}^H$	$D_{12}^H$	$D_{66}^H$	$D_{11}^H$	$D_{12}^H$	$D_{66}^H$
1.00	1.0000	0.3000	0.3503	1.0000	0.3000	0.3500
0.96	0.8825	0.2533	0.3003	0.8833	0.2540	0.2947
0.91	0.7638	0.2032	0.2393	0.7644	0.2039	0.2313
0.84	0.6347	0.1485	0.1665	0.6348	0.1487	0.1582
0.75	0.5092	0.0986	0.0983	0.5101	0.0992	0.0917
0.64	0.3931	0.0598	0.0477	0.3955	0.0606	0.0441
0.51	0.2885	0.0326	0.0183	0.2891	0.0328	0.0168
0.36	0.1875	0.0139	0.0054	0.1886	0.0141	0.0045
0.19	0.0920	0.0033	0.0006	0.0925	0.0035	0.0005
0.00	0.0000	0.0000	0.0000	0.0000	0.0000	0.0000

Table 3.2: Comparison of computed coefficients with results of the HOMOG code [68] for plane stress 2D model

There is excellent agreement for the homogenized constitutive matrix terms and therefore validates our plane stress polynomial functions.

### 3.4.2 Validation by comparison with ANSYS Mechanical 12.1 on a test problem

The second validation method adopts a more rigorous approach, in the sense that, a simple problem consisting of grid of a mesostructures is solved using the homogenized coefficients and the results are compared with the same problem solved on ANSYS Mechanical 12.1 - a commercial finite element package for structural analysis [78]. The density of the mesostructure is kept constant in the grid thus enforcing a trivial case of periodicity required for the application of the homogenization theory.

A square grid of a fixed volume fraction is filled with 8 x 8 mesostructure units of the same volume fraction (uniform densities). The grid is subjected to pressure loading at the top most plane and constraints are applied at the bottom and left plane to prevent rigid body motion. A finite element code was written in MATLAB using the homogenized

mesostructure units as material elements and the analysis was performed using the results of the procedure described in Section 3.3 (Equations 3.32, 3.31, 3.27, Table 3.1, Equations 3.28, 3.29 and 3.30). The results of the maximum displacement observed in the top most plane are compared with the displacements of the same problem solved in ANSYS Mechanical 12.1 for a plane strain problem. A solid Quad 4node (Library element #: 42) element was used in ANSYS with at least 4 elements in each mesostructure wall giving a very fine mesh.

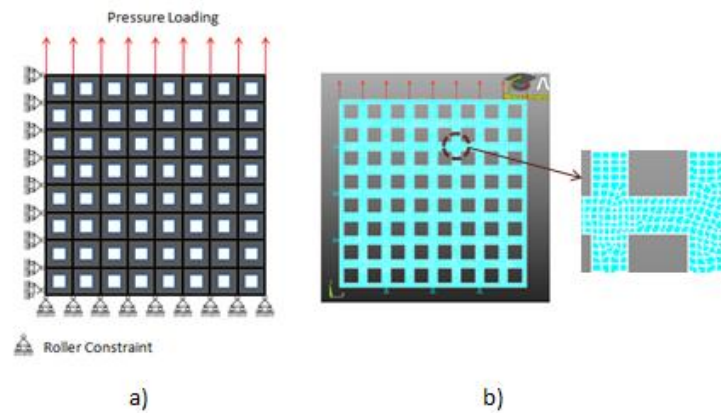


Figure 3.7: Square grid – a) Homogenized model b) ANSYS model with a zoomed view of the elements in the solid regions

A comparison of the displacement values are provided in Figure 3.8. An overall deviation of around 5% was observed. Since, we were using a polynomial fit on data points this 5% error can be explained from the inaccuracy of a piecewise cubic spline to perfectly match the results of the ANSYS model. For all practical purposes, a uniform error of 5% is good enough because, optimization will not be affected by such a low error percentage in the displacement value that is consistent with all densities.

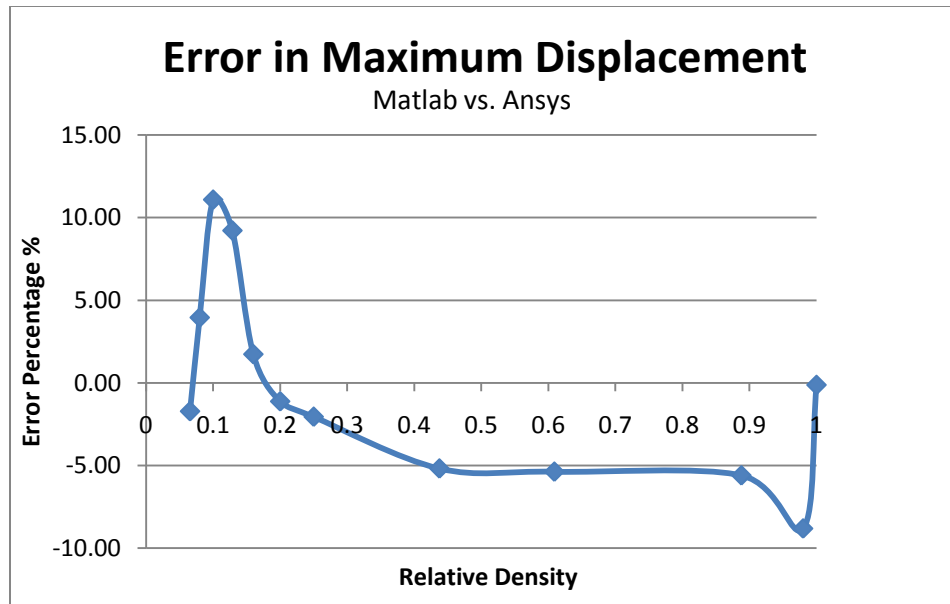


Figure 3.8: Error in maximum displacement of the homogenized model measured against the ANSYS model of the same problem for plane strain assumption

It is also to be noted that at low density values ( $<0.20$ ), the error in maximum displacement shoots up considerably. A possible explanation for this behavior is that at low densities it was difficult to enforce the presence of at least 4 mesh elements between the mesostructure walls as they were very thin. This could have rendered the predictions from the ANSYS model inaccurate. In order to verify this portion of the density region, low density models developed in [69] were used.

### 3.4.3 Validation of the low density region with cellular models

Low density cellular structures have been analyzed [64 & 69] and expressions for material properties based on cell wall thickness were derived as a function of the mesostructure geometry and orientation. Analytical estimates of the low density models are not valid beyond densities greater than 0.2 because they assume that the cell walls are thin and apply Timoshenko's beam theory, which is based on bending of beam-like cell

walls. As walls become thicker, the cells behave more like a solid plane element rather than as a beam. The expressions for material properties of a square mesostructure with a square hole from [69] are given in Equations 3.33, 3.34 and 3.35.

$$\frac{E_1^H}{E_s} = \frac{E_2^H}{E_s} = 0.5r \quad (3.33)$$

where,  $E_1^H$  and  $E_2^H$  are the homogenized Young's moduli of the low density cell in the  $x$  and  $y$  directions,  $E_s$  is the solid material Young's modulus and ' $r$ ' is the relative density of the cell.

The relative density of the cell is defined as the ratio of the material to non-material region inside cell. It is equivalent to the density of the mesostructure unit given by Equation 3.11. The expression for relative density is given in Equation 3.34.

$$r = 1 - \frac{\tilde{a}_h^2}{a^2} = \rho \quad (3.34)$$

where,  $\tilde{a}_h$  and ' $a$ ' are the size of the hole and size of the square cell respectively.

The homogenized shear modulus ( $G_{12}^H$ ) and Poisson's ratio ( $\nu_{12}^H$ ) are given by Equation 3.35.

$$\frac{G_{12}^H}{E_s} = 0.0625r^3 \quad \frac{\nu_{12}^H}{\nu_s} = 0.5r \quad (3.35)$$

The maximum displacement calculated by using these expressions for material properties allow the comparison of maximum displacements in this work obtained by substitution of the computed homogenized coefficients for low density mesostructure units. The results of the comparison are shown in Figure 3.9.

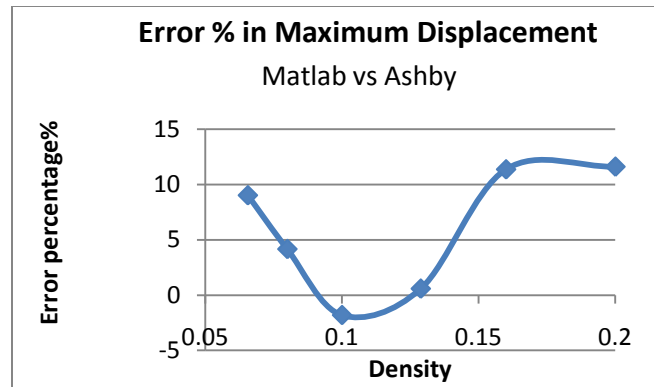


Figure 3.9: Error in maximum displacement of the homogenized model measured against the low density model of the same problem for plane strain assumption

Again, the overall error percentage was over 5% and less than 15% which confirmed the correctness of homogenized equations and finite element derivations. There are several potential explanations for the error. The analytical expressions may be less accurate for higher densities, since they are based on bending beam equations. Also, it is possible that the polynomial curve fits, described in Equation 3.12, for predicting homogenized material properties fit the underlying ANSYS predictions less accurately for certain densities. As observed earlier, an error around 5% in the displacement values gives us enough confidence on the expected behavior in the actual experimental environment of the obtained design solutions from optimization. Further, a sufficient safety factor (greater than 5%) is usually built into engineering design specifications and hence, a 5% deviation in deformation results would be relatively insignificant in the final environment.

### **3.5 DESIGN VARIABLE REDUCTION USING A PARAMETRIC SCHEME ON THE HOMOGENIZATION APPROACH**

The homogenization approach for mesostructure design introduces more design variables into the optimization problem than the other more popular and widely used material parameterization technique – SIMP. The total number of design variables can quickly spiral out of control in homogenization when enough resolution is sought to improve design solutions. But, the SIMP approach cannot be employed for mesostructure design due to reasons brought in Section 2.4. Therefore, there is a need to devise schemes that can reduce the large number of design variables in the homogenization approach. To this end, we discuss a novel parametric smoothing scheme based on B-splines that can be integrated into the optimization routine based on a homogenization material model. A second added advantage of our smoothing scheme is ensuring that the variations in densities are smooth in any local neighborhood of a particular mesostructure unit. This was discussed in Section 3.2.1 as one of the necessary constraints that determines the accuracy of the predictions of the homogenization approach. The behavior of the designs under experimental conditions will not match the predictions of the homogenized model if this condition is not met. Therefore, the ability of the smoothing scheme to satisfy this condition cannot be underestimated. A brief review on the available techniques for design variable reduction is presented next before more details on the smoothing scheme are discussed.

Design Variable reduction can be performed in one of the following ways [70].

1. Variable linking
2. Fixing variables
3. Mathematical functions



The first two techniques are not very appropriate for our purpose, since fixing or linking the variables would limit the diversity of the mesostructure. Instead, the variable values could be smoothed, using a parametric mathematical function with fewer variables. Consider the cubic mathematical function given in Equation 3.36.

$$\rho(x) = A_0 + A_1x + A_2x^2 + A_3x^3 \quad (3.36)$$

where,  $\rho(x)$  is the density function on the independent variable 'x' which determines the location of say a mesostructure unit,  $A_0, A_1, A_2, A_3$  are the coefficients of the polynomial function.

Let us assume there are fifty mesostructure units in our design domain and the optimization routine uses the mathematical function represented by Equation 3.36 to reduce the number of design variables. If the optimization routine is allowed to operate on the four coefficients of Equation 3.36 as design variables and the polynomial function is used to generate the fifty density values for all the mesostructure units, then the number of design variables has been reduced from 50 to 4. This is the approach of the mathematical functions technique.

Since, this work deals with a two dimensional problem, it is ideal to discuss a surface parameterization function rather than a one-dimensional polynomial functions for design variable reduction. Parnas [71] *et al.* used Bezier surfaces for reducing design variables in optimum design of composite structures for minimum weight under failure stress constraints. The thicknesses of fiber layers were controlled by the z-heights of a Bezier surface measured at the centroid of each element and the orientation of fiber courses were controlled by Bezier curves. A bicubic surface patch with 16 control points and a Bezier curve with 4 control points were used to determine design variable values during optimization. Implementing this strategy could result in significant computational

savings for meso-structure characterization in homogenization. In the following discussion, we will discuss why the B-splines are more appropriate for our work than the Bezier or other parameterization schemes.

Parametric surfaces using Bezier, B-splines and Rational B-splines (NURBS) have been widely used in computational geometry problems. Each of these surface shapes is controlled by the location of a set of control points. The difference between these surface representations lies in the extent of local control that these control points can exert on the surface shape. Local control can be understood as whether the change in location of a particular control point affects the shape of the entire surface or the portion of a surface in a small neighborhood of the control point. NURBS and B-splines provide the same level of local control followed by Bezier surfaces. A NURBS parameterization has the potential to represent quadric surfaces exactly which B-Splines and Bezier cannot and a B-Spline can provide local control which a Bezier surface cannot. In fact, a Bezier surface is one particular case of B-spline surface and a B-Spline surface is one particular case of the NURBS surface. The classification is shown in Figure 3.10.

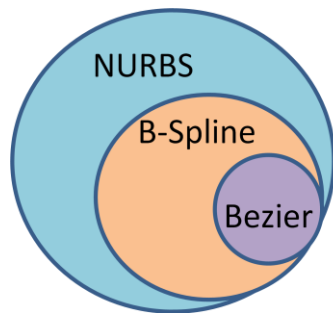


Figure 3.10: Classification of parametric surfaces

For our purpose of ensuring a smooth distribution of densities in the design domain, B-Splines are the perfect fit because we require sufficient local control over the mesostructure.

### 3.5.1 Introduction to B-spline Surface Parameterization Technique

A detailed discussion of B-spline surfaces is available in [72]. The necessary details of surface parameterization for the purpose of integration with a homogenization based optimization routine will be reviewed here. There are certain terminologies associated with a B-spline surface that need to be understood before delving into the subject of B-spline surfaces. A B-spline surface is a tensor product of b-spline curves in the two different parametric directions. A B-spline curve itself is generated by the specification of a set of points known as “control points”. A straight line joining the adjacent control points make up the sides of the “control polygon” or “control net” for the generated curve. A B-spline surface is shown in Figure 3.11.

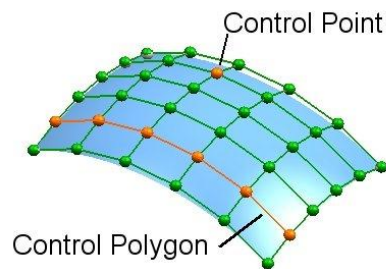


Figure 3.11 A B-spline surface with its control points and control polygon [73]

The total number of control points denotes the highest possible “order” that the resulting curve can have. The order of the curve denotes the level of continuity possessed by the curve (order = degree+1 = continuity+2). A smaller subset of the total number of control

points can be used to construct lower order curves that can be splined together at the boundaries and hence the name B-splines. The biggest advantage of the B-splines is probably its “knot vector”. A good “knot vector” allows the designer to locally control the curve geometry. Stated in another way, it defines the extent of the domain that is influenced by any particular control point. Each individual entity of the knot vector is called a “knot value”. The length of the knot vector is related to the order of the curve. So, if the order changes then the knot vector also changes. When the order is kept constant, the relative distance of the knot values determines the extent of influence (specified by a parameter range) that a particular control point has on the parameterized curve. A B-spline curve is thus completely specified by the set of control points, the order and the knot vector associated with it. The mathematical expression is given in Equation 3.37.

$$\begin{aligned}
 P_k(t) &= \sum_{i=1}^{n+1} Z_i N_{i,k}(t) \\
 t_{min} &\leq t < t_{max} \\
 2 &\leq k \leq n + 1 \\
 N_{i,1}(t) &= \begin{cases} 1 & \text{if } x_i \leq t < x_{i+1} \\ 0 & \text{otherwise} \end{cases} \\
 N_{i,k}(t) &= \frac{(t - x_i)N_{i,k-1}(u)}{x_{i+k-1} - x_i} + \frac{(x_{i+k} - t)N_{i+1,k-1}(t)}{x_{i+k} - x_{i+1}}
 \end{aligned} \tag{3.37}$$

where,  $P_k(t)$  is the B-spline curve of order  $k$  and parameter ‘ $t$ ’ with ‘ $t_{min}$ ’ and ‘ $t_{max}$ ’ specifying the lower and upper bounds of the parameter respectively,  $Z_i$  are the position vectors of the  $n+1$  control points,  $N_{i,k}$  are the normalized B-spline basis functions, and  $x_i$

denotes the values of the knot vector. There are a total of  $n+k+1$  knot values in the knot vector.

Since we are more interested in a surface than a curve, the tensor product surface formed from the curve definition in Equation 3.37 is presented in Equation 3.38.

$$Q_{k,l}(u,w) = \sum_{i=1}^{n+1} \sum_{j=1}^{m+1} Z_{i,j} N_{i,k}(u) M_{j,l}(w)$$

$$N_{i,1}(u) = \begin{cases} 1 & \text{if } x_i \leq u < x_{i+1} \\ 0 & \text{otherwise} \end{cases}$$

$$N_{i,k}(u) = \frac{(u - x_i) N_{i,k-1}(u)}{x_{i+k-1} - x_i} + \frac{(x_{i+k} - u) N_{i+1,k-1}(u)}{x_{i+k} - x_{i+1}}$$

$$M_{j,1}(u) = \begin{cases} 1 & \text{if } y_j \leq w < y_{j+1} \\ 0 & \text{otherwise} \end{cases}$$

$$M_{j,l}(w) = \frac{(w - y_j) M_{j,l-1}(w)}{y_{j+l-1} - y_j} + \frac{(y_{j+l} - w) M_{j+1,l-1}(w)}{y_{j+l} - y_{j+1}}$$

(3.38)

where,  $Q_{k,l}(u,w)$  denotes the B-spline surface of order  $k$  and  $l$  in the parametric directions  $u$  and  $w$  respectively,  $Z_{i,j}$  are the position vectors of the  $(n+1) \times (m+1)$  control points,  $N_{i,k}$  are the normalized B-spline basis functions of order  $k$  for the  $(n+1)$  control points in the  $u$  direction,  $M_{j,l}$  are the normalized B-spline basis functions of order  $l$  for the  $(m+1)$  control points in the  $w$  direction,  $x_i$  denotes the values of the knot vector in the  $u$ -direction and  $y_j$  denotes the values of the knot vector in the  $w$ -direction.

The values of the knot vector denote the values of the parameter in a particular direction. Adjacent knot values denote the extent of control for a particular control point on the parameterized surface. There are two different classifications for knot vectors – uniform or non-uniform and open or periodic. A uniform knot vector has knot values that are evenly spaced. A non-uniform knot vector has unequally spaced knot values. An open knot vector has multiplicity of knot values at the beginning and at the end and the multiplicity is equal to the order of the curve. A periodic knot vector does not have multiplicity of knot values. An open uniform knot vector is given by Equation 3.39.

$$\begin{aligned}
 x_i &= 0 & 1 \leq i \leq k \\
 x_i &= i - k & k + 1 \leq i \leq n + 1 \\
 x_i &= n - k + 2 & n + 2 \leq i \leq n + k + 1
 \end{aligned} \tag{3.39}$$

A particular knot vector will belong to a unique category under both classifications. Two examples have been given for each possible classification

Periodic uniform knot vector

[0 1 2 3 4] , [0 0.5 1.0 1.5 2.0 2.5]

Periodic non-uniform knot vector

[0 1 2.5 3 4.25] , [0 0.25 1.3 1.6 3.0]

Open uniform knot vector

[0 0 1 2 3 3] , [0 0 0 1 2 3 4 4 4]

Open non-uniform knot vector

[0 0 2.5 3 4 4] , [0 0 0 1.3 4.6 5 5 5]

The influence of a knot vector on surface shape is shown in Figure 3.12. The same knot vector was used for both the parameter directions.

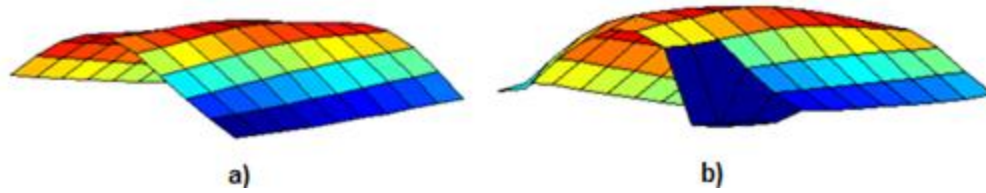


Figure 3.12 Two surfaces with the same control net and order but different parameter values in their knot vectors a) open uniform -  $[0\ 0\ 0\ 0\ 1\ 2\ 2\ 2\ 2]$  b) periodic non uniform –  $[0\ 1\ 2\ 3\ 4\ 5\ 5\ 5\ 5]$

A non-uniform knot vector created a greater curvature for the surface in Figure 3.12. In this work, an open uniform knot vector representation is used for curves that define the surface as it provides the flexibility to overlap the influence regions of control points and the ability to interpolate end points.

### 3.5.2 Homogenization with Parameterized Surfaces

The goal of a parametric smoothing scheme in a homogenization procedure is two-fold. First, it ensures that in the neighborhood of a particular cell the density function varies smoothly. Second, it reduces the number of design variables for optimization routines solving homogenization based topology problems. To meet those requirements, the optimization algorithm should no longer access the density function directly for optimization. Any change of the density function should be possible only through a change in the geometry of the surface, with the control points of the surface as design variables. As the surface geometry is constrained by the continuity requirements specified by the order, if the density function is mapped from such a surface there cannot be any sharp change in gradients of the density function in the resulting solution of the design problem. Of the surface parameters, order takes care of the continuity requirements, knot vector length is fixed by the order and number of control points and knot values

determine the extent of the neighborhood of a particular meso-structure unit. Therefore, the locations of control points represent the only suitable choice as optimization variables for the design problem. Two of the three coordinate locations can be kept fixed. Thus, the height of each of the control points can be varied between a fixed range of 0 and 1 to relate the surface height at fixed x-y locations measured from a datum plane directly to the density of cells in the mesostructure design problem. The datum plane will hold the fixed x-y locations and as the control point heights are modified by the optimization procedure, the surface geometry changes, thereby adjusting the heights at the locations of these fixed x-y spots. Since the surface heights are a direct measure of the density of the cells, the topology of the design domain changes causing an increase or decrease in the objective function value. A schematic sketch of the density measurement using surface height from a datum plane is shown in Figure 3.13.

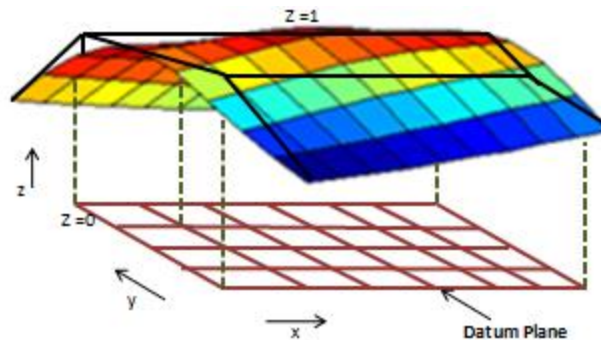


Figure 3.13 Measuring densities as surface heights from a datum plane at  $z=0$

For the purpose of clarity the control point locations have not been shown in Figure 3.13. The black lines are the edges of the control polygon of the surface. In surface parameterization, a large number of control points results in a higher fidelity surface, with a smaller number of control points resulting in a lower fidelity or smoothing surface. The number of control points is always significantly less than the number of



points it could be used to generate on the surface. This implies that we could always have the number of control points to be less than the number of fixed locations at which the surface will be measured for densities, thus, effectively reducing the number of optimization variables for the problem. The compromise in seeking such reduction is that changing a control point height will now affect a set of cells rather than just a single cell. Thus, we lose the one-to-one correspondence between a mesostructure unit and a control point. A good tradeoff needs to be sought on the extent of reduction and the ability to locally control regions of a surface.

### 3.5.3 Sensitivity Equations for Homogenization with Parameterized Surfaces

A gradient-based optimization routine for a design problem works faster if the derivative (sensitivity) information for the objective function with respect to the optimization parameters can be provided analytically, rather than numerically. Since a parametric mapping translates optimization variables to the design variables, it rests with the parametric implementation scheme to return the derivative quantities in the chain rule shown in the Equation 3.40.

$$\frac{\partial S}{\partial Z_{i^*,j^*}} = \sum_{r \in \chi} \frac{\partial S}{\partial \rho_r} \frac{\partial \rho_r}{\partial Z_{i^*,j^*}} \quad (3.40)$$

where, ‘ $S$ ’ represents the objective function,  $Z_{i^*,j^*}$  denotes the z-height of the  $(i^*,j^*)^{th}$  control point, ‘ $r$ ’ is the set of all mesostructure units whose densities are changed when the z-height of the  $(i^*,j^*)^{th}$  control point is changed,  $\rho_r$  is the density of the  $r^{th}$  mesostructure unit and ‘ $\chi$ ’ denotes the region of influence of the  $(i^*,j^*)^{th}$  control point.

In Equation 3.40, the first derivative quantity of the summation can be obtained from the finite element analysis routine and the second derivative quantity from

the smoothing scheme. We will first discuss the derivative quantity associated with the smoothing scheme. The derivative of the density of the  $r^{th}$  mesostructure unit with respect to the  $(i^*, j^*)^{th}$  control point is given in Equation 3.41.

$$\frac{\partial \rho_r}{\partial Z_{i^*, j^*}} = \frac{\partial Q_{k,l}(u, w)}{\partial Z_{i^*, j^*}} \quad (3.41)$$

Substituting, the  $Q_{k,l}(u, w)$  from its definition in Equation 3.38 we get Equation 3.42.

$$\frac{\partial Q_{k,l}(u, w)}{\partial Z_{i^*, j^*}} = \frac{\partial \sum_{i=1}^{n+1} \sum_{j=1}^{m+1} Z_{i,j} N_{i,k}(u) M_{j,l}(w)}{\partial Z_{i^*, j^*}} \quad (3.42)$$

Since each of the control point height is an independent variable in Equation 3.38, except for some  $i = i^*$  and  $j = j^*$  all other terms in the derivative of the summation quantity of Equation 3.42 reduce to zero resulting in Equation 3.43.

$$\frac{\partial Q_{k,l}(u, w)}{\partial Z_{i^*, j^*}} = \frac{\partial N_{i^*, k}(u) M_{j^*, l}(w) Z_{i^*, j^*}}{\partial Z_{i^*, j^*}} \quad (3.43)$$

Since the basis functions are simple weighting functions independent of control point heights, Equation 3.43 now becomes Equation 3.44

$$\frac{\partial Q_{k,l}(u, w)}{\partial Z_{i^*, j^*}} = N_{i^*, k}(u) M_{j^*, l}(w) \quad (3.44)$$

The Equation 3.44 implies that for a  $\delta Z_{i^*, j^*}$  change in the height of the  $(i^*, j^*)^{th}$  control point, the surface height in its influence domain  $\chi$  changes by a magnitude equal to its weighting function given by 3.43. The difficulty in evaluating these basis functions for derivative calculations of control points lies in the fact that they are dependent on the

parametric directions  $u$  and  $w$ . Therefore, they are different for different  $(u, w)$  pairs. For instance, let's say there are 200 mesostructure units and 100 control points. If each control point influences 3 mesostructure units then the basis function associated with any particular control point has to be evaluated for the x-y locations corresponding to the 3 mesostructure units influenced by that control point. There would be total of 300 (100x3) such evaluations for derivative computation, although there are a total of only 200 design variables. Further, each basis function itself is recursively dependent on basis functions of smaller order complicating the problem. Even if an iterative approach is used instead of a recursive formulation the computational overhead is significant.

One method of overcoming the significant computational burden associated with derivative computation is to use approximation techniques rather than an exact analytical approach. A finite difference scheme could be adopted as a method of approximating the derivatives. This scheme works by taking the difference of surface heights at  $(u, w)$  locations close to the control point under consideration as shown in Equation 3.45.

$$\frac{\partial Q(u, w)}{\partial z_{i^*, j^*}} = \frac{Q(u^{+z_{i^*, j^*}}, w^{+z_{i^*, j^*}}) - Q(u^{-z_{i^*, j^*}}, w^{-z_{i^*, j^*}})}{\delta z_{i^*, j^*}} \quad (3.45)$$

where,  $+z_{i^*, j^*}$  denotes a point very close to the right of  $z_{i^*, j^*}$  and  $-z_{i^*, j^*}$  denotes a point very close to the left of  $z_{i^*, j^*}$ .

But, since a surface is two dimensional the difference scheme would involve interpolation of four corner  $(u, w)$  surface points in a close neighborhood of the  $(i^*, j^*)^{\text{th}}$  control point. Further, the derivative value computed this way will be valid for the entire influence domain only when the influence domain  $\chi$  is very small. Therefore, this is a not a very attractive solution to our problem. Thus, there is a definite need to look for

alternative methods for sensitivity estimation or to opt for non-gradient based optimization methods. The reduction in the number of design variables enabled by the parametric representation should make it more tractable to apply non-gradient based methods.

Now, we will address the first term in the chain rule of Equation 3.40. In order to look into this term, the objective function needs to be determined. In this thesis focus is on 2-d plane elasticity problems and a suitable objective quantity for such problems is the strain energy. The goal is to minimize the strain energy for the resulting structure. Strain energy is defined by the Equation 3.46.

$$S = \sum_{i=1}^{No.Elements} \frac{1}{2} d^{eT} K^e d^e \quad (3.46)$$

where,  $d^e$  represent the displacement of nodal points of the structure as a column vector and  $K^e$  is the element stiffness matrix of the mesostructure unit.

Taking the derivative the strain energy with respect to density of the  $r^{\text{th}}$  mesostructure element, we get Equation 3.47.

$$\frac{\partial S}{\partial \rho_r} = \sum_{i=1}^{No.Elements} \frac{1}{2} \left[ \frac{\partial d^{eT}}{\partial \rho_r} K^e d + d^{eT} \frac{\partial K^e}{\partial \rho_r} d + d^{eT} K^e \frac{\partial d^e}{\partial \rho_r} \right] \quad (3.47)$$

The force equilibrium equation for a mesostructure element is given by Equation 3.48.

$$F^e = K^e d^e \quad (3.48)$$

The force vector is a given quantity for the problem and is not dependent on the design variables of the problem. Taking the derivative of Equation 3.48 with respect to  $\rho_r$  we get Equation 3.49.

$$\frac{\partial F^e}{\partial \rho_r} = \frac{\partial K^e}{\partial \rho_r} d^e + K^e \frac{\partial d^e}{\partial \rho_r} = 0 \Rightarrow \frac{\partial K^e}{\partial \rho_r} d^e = -K^e \frac{\partial d^e}{\partial \rho_r} \quad (3.49)$$

Taking the transpose on both sides of Equation 3.48 and using the fact that  $K^e$  is a symmetric matrix, we get Equation 3.50.

$$d^{eT} \frac{\partial K^e}{\partial \rho_r} = -\frac{\partial d^{eT}}{\partial \rho_r} K^e \quad (3.50)$$

Substituting Equations 3.49 and 3.50 back into 3.47 we get Equation 3.51.

$$\frac{\partial S}{\partial \rho_r} = \sum_{i=1}^{No.Elements} \frac{1}{2} \left[ -d^{eT} \frac{\partial K^e}{\partial \rho_r} d^e + d^{eT} \frac{\partial K^e}{\partial \rho_r} d^e - d^{eT} \frac{\partial K^e}{\partial \rho_r} d^e \right] = -\frac{1}{2} d^{eT} \frac{\partial K^e}{\partial \rho_r} d^e \quad (3.51)$$

From Equation 3.51, it turns out that the derivative of strain energy with respect to density of a  $r^{th}$  mesostructure element simply amounts to finding the derivative of the stiffness matrix of the mesostructure element with respect to the density of the same element.

As already noted from 3.27, 3.28 3.29 and 3.30 the stiffness matrix can be readily represented in terms of the homogenized constitutive coefficients which in turn have a direct relation with homogenized material properties. Since the homogenized properties were obtained from a non-rational polynomial function in terms of the density (Equation 3.12), obtaining the derivative of the stiffness matrix with respect to the density

parameter should be available through the application of fundamental derivative theorems from differential calculus.

This completes the discussion on obtaining sensitivities of the objective function with respect to the optimization parameters for homogenization operating with B-spline based smoothing algorithm.

### **3. 6 SUMMARY**

In this chapter a thorough development of the analysis routine of the design tool based on homogenization was provided. The problems of design variable smoothing and design variable reduction were both addressed by a parametric smoothing scheme and the implementation details were presented. The sensitivity calculations for the objective function with respect to the z-heights of the control points were also discussed. The problems from expensive computations associated with evaluation of basis functions during sensitivity calculations were outlined and suggestions for improvement were discussed.

A second and final stage in the design tool development for mesostructure design is the formulation and solution of the representative plane elasticity problems. This is the subject of the next chapter.

## **Chapter 4: Design Optimization by Homogenization – Problem cases, Solutions and Results**

### **4.1 CHAPTER OBJECTIVES**

The goals of this chapter include the following:

- 1) Select test problems for design optimization.
- 2) Set up an optimization routine to minimize strain energy for the selected plane elasticity problems based on the homogenized model with the parametric smoothing scheme developed in the previous chapter.
- 3) Present design solutions of our modified homogenization method and compare them with design solutions from the SIMP method available in the literature.
- 4) Validate the results of our design tool with computational models of obtained solutions analyzed on ANSYS Mechanical 12.1.

### **4.2 PROBLEM SELECTION FOR DESIGN OPTIMIZATION**

There are certain characteristics that need to be met by the chosen design problem. These characteristics include the following:

*The problem should have been well studied in the literature and the solution to the design problem should be well known.*

1. This characteristic allows comparison of different methods that seek to find solution to the same problem. In particular, since our approach of a smoothing scheme combined with the homogenization procedure is novel, the requirement that there is a consensus among the research community with

regard to what is the best solution for the stated design problem becomes all the more important.

*The problem can be directly translated into a physical experiment with identical loading conditions and measurable response.*

2. Since, the fabrication of the resulting solutions is within the scope of this work, it makes sense to choose a problem based on whether it can be replicated physically under controlled settings and enable measurement of quantities that are of interest.

Several papers have been published on compliance minimization of a Messerschmitt-Bolkow-Blohm (MBB) beam using many types of optimization algorithms; this problem represents a simple starting exercise for beginners in topology optimization. A cantilever beam problem is also one of the most well studied design problems in the literature. These are the problems for which the best solution [44] and the analytical solution [51] at low volume fractions are readily available and in that respect serve as useful benchmarks. Further, a laboratory set up to determine the deformation displacement for an applied load in these problems is tractable with a careful experimental design. Thus, the MBB beam and the cantilever beam design are chosen as test case problems for our novel design optimization procedure.

### **4.3 DESCRIPTION OF THE TEST PROBLEMS**

#### **4.3.1 MBB Beam Problem**

The MBB beam problem shown in Figure 4.1 is one of the earliest problems studied in topology optimization and has its roots in the aircraft industry. It is a simple model of the floor of a fuselage system in an Airbus passenger carrier [75]. Today, it is



more commonly known as the simply supported beam problem, which can be solved for displacement at the center, given its cross-section, using rudimentary principles found in standard textbooks on structural mechanics. In our case, the cross-section is not known a priori and the goal of the optimization routine is to determine the distribution of material inside the domain of the MBB beam for a structure with minimum compliance.

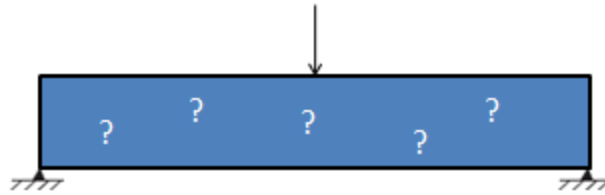


Figure 4.1: A simply supported beam – MBB problem

The MBB beam problem is symmetric with respect to the center. Accordingly, only one symmetric half of the structure is modeled, and the resulting solution is mirrored about the center. The roller constraints shown in Figure 4.2 remove two of the three degrees of freedom in a planar motion. The fixed constraint removes all degrees of freedom. The maximum displacement occurs at the center of the full beam and the x-displacement along the center line is zero.

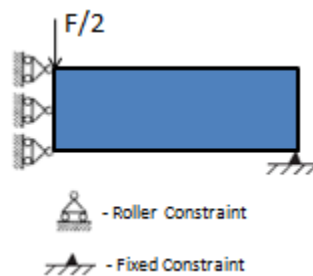


Figure 4.2: Symmetric half beam – MBB problem

### 4.3.2 Cantilever Beam Problem

A cantilever beam is also a well known problem in beam theory. Vertical and horizontal displacements are fixed on its left end, and a load is acting on the right end at the center of the beam. In both the MBB beam and the cantilever beam problems, the contribution from the self weight of the beam is ignored and only the external loads and boundary conditions are taken into account for analysis.

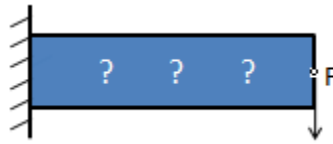


Figure 4.3: Cantilever beam problem

### 4.4 OPTIMIZATION SETUP FOR TEST PROBLEMS

MATLAB was used for developing the algorithm for the homogenization based material distribution optimization. It is necessary to understand the class of optimization problems that the design optimization of this work belongs to in order to make use of appropriate MATLAB utility functions. The optimization function, namely, the strain energy can be evaluated using the results of the finite element procedure. The constraints to the optimization function involve the limit on volume fraction that can be expressed as the sum of intermediate densities and the conservation equation of the problem, namely, the equilibrium of forces modeled using the finite element procedure. The resulting optimization problem is expressed in Equations 4.1 and 4.2.

$$\min S = \sum_{i=1}^{No.Elements} \frac{1}{2} d^{eT} K^e d^e \quad (4.1)$$

$$\text{such that} \quad K(E^H)u = f \quad (4.2)$$

$$\sum_{i=1}^N \rho_i \leq V$$

where,  $\rho_i$  represents the design variable, ' $V$ ' represents the volume fraction,  $K(E^H)$  represents the global stiffness matrix with the homogenized properties, ' $u$ ' is the displacement vector for all the degrees of freedom, ' $f$ ' represents the loads acting on the structure, ' $S$ ' represents the strain energy of the structure and the superscript  $e$  denotes the mesostructure element quantities.

Equations 4.1 and 4.2 constitute an optimization problem with linear inequality constraints. The FMINCON utility function from the optimization toolbox is well-suited for handling constrained optimization problems with both linear and nonlinear, equality and inequality constraints. It is based on the Sequential Quadratic Programming (SQP) optimization method with the option to turn on and off the gradients and hessian of the objective function. The sequence of steps in the optimization process is given below:

Step 1: Specify the number of mesostructure elements in the problem and indicate the xyz coordinate bounds for the design domain.

Step2: Specify the size of mesostructure unit cell, and the starting density values for each mesostructure unit.

Step 3: Specify the boundary conditions and loads for the problem.

Step 4: Optimize the mesostructure.

Step 4a: Generate a mesh using the mesostructure units and compute the homogenized material properties for all mesostructures using density in the homogenized material model.

Step 4b: Compute the stiffness matrix terms for each mesostructure unit

and assemble them to form the global stiffness matrix for the macrostructure.

Step 4c: Solve for the x-y displacement values at the nodal points and use these values to compute the strain energy for the macrostructure.

Step 4d: Compute the gradient of the strain energy function with respect to the design variables (densities) given by Equation 3.51.

Step 4e: Calculate the volume fraction,  $V$ , and the gradient of the volume fraction with respect to the design variables.

Step 5: Return the objective and the constraint function values and gradients to the optimization algorithm, check for convergence, and adjust the density values and return to step 4 if the algorithm has not yet converged.

Step 6: Save the converged solution – final set of converged density values of the mesostructure unit cells.

A schematic sketch of these steps is shown in the Figure 4.4.

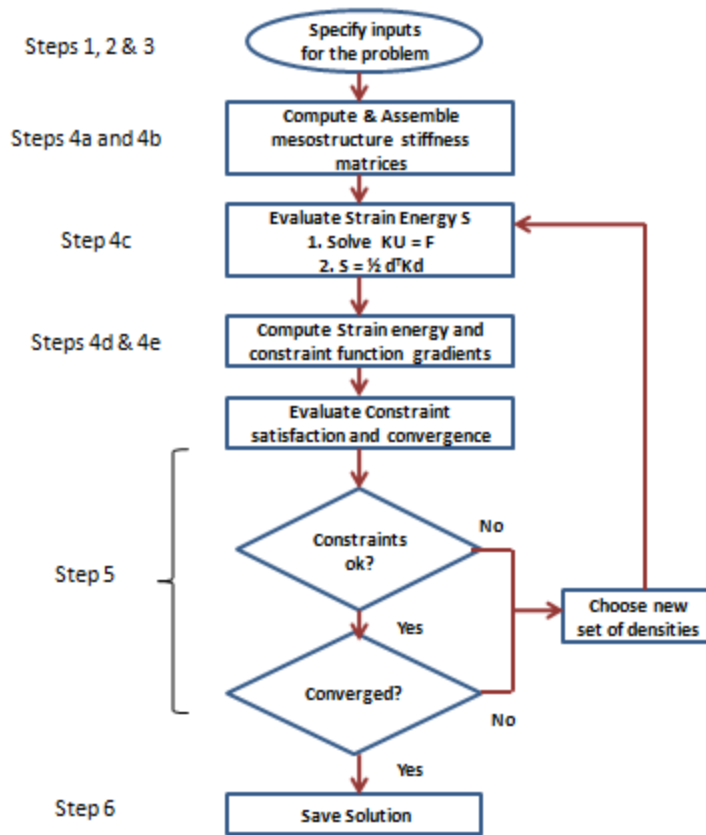


Figure 4.4 Steps in the optimization procedure

#### 4.4.1 Integrating the B-Spline Smoothing scheme with the Optimization Procedure

Since a b-spline based smoothing scheme will be integrated with the optimization scheme, the design variables for optimization will be the control points of the b-spline surface and not the density values. Therefore, the initial starting point has to be a set of control point heights that define the surface. Additionally the knot vector and order of the splines have to be fixed as parameters for the problem. A constraint on the volume fraction is still applied but, this constraint must be expressed in terms of the control point heights making it a non-linear function. Again, the FMINCON function can handle this

kind of optimization but the steps in the optimization process are modified considerably. The revised sequence of steps is shown in Figure 4.5.

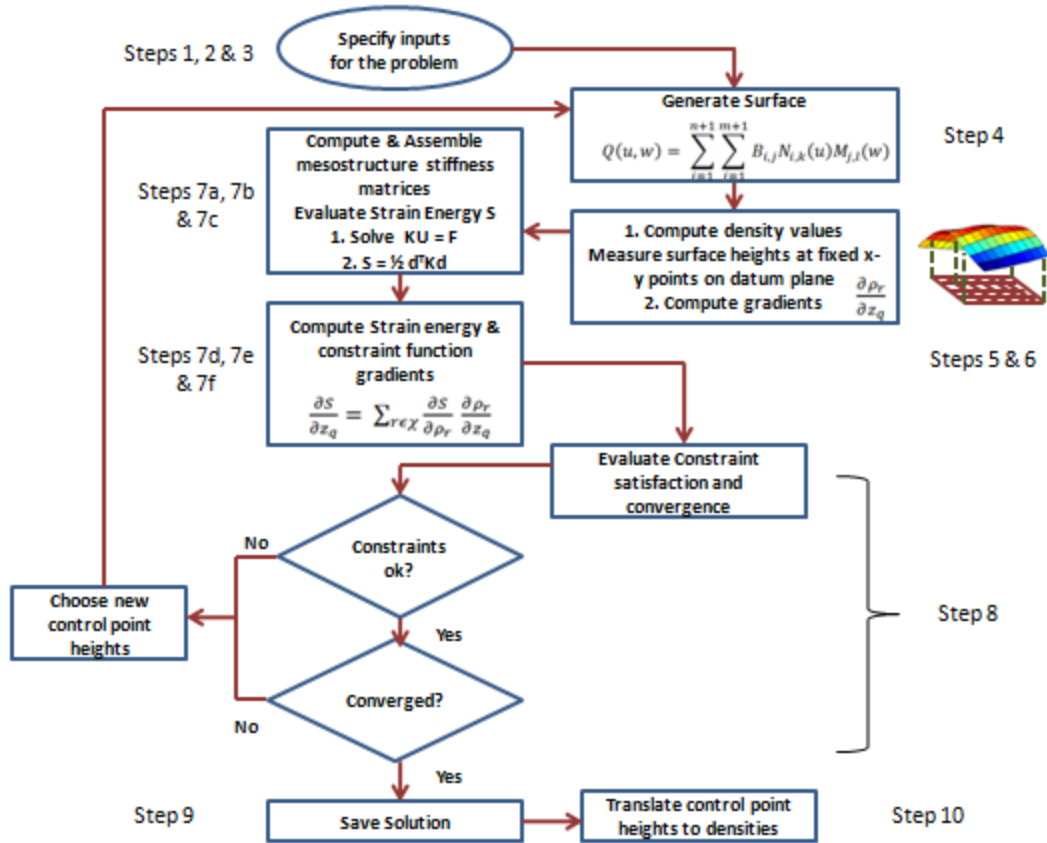


Figure 4.5: Steps in optimization with the B-spline smoothing scheme

Step 1: Specify the number of control points, knot vector and order and fixed x-y locations on a datum plane at which mesostructure densities will be computed.

Step 2: Specify the initial control point heights for optimization.

Step 3: Specify the number of mesostructure units, the boundary conditions and

loads

Step 4: Generate a surface based on information in Step 1 and 2.

Step 5: Calculate the densities of all the mesostructure units as surface height of their respective x-y points on the datum plane.

Step 6: Compute the gradients of the surface heights of the x-y points on the datum plane with respect to the control point heights using Equation 3.44 or 3.45.

Step 7: Optimize mesostructure densities using control point heights.

Step 7a: Generate a mesh using the mesostructure units and compute the homogenized material properties for all mesostructures using its density in the homogenized material model.

Step 7b: Compute the stiffness matrix terms for each mesostructure unit and assemble them to form the global stiffness matrix for the macrostructure.

Step 7c: Solve for the x-y displacement values at the nodal points and use these values to compute the strain energy for the macrostructure.

Step 7d: Compute the gradient of the strain energy function with respect to the densities given by Equation 3.51.

Step 7e: Calculate the volume fraction,  $V$ , and the gradient of the volume fraction with respect to the densities.

Step 7f: Compute the gradient of the strain energy function and constraint function with respect to the design variables (control point heights) using the chain rule given in Equation 3.40 with information from Step 7d, 7e and 6.

Step 8: Return the results of the objective and constraint functions that includes

their current values and gradients to the optimization algorithm for constraint evaluation. Return to step 4 until the optimization algorithm converges.

Step 9: Save the converged solution – final set of control point heights.

Step 10: Translate the converged control point heights to density values by following steps 3 and 4 as a material distribution solution for the problem.

#### **4.4.2 Problem Parameters**

There is a set of parameters that must be finalized to set the optimization running for the cantilever and MBB beam problem cases. These include the following:

1. Dimensions of the design domain
2. Volume fraction
3. Number of mesostructure unit cells in x and y (Alternatively, the unit cell size)
4. Number of control points in x and y
5. Upper and lower bounds on control point heights (Also, sets the limits on the density range)
6. Order and knot vector of the spline
7. Solid material properties – Young's modulus, shear modulus, Poisson's ratio
8. Loads and displacement constraints on the boundary
9. Initial guess of the choice variables for the optimization routine.
10. Convergence condition, if any



The values for these parameters require careful consideration. The volume fraction of the design domain is set to a limit of 0.4. The upper and lower bounds on control points heights (above the datum plane) are set to 0.02 and 1.0 respectively. The solid material properties are chosen to reflect the properties of Nylon 11 keeping the fabrication goals in mind. Accordingly, the young's modulus is 1500MPa, the shear modulus is 577.5Mpa and the Poisson's ratio is 0.3.

The dimensions of the design domain are linked with the mesostructure unit cell size and the number of unit cells in x and y direction. Specifying two of these parameters will fix the third one. We will show in the following discussion how to determine which of the two parameters to specify. The limits on the dimensions of the design domain are determined by the minimum feature size and the maximum part size that can be accommodated in the build chamber of a SLS machine. There is neither a possibility to manufacture anything smaller than 0.75mm (holes or wall thickness smaller than these don't come through) nor a part that is greater than 350mm in any one direction can be accommodated inside the build chamber. Keeping these values in mind, we can arrive at an optimal size for a single square mesostructure unit. Let us consider for example that the minimum density that will be encountered for any mesostructure unit in the final solution is 0.04 (4% density). Allowing 0.75mm minimum wall thickness to correspond to two adjacent mesostructure walls, we require that a density value will correspond to 0.375mm thickness of the mesostructure wall. This is shown in Figure 4.6.

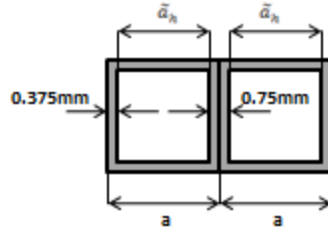


Figure 4.6: Minimum density mesostructure units possible on the SLS

The density of the cell is given by Equation 3.11

$$\rho = 1 - \frac{\tilde{a}_h^2}{a^2} = 0.04 \quad (4.3)$$

We also know from the minimum wall thickness for a single mesostructure unit that

$$a - \tilde{a}_h = 0.375 * 2 = 0.75mm \quad (4.4)$$

Therefore, substituting Equation 4.4 in Equation 4.3, we get the minimum mesostructure unit cell size that should be used if a target of 4% minimum density must be achieved during fabrication.

$$\frac{(a - 0.75)^2}{a^2} = 0.96 \Rightarrow a = 37.12mm$$

A mesostructure size of 37.12mm allows us to have a maximum of  $300/37.12 = 8$  mesostructure units in the maximum length direction. Since, for the MBB beam only a half beam needs to be modeled, this leaves us with 4 cells in the longest direction. There is really no scope for optimization with such a small number of cells. If we relaxed the limit on the minimum density that must be achieved to 19% then, the mesostructure unit size reduces to 8mm giving the possibility of having 40 unit cells along the longest

direction of the beam serving as a useful problem for the optimization procedure. An 8mm mesostructure unit size is chosen for the MBB problem.

There is a general agreement on the length to height ratio of an MBB beam with the application of the loading and displacement constraints prescribed in the literature. Lewinski *et al.* [76] used a value of 1.8 or above for the half beam problem and Sigmund [44] used a value of 1.6 in his widely distributed code for the same problem. A ratio of 3.3 is chosen for the half beam in this work. The choice is based on requiring at least 6 cells in the direction of the height of the beam so that the optimization routine with the smoothing scheme is not overly constrained.

For the cantilever beam, 16 cells were chosen in the length direction and 10 cells were chosen in the height direction. The choice of the number of cells was again governed by similar values in literature (1.6 in [44]). It was ensured that the optimization load was nearly the same in both beam problems – 120 (20 x 6) for the MBB beam and 160 (16 x 10) for the cantilever beam. A smaller number of total mesostructures in the cantilever as compared to a full MBB beam allowed us to choose a larger unit mesostructure size for the cantilever case. A 12mm unit size was chosen for the cantilever case. As a result, for the cantilever case densities as low as 12% can be achieved ( $1 - \frac{11.75^2}{12^2}$ ).

Design variable reduction was kept at 50% for both cases. The number of control points for the MBB problem was 60 (10 x 6) and the number of control points for the cantilever problem was 80 (8 x 10). The number of control points in the height direction was intentionally kept the same as the number of mesostructure units in the same direction for both cases. This helps eliminate over smoothing of the densities by the B-spline algorithm. To understand over smoothing, let us consider there were only 5 control points in the height direction for the cantilever beam. If each control point influences at

least two cells, then there are simply not enough control points in this direction to allow gradual transition of densities from solid to void regions in the solution.

Third order polynomials were used to construct the surface patches for each problem (biquadratic surface patch). A biquadratic patch is of an order high enough to ensure continuity and at the same time low enough to limit the influence of any control point to a small neighborhood of mesostructure unit cells. An open uniform knot vector is used for surface generation.

The displacement boundary conditions were shown in Figures 4.2 and 4.3 for the two cases. The applied load should be restricted to induce deformations that are in the linear elasticity region of the material. Since, this is a simulation and the governing equations are from linear elasticity theory, the applied load is not much of a concern and a load of 1N causing strains on the order of  $10^{-4}$  was chosen

This leaves us with the initial guess and the convergence criteria as the only two parameters to be decided for the optimization procedure. Convergence criterion is set by default to a  $10^{-6}$  change in the objective function values in MATLAB. As we are already in the  $10^{-4}$  order of strain values, a  $10^4$  scale factor was applied to the computed strain energy values and the default convergence criteria from MATLAB were accepted for our purpose. Starting guesses were chosen appropriately to speed up convergence from the knowledge of analytical solutions in [74 & 76]. Table 4.1 summarizes the discussion of this section.

<b>Problem parameter</b>	<b>MBB (Half beam)</b>	<b>Cantilever</b>
Design domain size	160 x 48 x 22mm <sup>3</sup>	192 x 120 x 20mm <sup>3</sup>
Number of unit cells	20 x 6	16 x 10
Number of control points	10 x 6	8 x 10
Control point height limits	0.02-1.0	0.02-1.0
Order	3	3
Knot vector	Open uniform	Open uniform
Material properties	Nylon 11	Nylon 11
Applied Load	1N	1N
Convergence	FMINCON default	FMINCON default

Table 4.1 Summary of the problem parameters for the optimization routine

#### 4.5 PERFORMANCE EVALUATION OF SOLUTIONS FROM THE HOMOGENIZATION ROUTINE

The solutions of the homogenization routine with integrated B-spline smoothing can be compared against the SIMP based implementation scheme available from Sigmund [44]. The parameters for comparison of solution quality include the objective function value of the converged solution and the maximum deformation experienced by the two beam cases at the point directly under the action of the load. The design solutions from the SIMP routine for the half beam and its corresponding full beam are shown in Figure 4.7



Figure 4.7: SIMP solution for the MBB beam problem – Full beam and half beam

The design solutions from the Homogenization routine with B-spline smoothing for the half beam and its corresponding full beam are shown in Figure 4.8

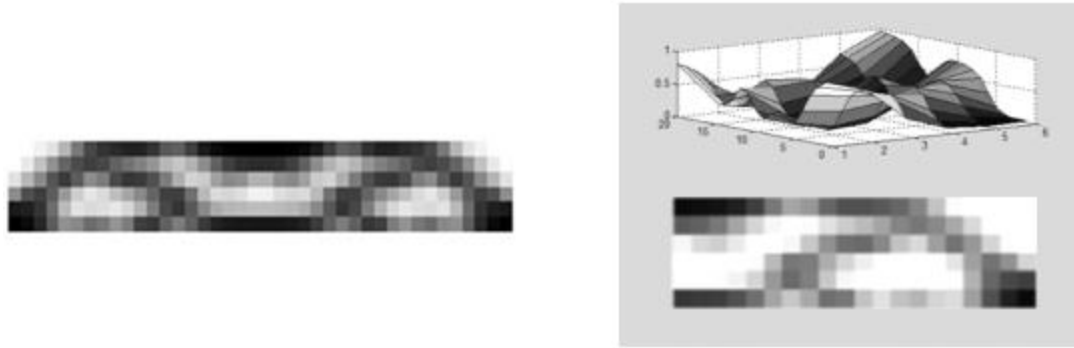


Figure 4.8: Homogenization with B-spline smoothing solution for the MBB beam problem – Full beam and half beam

The solutions for the MBB problem presented in Figures 4.7 and 4.8 show a truss type layout. The homogenization method with mesostructure substitution has more grey regions in its solution. The SIMP routine explicitly drives the solution away from grey regions using a penalization scheme

The design solutions from the SIMP and the Homogenization routine with B-spline smoothing for the cantilever beam are shown in Figure 4.9. Again for the cantilever problem the solutions from SIMP represent a truss type structure and the homogenization solution has greyer regions.

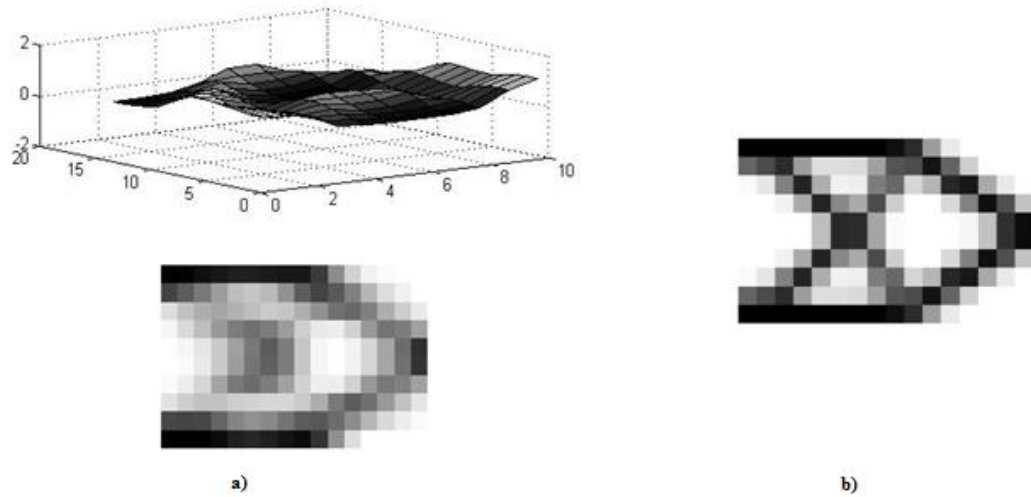


Figure 4.9 Cantilever problem – a) Homogenization with B-spline smoothing solution (HOMOG-B) b) SIMP solution

The comparison of the solutions based on performance parameters strain energy and maximum displacement is shown in table 4.2

Applied Load – 1N			
Case		Strain Energy ( $\times 10^{-3}$ Nmm)	Maximum Displacement ( $\times 10^{-3}$ mm)
Cantilever	SIMP	0.0023	0.0023
	HOMOG-B	0.0051	0.0051
MBB	SIMP	0.0045	0.0090
	HOMOG-B	0.0054	0.0109

Table 4.2: Comparison of design solutions – SIMP vs. HOMOG with B-Spline

The difference in the performance based on the strain energy and maximum displacement can be explained as follows. Firstly, the homogenization algorithm with the B-spline smoothing scheme combined with 50% design variable reduction used in this

study is a large smoothing that significantly impacts the quality of the final solution. It would be useful to study in a future work if whether a smaller percentage design variable reduction gives better results. A second important factor for the difference in the strain energy value and maximum displacement values lies with the inaccuracy of the SIMP model in correctly estimating the performance parameters. The SIMP approach as discussed in chapter two uses a power law material model which is not a good approximation of the material properties for intermediate density values. To test this hypothesis, the SIMP solutions were run through the analysis routine of the homogenization method with B-spline smoothing and the computed strain energy and maximum displacement values were compared with the HOMOGB results shown in Table 4.3.

Case		Strain Energy (x 10 <sup>-3</sup> Nmm)	Maximum Displacement (x 10 <sup>-3</sup> mm)
Cantilever	SIMP on HOMOGB	0.0024	0.0024
	HOMOGB	0.0051	0.0051
MBB	SIMP on HOMOGB	0.0043	0.0086
	HOMOGB	0.0054	0.0109

Table 4.3: Performance parameters of SIMP solution recomputed on HOMOGB analysis routine

As it can be observed there was no significant in the estimated performance parameters and it turns out that the SIMP approximations were not very inaccurate proving our hypothesis false. The accuracy of the SIMP approximation is partly due to the converged nature of the final SIMP topology, with few intermediate density elements. So, we conclude that the lower stiffness of the solutions really rest on the excessive



smoothing during design variable reduction with the B-spline smoothing scheme. Although the SIMP solutions are stiffer than the HOMOGENEOUS-B solutions, it is not appropriate to conclude that the SIMP solutions are preferred. The designed mesostructures (which can be obtained with the HOMOGENEOUS-B algorithm but not with the SIMP algorithm, for reasons discussed previously in this section) may offer several advantageous properties. For example, the large number of cell walls from a smoothly distributed mesostructure are likely to exhibit superior buckling failure, relative to the truss-like solutions obtained by the SIMP algorithm. Cell-like structures have also been shown to provide exceptional structural energy absorption and heat transfer capabilities [69].

#### 4.6 VERIFICATION OF DEFORMATION DISPLACEMENT WITH ANSYS MODELS

The results obtained for the design problems were verified for their correctness by modeling the solutions in ANSYS Mechanical 12.1. A solid Quad4node (42) element was used as before in chapter 3 and the mesh density was kept at least 2 elements per cell wall. The densities were used to build the geometry. Every density value can be converted into a unique size for the hole inside the square mesostructure. Therefore, if given the coordinates for the mesostructure the coordinates of the hole can be computed. For instance, let us consider the MBB beam problem. The mesostructure unit size is 8mm. Let the density of a particular mesostructure unit be 0.76. The hole size can be calculated using Equation 3.11.

$$\rho = 1 - \frac{\tilde{a}_h^2}{8^2} = 0.76 \Rightarrow \tilde{a}_h = 3.92mm \quad (4.5)$$

The coordinates of the mesostructure and its hole for the calculation in Equation 4.5 is shown in Figure 4.10. If the resulting cell wall was less than the manufacturable limit, then the density was rounded to zero, and the mesostructure unit cell was eliminated.

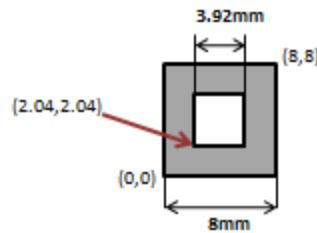


Figure 4.10 Density to mesostructure geometry conversion

The procedure can be repeated for all densities to calculate the hole sizes and an APDL (ANSYS Parametric Design Language) code can be written to automate the procedure of creating the geometries for both the SIMP and the HOMOGENEOUS-B solutions of the cantilever and the MBB beam problems. It is to be noted here that although only the HOMOGENEOUS-B routine interprets density values to an underlying mesostructure, we have extended the same interpretation for the SIMP method too. The inaccuracy from such an interpretation for SIMP will be under tolerable limits only if there are very few intermediate density regions in the final solution of the SIMP method. Fortunately, for the two beam problems this condition is met as the filtering scheme of the SIMP method drives most of the density values in the final solution close to either zero or one.

Boundary conditions were replicated to solve the model and verify that the maximum displacements obtained for the two beam cases on two different schemes – the

SIMP and homogenization with mesostructure substitution, are close enough with that predicted by the ANSYS Mechanical results.

The meshed model with its loads and boundary conditions for the two MBB beam cases and the two cantilever beam cases in ANSYS Mechanical 12.1 are shown in Figures 4.11 and 4.12 respectively.

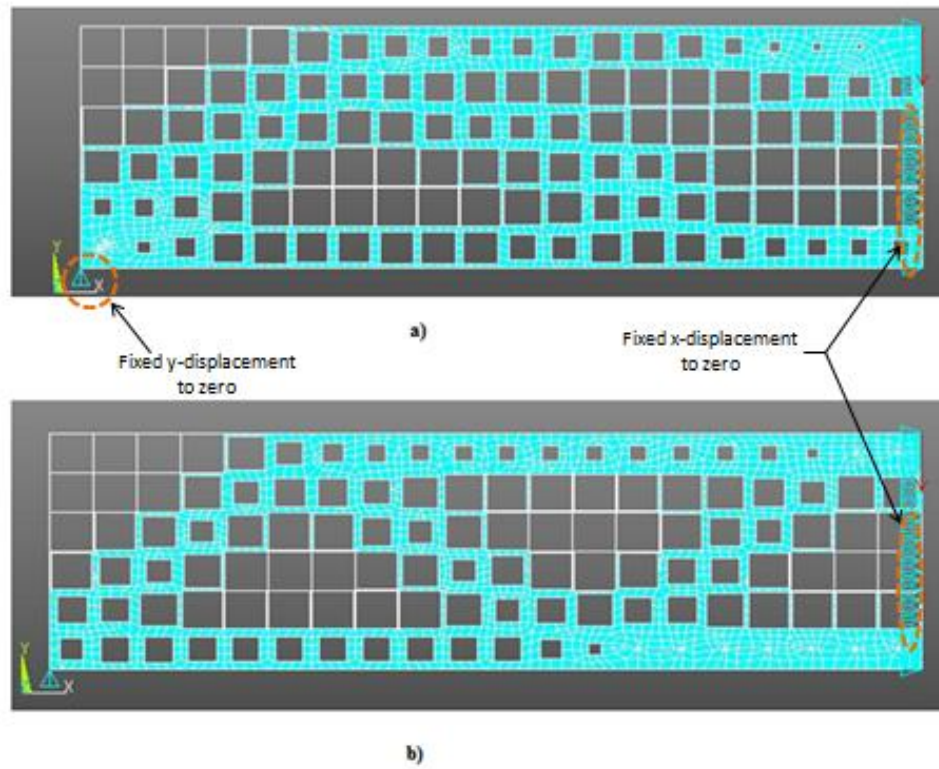


Figure 4.11 ANSYS MBB Models a) HOMOG b) SIMP

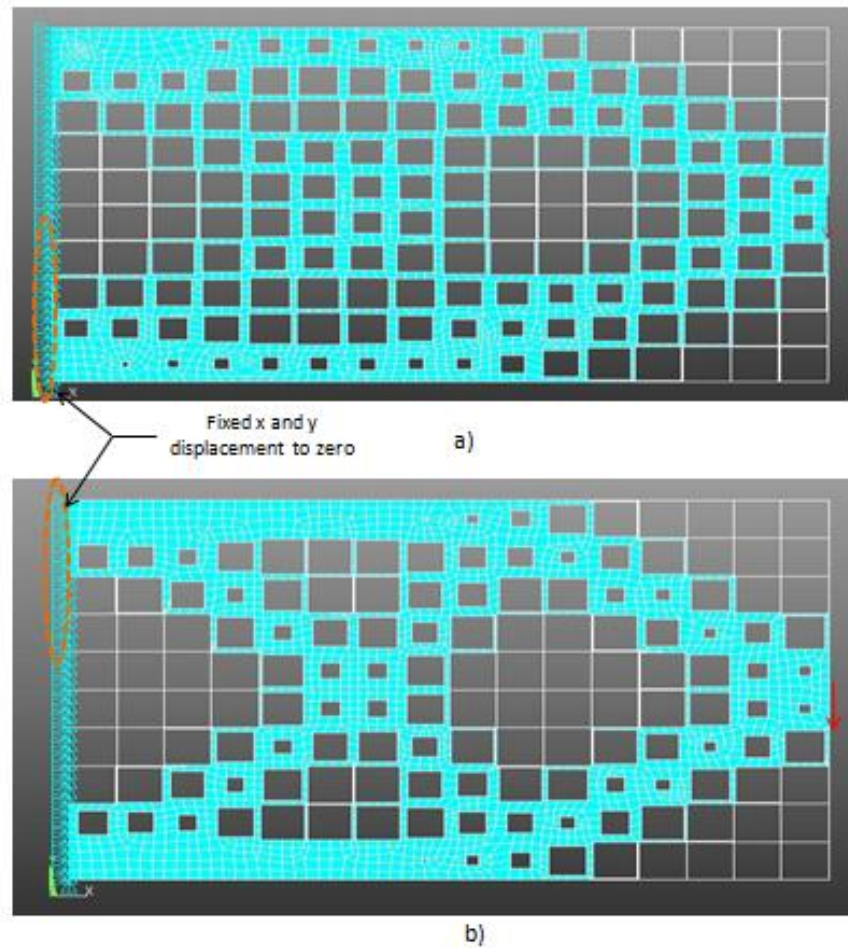


Figure 4.12 ANSYS Cantilever Models a) HOMOG b) SIMP

The results of the comparison are presented in the Table 4.2

Case		Maximum Displacement at 1N (mm)	
		SIMP solution	Homog-B solution
Cantilever	MATLAB	0.00235	0.004803
	ANSYS	0.00269	0.004979
MBB	MATLAB	0.00810	0.011800
	ANSYS	0.00780	0.010800

Table 4.2 Verification of results – ANSYS & MATLAB

It can be observed that excellent agreement was obtained with the computational model for all four cases with respect to maximum displacement predictions (average deviation <7%). This small error can be attributed to the approximation of the homogenized material model for a macrostructure substituted with mesostructure geometries, the errors associated with finite element analysis and numerical round off.

#### **4.7 SUMMARY**

This chapter provided a very detailed insight into the application of the developed design tool for two practical test design problems. The steps in optimization were discussed. The significance of the design variable reduction and design by tailored mesostructure were brought out in this chapter. It turns out that we did not achieve a significant improvement in the stiffness for the MBB and cantilever problems using our homogenization with B-spline smoothing design tool on the chosen performance parameters (strain energy and maximum displacement). But we have addressed several key issues in design by homogenization.

- 1) A filtering scheme is no longer required in the presence of the B-spline smoothing technique.
- 2) A successful interpretation for intermediate densities in the design solution has been presented so that complex mesostructures can be additively fabricated.
- 3) The implementation of a design variable reduction, via B-spline smoothing procedure and the computation of associated derivative quantities for use in gradient based algorithms have been demonstrated.

- 4) The developed design tool is independent of the optimization search method and the MATLAB FMINCON function can be substituted with other suitable approaches.

In the next chapter, we study the characteristics of the fabrication process for our obtained design solutions and devise experimental testing procedures and present the results from these tests as a final validation for our design methodology

## **Chapter 5: Fabrication of Designed Mesostructure through SLS and Experimental Testing of Parts – Details and Results**

### **5.1 CHAPTER OBJECTIVES**

The goal of this chapter is to provide details of the experimental validation for the designs obtained using the homogenization routine with the B-spline smoothing scheme. Both homogenized designs and SIMP solutions are fabricated additively with SLS and subjected to experimental tests that match the boundary conditions applied to the optimization problem. It is also in the goal of this chapter to elucidate some of the fabrication characteristics for the mesostructure designs on the SLS process.

There are several steps between a material distribution solution from topology optimization and actual fabrication of the parts. For example, it is important to understand the influence of part orientations inside the build chamber on minimum resolvable dimensions for the mesoscale features of the design solutions. Further, in order that the fabricated parts can be evaluated, testing methods need to be set up for the MBB and cantilever cases. In the following sections, the steps to design for fabrication and testing will be discussed in detail.

### **5.2 CONVERSION OF DESIGN SOLUTIONS TO CAD MODELS**

The design solutions presented in chapter four were material distribution solutions. The technique to convert the material distribution information into a material geometry specification was discussed in the validation with ANSYS section in Chapter 4 (Section 4.6). For fabrication with an AM process, it is not enough to know the geometry details in the form of coordinate vertices of different points. There is a need to construct a

CAD model specifying the plane and volume elements in the design domain formed from these vertices in an STL (stereolithography) format developed by 3D systems. MATLAB was used to convert the material distribution information into coordinate points using the theory of Section 4.6 and subsequently to surface patches connecting these vertices using built-in functions. The code to convert patch information to an STL file format is freely distributed by many authors. One such code from Sven Holcombe [77] was used in this work. Thus, CAD models of the material distribution design solutions for all four cases were created for fabrication according to the procedure in Figure 5.1.

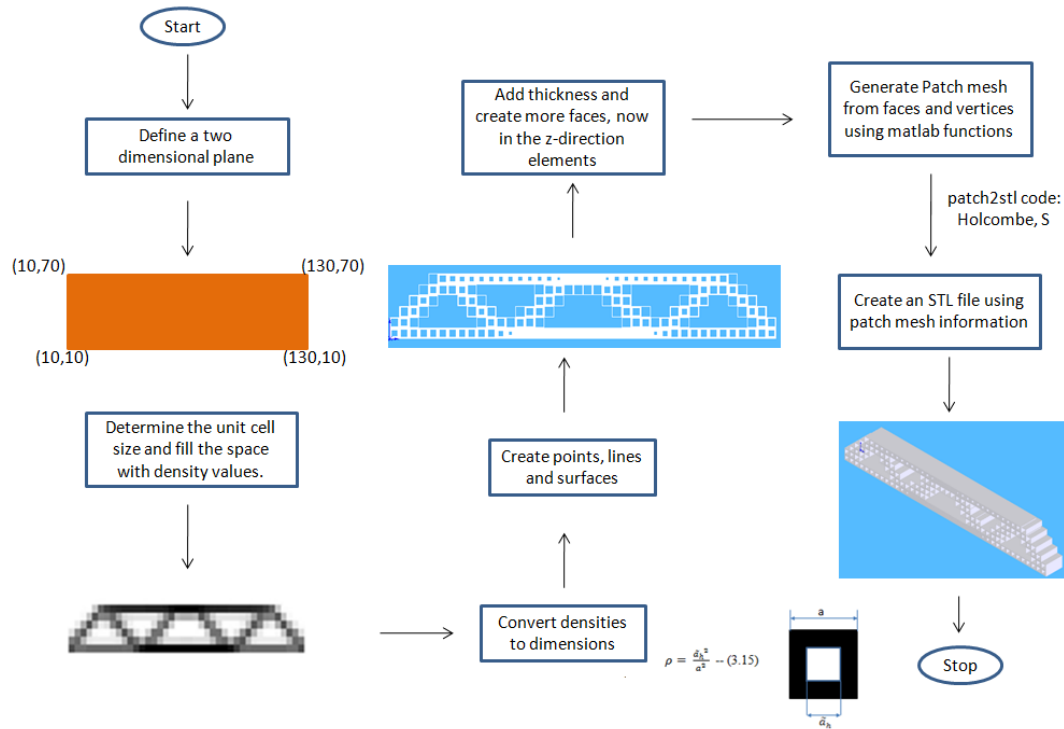


Figure 5.1: Steps in the conversion of Optimization results to CAD model – Illustration with an MBB case



The inputs to the STL conversion routine include the size of a single mesostructure cell, the number of meso-cells in the x and y direction, the densities of all the meso-cells and a user defined name for the resulting STL file. The STL files opened using SolidWorks are shown in Figures 5.2 and 5.3.

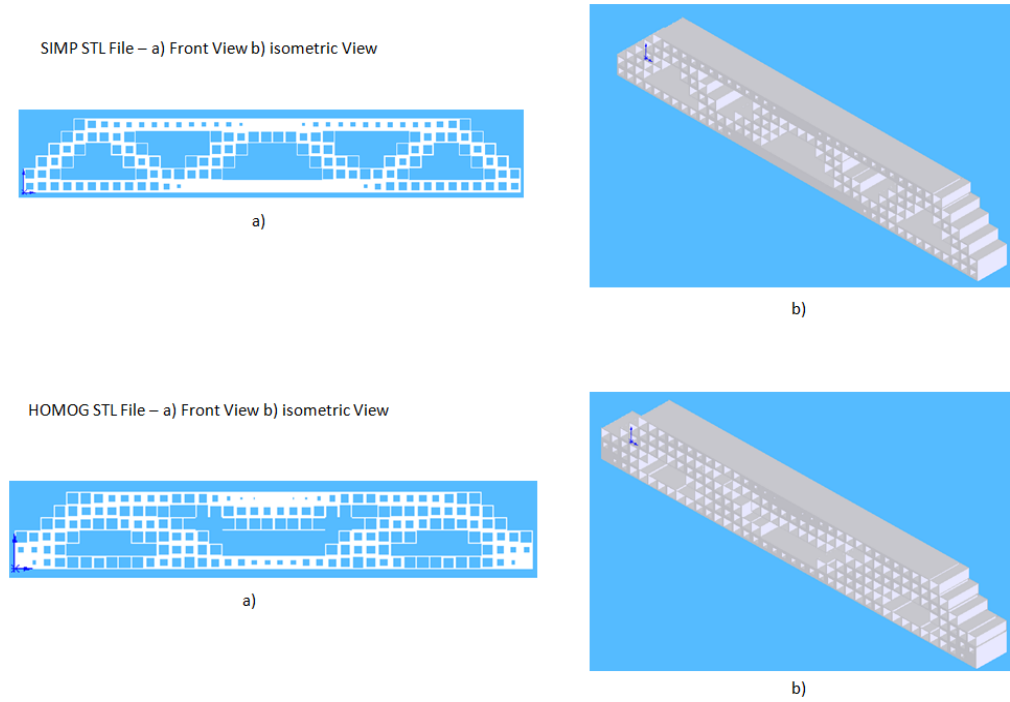


Figure 5.2 CAD models for the SIMP and the HOMOG-B design methods – MBB beam

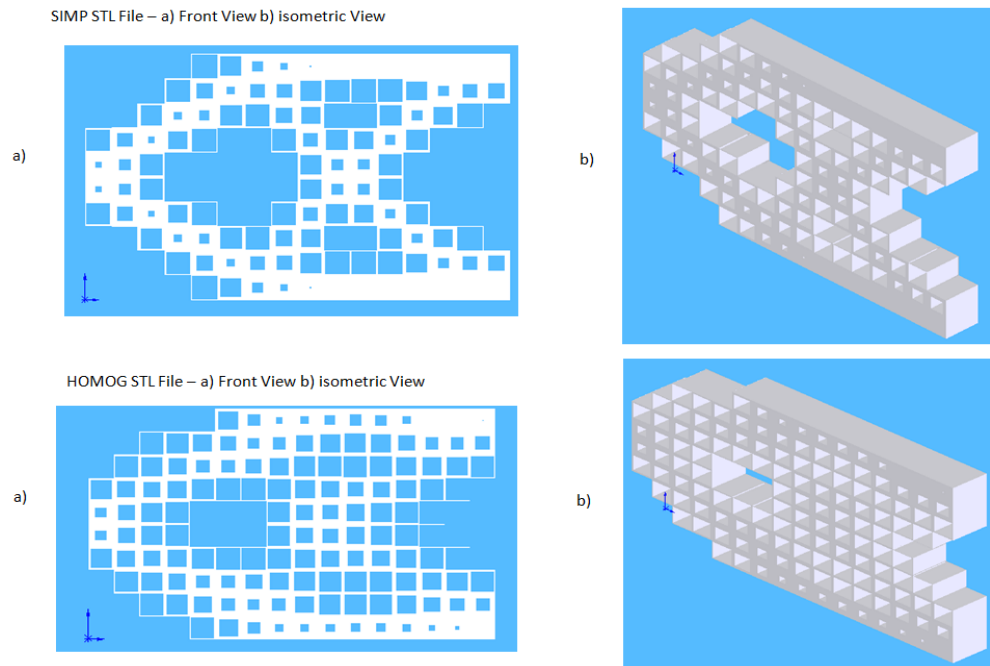


Figure 5.3: CAD models for the SIMP and the HOMOG-B design methods – Cantilever beam

### 5.3 DESIGN FOR FABRICATION AND TESTING

Design for fabrication and testing involves consideration of following parameters:

1. Determination of ideal orientation of the part inside the build chamber
2. Determination of minimum wall thickness and hole size possible with SLS
3. Conditions affecting the final dimensions of the part, including inaccuracy of the process in fabricating specified dimensions, and accommodations for testing procedures.

### 5.3.1 Experimental Studies for Build orientation, Wall thickness and Hole size

A test part was set up to determine the minimum feature size for thin walls and small holes and the best part orientation at which these fine details could be reproduced consistently. Sample specimens with increasing hole size starting from 0.5 mm to 1.9mm in steps of 0.1 mm were built using Nylon 11 powder on Sinterstation<sup>®</sup> HiQ<sup>™</sup> machine from the 3D<sup>®</sup> Systems corporation. The machine with the build chamber directions are shown in Figure 5.4. The wall thicknesses were designed starting from 0.15mm to 0.95mm in steps of 0.1mm.

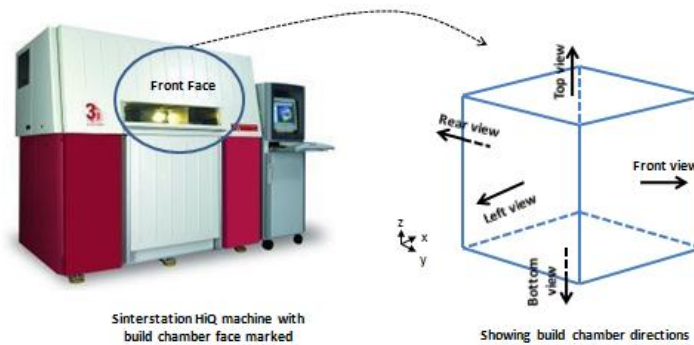


Figure 5.4: Sinterstation HiQ machine showing build chamber view direction adopted in this work

The machine parameters for Nylon-11 are given in Table 5.1 and the orientation of the parts in the build chamber is shown in Figure 5.5.

Build parameters	Set value
Part bed temperature	187°C
Layer time	20 s
Laser power	38 W
Roller feed rate	10 in/s
Scan spacing	0.010 in
Powder layer thickness	0.004 in

Table 5.1: Sinterstation HiQ build parameters for Nylon-11 powder

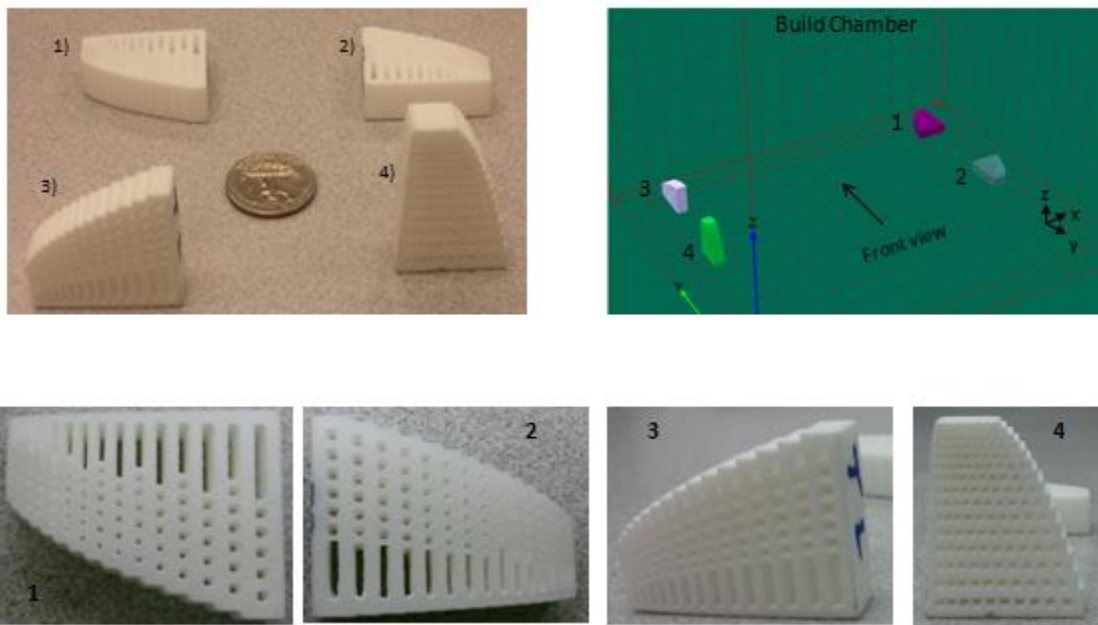


Figure 5.5: Sample specimens (top) and their zoomed views (below) with their relative orientations in the build chamber indicated by matching numbers

The experiments indicated that vertical orientation of thin walls with holes in the y-z plane (part 4) allows for the best reproduction of meso scale features – smallest possible holes, thinnest possible walls and repeatability of these features. A thin wall that is 0.9mm or thicker was consistently reproduced irrespective of the orientation. In the

orientation of part 4, a wall thickness of 0.5mm or greater was consistently guaranteed. Therefore, the orientation of part 4 with a minimum wall thickness of 0.75mm (allowing a safety factor of 0.25) was chosen as the fabrication specifications for part designs. A 0.75mm limit was placed on the minimum possible hole as well. This was based on the fact that hole size greater than 0.5mm were repeatable on part 4 orientation and a safety factor of 0.25mm was fixed. Occasionally, minimum hole size and thin walls as low as 0.3mm, but they were not consistently fabricated. A digital caliper was used for measuring all these dimensions. The safety factor also allows us to account for any errors that could have occurred in the measurement procedures.

The reasons that part 4 orientation serves as the best orientation for the mesoscale features lies in the fact that this is the only orientation in which the advantages of a small layer thickness (0.1mm) and the absence of frequent need to turn the laser light on and off for holes and walls can both be leveraged during part fabrication. The results of the study are presented in Table 5.2

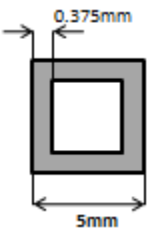
Minimum possible hole size	0.75 mm
Minimum possible wall thickness	0.75 mm
Selected Orientation	Orientation No.4

Table 5.2: Results of the experimental study

Another important result that was observed from this experimental study was repeatable hole size deviations. For example, if a hole size of 0.5mm was specified in the CAD model, most of the holes with this dimension ended up as a 0.6mm hole (an error of 20%) in the final fabricated specimen. Therefore, a second study was conducted to predict the expected deviation on hole sizes and study the effect of this deviation on the mechanical behavior of design solutions.

### 5.3.2 Experimental Study to Determine the Impact of Hole Size Deviations

A test sample of the homogenization with B-spline smoothing design solution was designed for testing on a Instron 3-point bending equipment to analyze hole size deviations and determine their impact on the behavior of the final part. The available span on the Instron machine was 220mm. Mounts were required to secure the beam on the fixtures of the machine. Providing 10mm space for the mount designs on either side leaves a total length of 200mm (220-20) for the mesostructure units. Since the MBB beam has 40 mesostructure units in the length direction, an available span of 200mm will yield a mesostructure unit size of 5mm (200/40). Using this mesostructure size it is possible to calculate the minimum achievable density in the fabricated structure. The smallest wall thickness possible in fabrication is 0.75mm. Therefore, the smallest achievable density is 0.28. This is shown in Figure 5.6.

$$\rho = 1 - \frac{(5 - 0.75)^2}{5^2} = 0.28$$


The diagram shows a square mesostructure unit with a side length of 5mm. Inside the square is a smaller square hole with a side length of 0.375mm. The wall thickness of the square is indicated as 0.375mm. The overall dimensions are labeled with arrows and text: 5mm for the outer side and 0.375mm for the inner hole side.

Figure 5.6: Smallest achievable density for 5mm mesostructure unit size

This implies that any density value less than 28% will be converted to an empty cell during SLS fabrication. Thus, as a note for the testing procedure on final parts, the span of the Instron machine is clearly not sufficient for the MBB problem if a reasonable range of mesostructure densities need to be captured. But, here the focus is to study the fabrication inaccuracy on hole sizes and not an experimental evaluation of our design solutions. Therefore, there is no harm caused by losing density values as high as 28%. The mesostructure unit size of 5mm also fixes the height of the beam as there are 6 cells

in the height direction and so the height is (6x5) 30mm. The depth of the beam is fixed as 20mm to enable a plane stress approximation for the MBB beam problem (less than  $1/10^{\text{th}}$  of the maximum dimension – 220mm). A schematic sketch of the final part with appropriate mount designs for the test fixture is shown in Figure 5.7

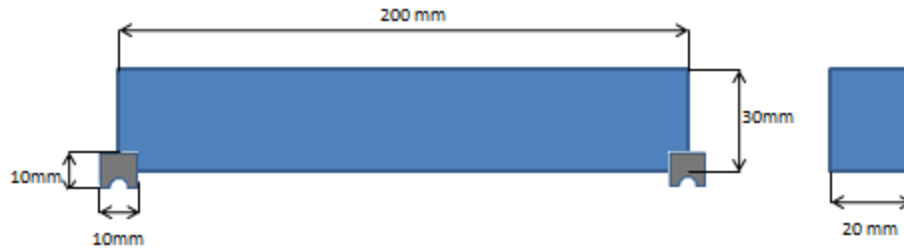


Figure 5.7 Schematic sketch of the MBB beam with mounts for the experimental study on hole size deviations

The fabricated part with 5mm mesostructure unit size was measured for hole size deviations and the results are presented in Figure 5.8. Nylon-11 powder was used for fabrication and the parameters shown in Table 5.1 were used with the fabrication machine. Of the 240 mesostructure units, 160 holes were actually measurable and the data was used to construct the plot in Figure 5.8.

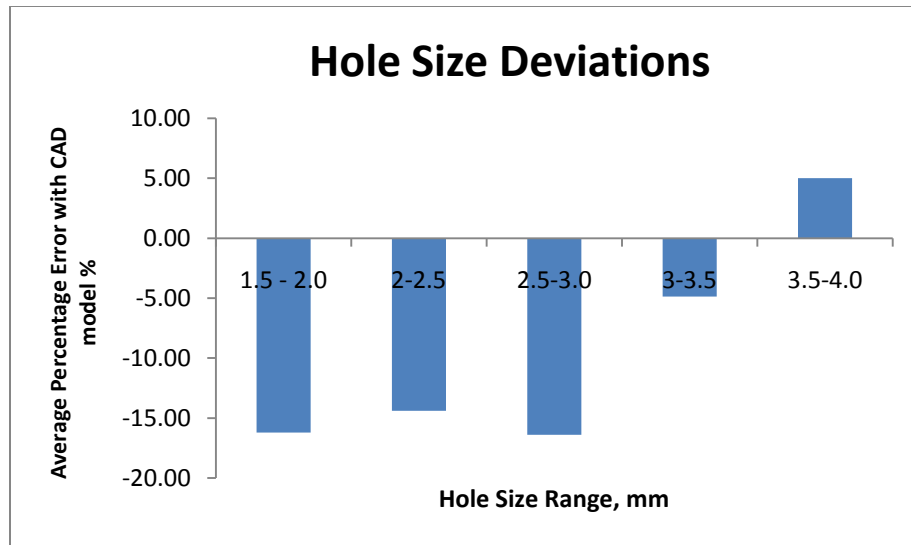


Figure 5.8: Error in measured hole sizes on the actual part against the CAD model for different hole size ranges

It can be observed that around 5% positive deviation for a hole size of 4.0 mm would give a maximum possible hole size of 4.2mm.

The impact of these hole size deviations on the structural behavior was studied by subjecting the fabricated MBB beam to an experimental test on the Instron machine and comparing the maximum displacement values with those from the numerical analysis model of the homogenization with B-spline routine at different loads. The set up is shown in Figure 5.9.



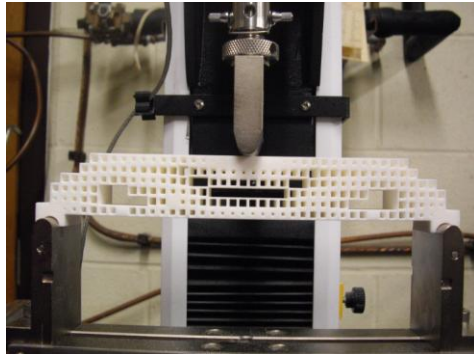


Figure 5.9: Test part on the Instron 3-point bending equipment

In order to compare similar part results, the input density file for the analysis routine was adjusted by converting results of Figure 5.8 into density variations and incorporating them into the input file. Each of the density value was adjusted by first identifying the hole size range to which it belongs and then correcting its value based on the deviations for each range presented in Figure 5.8. The comparison results from the plane stress and plane strain models with the experimentally measured values on the Instron machine are shown in Figure 5.10.

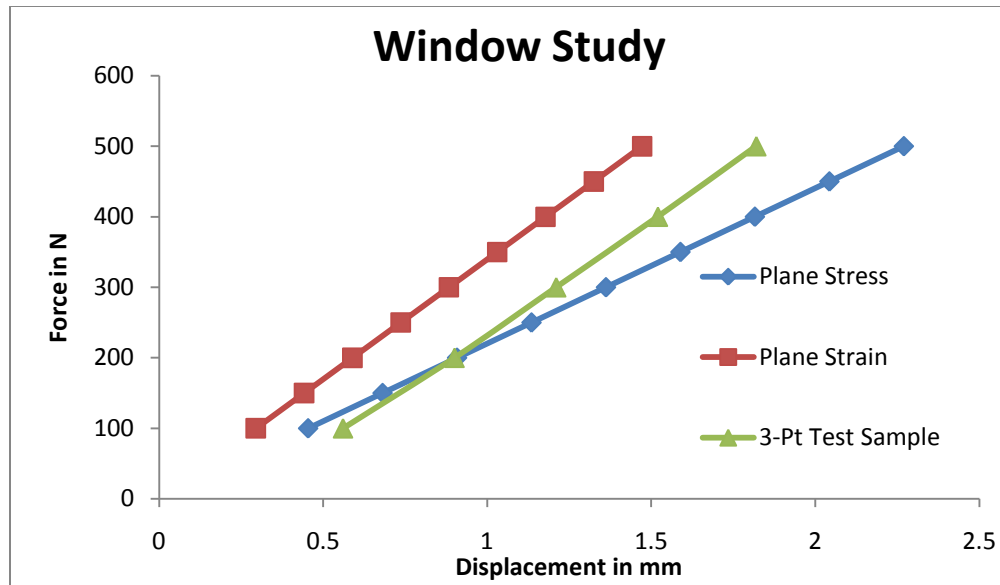


Figure 5.10: Comparison of numerical routines with experimental values for the MBB beam in the hole size deviation study

As seen from Figure 5.10 the results of the displacement were much closer to the plane stress model than the plane strain model which validates the length to thickness ratio of less than 1/10. Further, a good agreement (overall 10% deviation) of the measured maximum displacement values with the numerical analysis routines implied that the variations can be anticipated, and built into the final solution of the design methodology by incorporating appropriate adjustments.

### 5.3.3 Discussion of the Test Apparatus for Experimental Measurements

The dimensions of the parts are constrained by both the maximum allowable part size allowed in the build chamber and the testing apparatus. The build volume of the Sinterstation HiQ machine is 330mm(W) x 330mm(D) x 381mm (H). Since the orientation of our parts is fixed to No.4 orientation discussed in the section 5.4.1, the length of the beams will be in x-y plane and are therefore limited to a maximum

allowable length of 330mm in this direction by the specifications of the Sinterstation HiQ SLS machine. For the MBB beam, the span length of the available Instron testing equipment was not sufficient. For the cantilever case there was no existing testing equipment that could be used to replicate boundary and loading conditions. Therefore, a test set up was designed using available devices and equipment.

### 5.3.3.1 MBB Beam Test Apparatus

A lathe chuck was found to be suitable for mounting the MBB beam and conducting a 3-point bending test by hanging weights from the center by means of a rope. The chuck has a hole at the center that serves to hold the spindle of the lathe. This hole can be used for passing the rope to hang the weights. The chuck jaws allowed a total span of 340mm and since the maximum length on the SLS machine was 330mm testing equipment was no longer limiting the dimensions of the parts for the MBB beam. Mounts were designed for the MBB beams to help rest securely on the jaws of the lathe chuck. A solid unit cell was added as a mount on either side for the MBB beam. Mount design details are shown in Figure 5.11



Figure 5.11: Mount designs for the MBB beam

The test set up is shown in Figure 5.12. To measure displacements at the center of the beam a standard burette stand from the chemistry laboratory was used to mount a Starret Dial Indicator that had a least count of 0.001 in (0.0254mm).



Figure 5.12 Test set up equipment – Dial Indicator, MBB SIMP case and weights

Care has to be taken to ensure that the chuck is mounted on two level tables with sufficient gap between them to let the weight from center pass through the hole into this gap. A nylon-polypropylene rope that can withstand a load limit of 90lb was used to suspend the weights on the structure.

### ***5.3.3.2 Cantilever Beam Test Apparatus***

The cantilever beam was clamped by a table vise with an addition of two machined blocks that served to extend the height of the vise clamp through the entire height of the cantilever beam. An additional clamp secured the cantilever tightly with the two blocks at the top thus preventing any slippage. Mounts were designed for hanging load at the center of the right end and provision was given on the left end to provide clamping space for the vise blocks. The designs are shown in Figure 5.13.

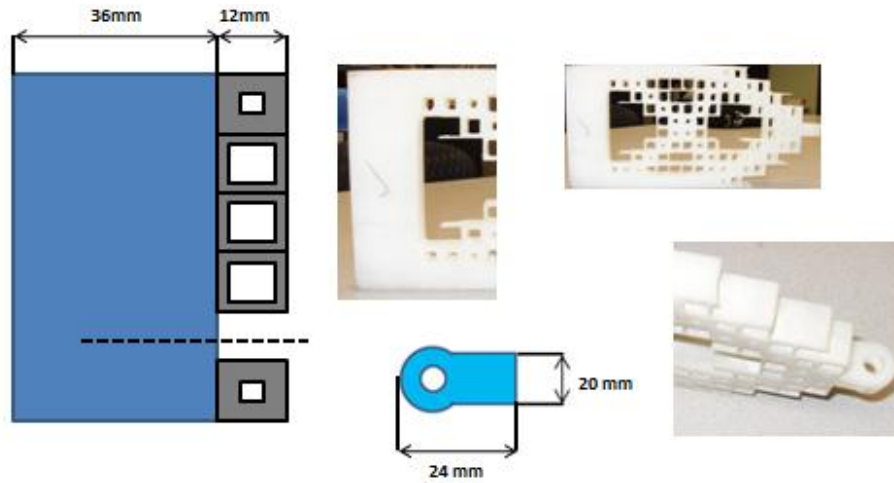


Figure 5.13: Front view of the provision for clamping space at the left end and top view of the load mount design at the right end of the cantilever beam

The set up of the cantilever on the apparatus is shown in Figure 5.14. Again the Dial indicator was attached to a burette stand and used for displacement measurements.



Figure 5.14: Cantilever beam test set up – Dial Indicator, Vise blocks, weights and clamp at the top

## 5.4 FINAL DIMENSIONS OF FABRICATED PARTS

It can be concluded from the previous discussion that a number of factors affected the dimensions of the final parts for fabrication. We will quickly summarize them here and provide a set of final dimensions of the parts for the two beam problems.

### 5.4.1 MBB Beam

The mesostructure unit cell size needs to be 8mm for achieving a lowest possible density of 19% in the design solution ( $1 - \frac{7.25^2}{8^2}$ ). This calculation takes the minimum possible wall size as 0.75mm. Since the mesostructure has 40 x 6 unit cells, a mesostructure size of 8mm fixes the length and height of the beam to 320mm (8x40) and 48mm (8x6) respectively. The total allowable span of the beam from fabrication limits is 330mm and 340mm from test apparatus (length of travel of lathe chuck jaws). The fabrication limit can be relaxed slightly if the beam was built at an angle on the x-y plane instead of parallel to the x or y-axis. Using this to our advantage, we provide 16mm room for mounts along the x direction on the 320mm beam giving a total length of 336mm (320 + 2\*8) in length and 8mm room along the y-direction giving a total height of 56mm (48+8). The depth of the beam is limited by the depth of the jaws and plane stress theory requirements ( $<1/10^{\text{th}}$  of the longest dimension). It is fixed at 22mm. The final part dimensions are shown in the model in Figure 5.15.



Figure 5.15: Dimensions of the MBB beam – SIMP and HOMOG-B

### 5.4.2 Cantilever Beam

The mesostructure unit cell size is chosen as 12mm for the cantilever beam because there is a much smaller number of cells in any one direction than the MBB beam for this case. A minimum density of 13% can be achieved by choosing a larger unit size ( $1 - \frac{11.25^2}{12^2}$ ). The number of mesostructure units in the cantilever case is 16 x 10. Therefore, the length and height of the beam are 192mm (12x16) and 120mm (12x 10) respectively. An additional room of 36mm is provided to help secure the beam between the vise blocks and 24mm is needed on the right end for load mount design shown in Figure 5.13. Therefore, the total length of the beam is 252mm (192+36+24). The depth of the beam is fixed at 20mm according to plane stress theory requirements ( $<1/10^{\text{th}}$  of the longest dimension). The final part dimensions are shown in the model in Figure 5.16.

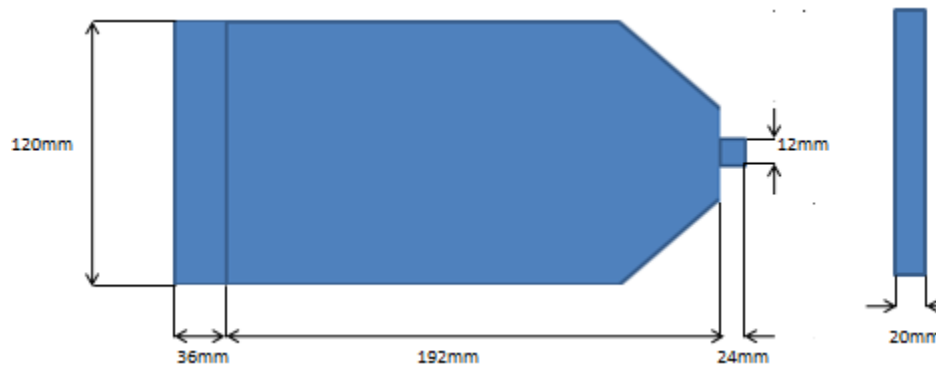


Figure 5.16: Dimensions of the Cantilever beam – SIMP and HOMOGB

### 5.5 FABRICATED PARTS

An 80-20 mix of virgin Nylon 11 and overflow powder was used to fabricate the parts. Three cantilever parts in each design (SIMP and HOMOGB) were fabricated in the

orientation determined before (thin cell walls in the vertical direction with holes in the x-y plane). Two MBB parts in each design (SIMP and HOMOG) were fabricated. A 2.54 mm spacing was left between parts. The parts took up a build height of 305mm or 12 inches in the build chamber. Eight tensile specimens, four in horizontal direction and four in vertical direction, were added, each measuring 165mm in length, 13.5mm in width and 3.4mm in thickness. The tensile specimens serve to experimentally determine the young's modulus of the powder mixture. It took 23 hours to remove the parts and sufficient time was spent additionally in post processing to clean up the loose powder in the parts. The arrangement of the parts in the build chamber is shown in Figure 5.17.

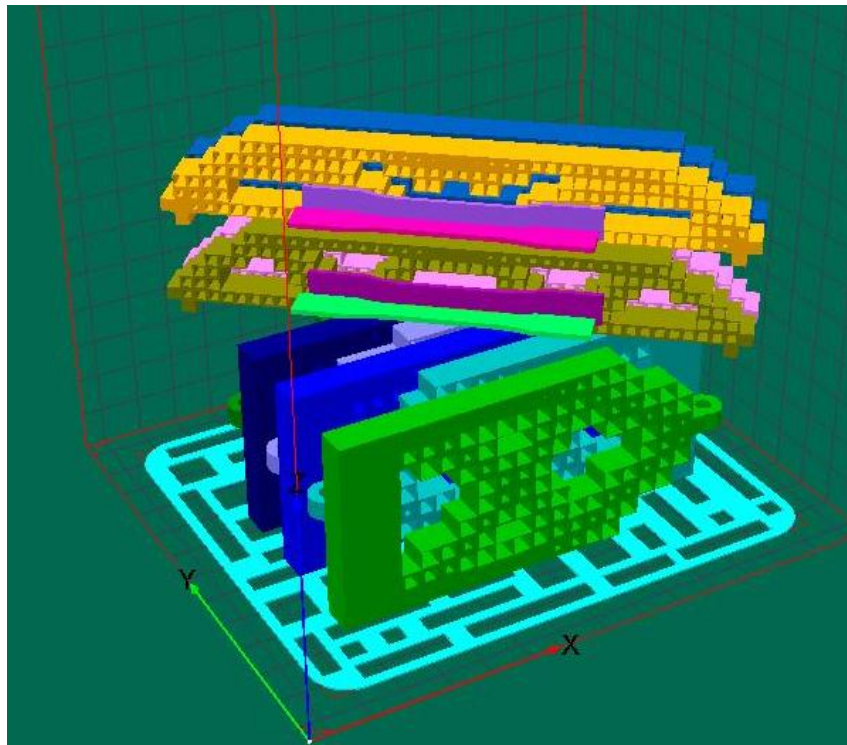


Figure 5.17 Arrangement of parts in the build chamber



The fabrication parameters for the build were the same as before in Table 5.1. In order to eliminate curling of parts the bed temperature was adjusted at 0.036inch height of the build chamber to 187°C and from a height of 0.7 inch height onwards the bed temperature was maintained constant at 186°C. The fabricated parts are shown in Figure 5.18.

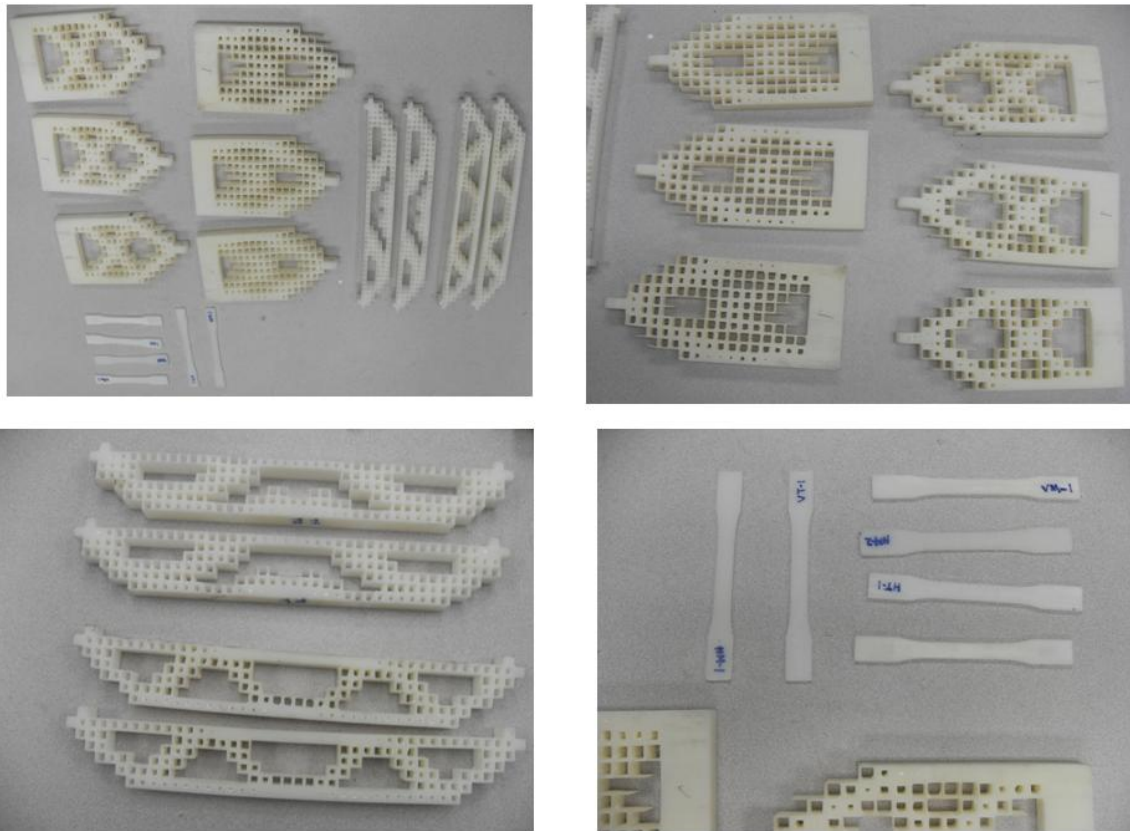


Figure 5.18: Fabricated parts - Cantilever, MBB beams and Tensile specimens

## 5.6 EXPERIMENTAL TESTING RESULTS

The tensile specimens were subjected to tensile testing on the INSTRON testing equipment. An extensometer was used to measure displacement strains. Five tests were conducted on each specimen giving a total of 40 test values. Load was applied at the rate of 3.2mm/minute and each specimen was constrained to a strain limit of 0.07mm/mm. Sufficient time was given between tests to let the sample return to its unstrained condition on the removal of applied load. The results are shown in Figure 5.19 with the respective locations of the specimen inside the build chamber. The orientation schematic is shown in Figure 5.19.

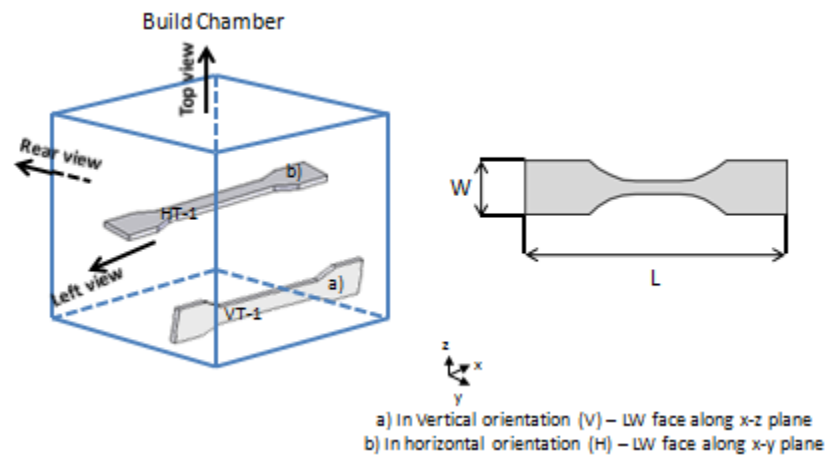


Figure 5.19: Schematic for orientation of tensile specimens inside the build chamber

In Figures 5.19 and 5.20, 'H' refers to horizontal specimen and 'V' denotes a vertical specimen, 'M' denotes a specimen in the middle of the build chamber and 'T' denotes the top of the build chamber. The numbers '1' and '2' indicate the front and the rear sides of the build chamber respectively. For instance, HT-2 means that the specimen was horizontal, closer to the top end of the build chamber and on the rear end of the build chamber. In Figure 5.18, for the purpose of clarity, only parts lying closer to the top and

front side of the build chamber are shown. To enhance visibility, the tensile parts have not been drawn to the scale of the build chamber. The total height of the build chamber is 381mm and the length of the tensile specimen is only 155mm.

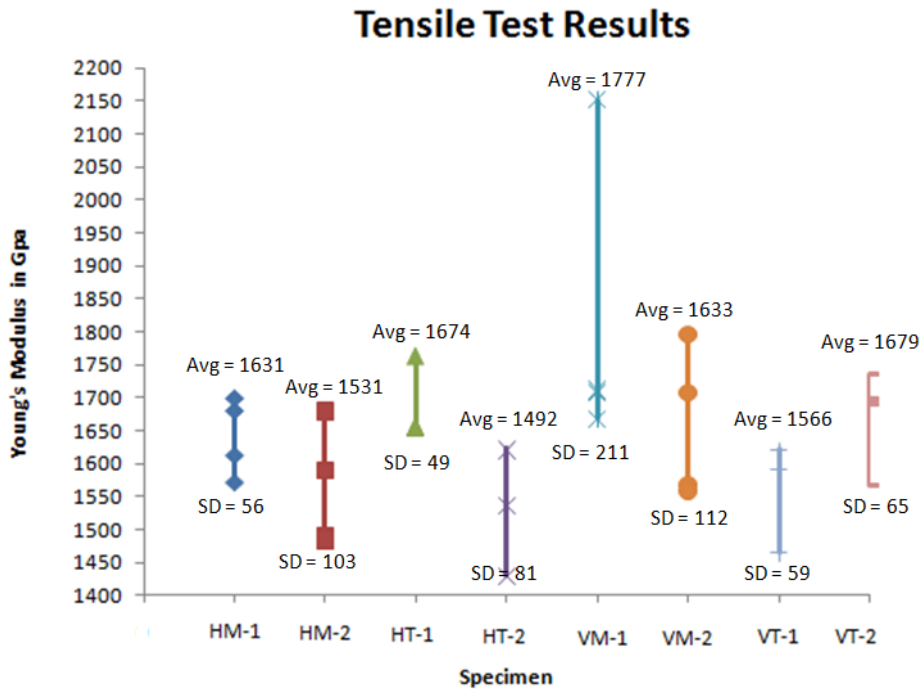


Figure 5.20: Tensile test results giving young's modulus for the specimens

It can be observed that in general vertically oriented components had a higher modulus value than their corresponding horizontal counterparts with the exception of VT-1. Within a particular orientation the parts that were towards the front end (represented by number 1) had a higher modulus value than the rear end counterparts again with the exception of VT-1. If the anomalous data point on VM-1 is omitted, the modulus value of the remaining 39 samples averages to 1600GPa with a standard

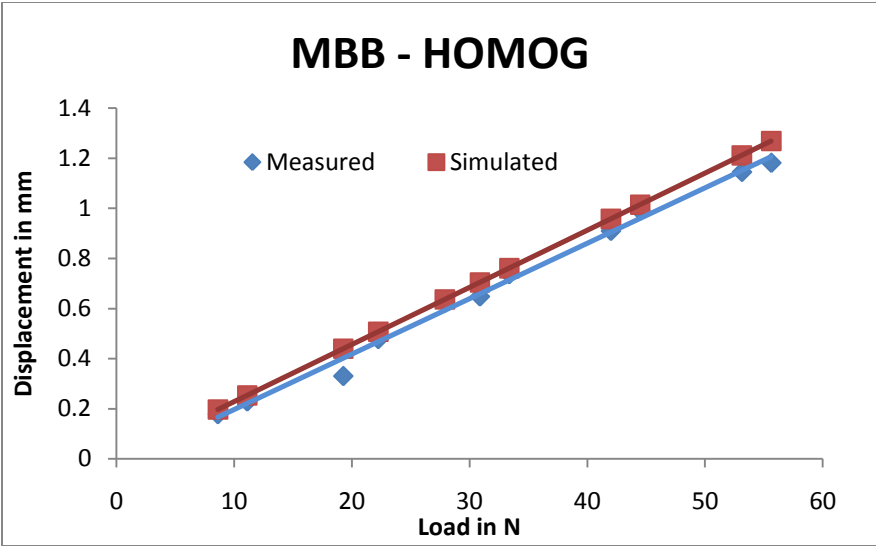
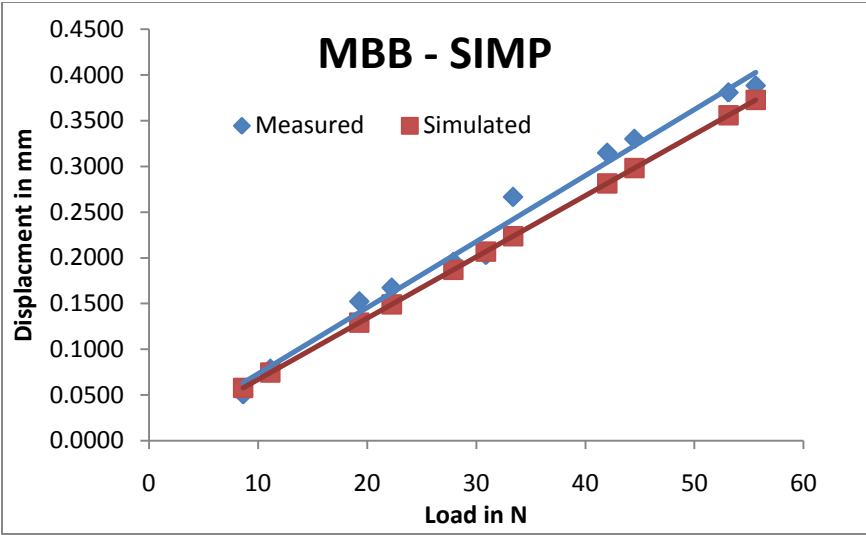
deviation of 100GPa. A value of 1600GPa is chosen as the young's modulus of the 80-20 mixture in all numerical simulations.

Four specimens - two cantilever cases (SIMP and HOMOOG) and two MBB cases (SIMP and HOMOOG) were experimentally evaluated for displacement under applied load. The results are shown in Table 5.3.

Load (lb)	Load (N)	Displacement (mm)			
		MBB		Cantilever	
		SIMP	HOMOOG	SIMP	HOMOOG
1.94	8.63	0.0508	0.1778	0.0254	0.0343
2.50	11.13	0.0787	0.2286	0.0317	0.0508
4.33	19.28	0.1524	0.3302	0.0483	0.0889
5.00	22.25	0.1674	0.4775	0.0610	0.1016
6.27	27.90	0.1956	0.6223	0.0762	0.1524
6.94	30.88	0.2032	0.6477	0.0902	0.1651
7.50	33.38	0.2667	0.7366	0.1010	0.1804
9.44	42.01	0.3150	0.9093	0.1280	0.2413
10.00	44.50	0.3302	0.9904	0.1321	0.2540
11.83	53.13	0.3810	1.1446	0.1512	0.3264
12.50	55.63	0.3886	1.1811	0.1577	0.3493

Table 5.3: Load – Displacement results for experimentally tested parts

The results of maximum displacement from numerical algorithms for the four cases of design solutions were compared with the experimental values. To closely replicate the experimentally tested parts on the numerical tools, hole size deviations against actual size in the CAD model were again measured in these final parts and adjustments for these fabrication errors were incorporated into the design solutions. The results are plotted in Figure 5.21.



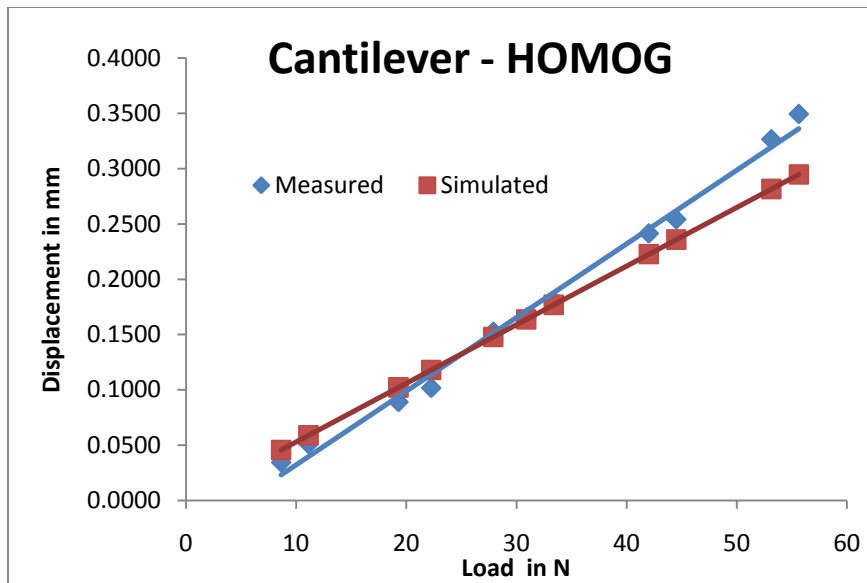
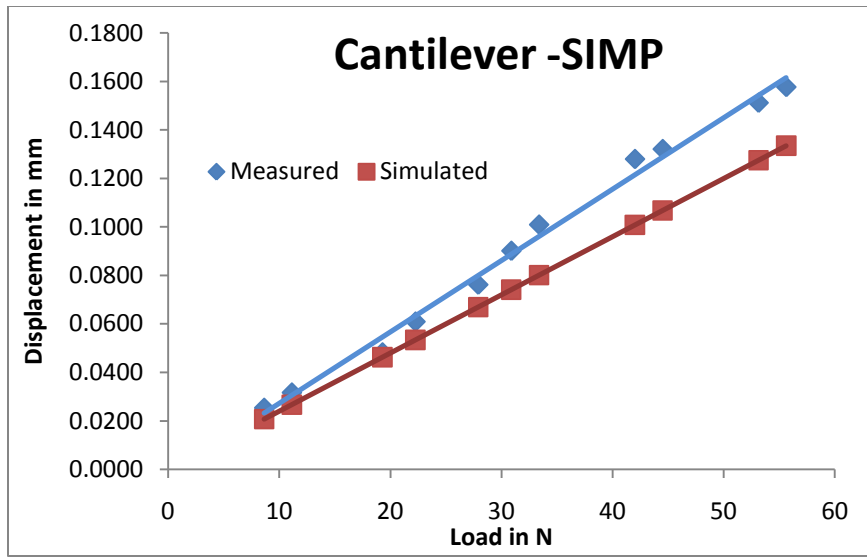


Figure 5.21: Comparison of experimental results with numerical models

It can be observed that in general there is good agreement in the displacement values of the experimental results with the numerical methods based on plane stress approximation. The average error in all the cases is less than 10%. The error plots are shown in Figure 5.22.

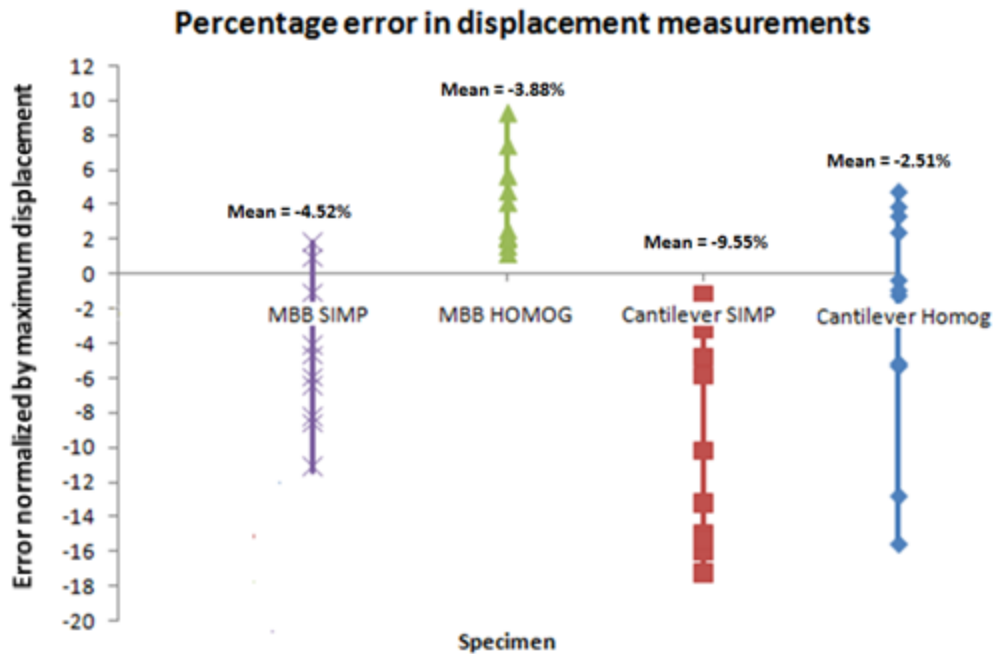


Figure 5.22: Error percentage results for different cases against numerical models

The cantilever case had greater errors in the measured displacement values than the MBB beam case relative to the numerical models. Further, the slope of the displacement vs. load curve was more deviant from the numerical model for the cantilever case than it was for the MBB beam. This can be explained by the fact that deviations from intended hole sizes were more consistent for the MBB parts than for the

cantilever parts, partly due to the symmetry of the MBB beam. Additionally, the MBB beam case included a greater number of cells (240) and the unit cell sizes were smaller (8mm) than the cantilever case. The errors for the SIMP models were greater than those for the HOMOGENEOUS models. This trend can be explained by the fact that the SIMP routine is not very a good approximation of the material mesostructure as it uses a power law model without any reference to the underlying geometry. Homogenization on the other hand is dependent on the material geometry and characterized the underlying mesostructure rigorously based on shape, size and orientation.

## **5.8 SUMMARY**

In this chapter, the necessary steps in the conversion of design solutions to CAD models were outlined. The limits on achievable feature sizes with the SLS technique and the best part orientations for minimizing the achievable feature size limits were explored. Based on this information, the dimensions of the part were determined taking into account the thin walls necessary to represent the low density regions, the fabrication limit on those walls, and the dimensions required to accommodate the testing apparatus. The details of the experimental apparatus were also detailed, including the features for support and loadings.

After the determination of the final dimensions of the parts, fabrication was carried out with the addition of standard tensile specimens into the build chamber. Tensile experiments were conducted to determine the Young's modulus of the 80-20 mix of virgin/overflow Nylon-11 powder used to make the parts. An average value 1600GPa was calculated to be used in numerical models.



Snapshots of the test setup for the three point bending and cantilever experiments were provided and a comparison of the results from the experimental study with the numerical models was provided for all the beam cases. A very good agreement (overall deviation percentage of less than 10%) was observed between the experimental measurements and numerically simulated values.

## **Chapter 6: Conclusions and Directions for Future Work**

In this chapter, a summary of the unique contributions and their usefulness for the present and future work are presented. The strengths and limitations of the proposed design method for custom mesostructure components are discussed. Suggestions for addressing these limitations and avenues for future research are provided.

### **6.1 SUMMARY OF CONTRIBUTIONS**

A design tool that can cater to the unique capabilities of additive manufacturing was motivated in this work. Accordingly, a homogenization based design tool (HOMOG-B) for mesostructure tailored designs was developed using techniques described in the literature. A homogenization based analysis procedure was implemented for analyzing the elastic structural properties of customized mesostructures. The mesostructures were smoothed and design variable reduction was achieved through B-spline surface parameterization for the two dimensional design domain. The design tool was applied to two common topology optimization problems – the MBB beam and the cantilever beam – and the resulting designs were fabricated using the selective laser sintering technique. Experimental testing was performed, and the design tool predictions were confirmed. Additive manufacturing process variables such as part orientation for minimization of dimensional errors were also studied in this work. Experimental results agreed very closely with the predictions of numerical models and helped validate the design methodology introduced in this work. The quality of solutions obtained from the HOMOG-B algorithm were compared with SIMP solutions for structural performance parameters strain energy and maximum displacement. The SIMP solutions were stiffer

than the HOMOGENEOUS-B solutions. This result was expected because it had been shown previously in literature that SIMP solutions matched analytical results at low volume fractions for stiffness optimization. However, the SIMP algorithm does not support mesostructure tailored designs because penalization parameters typically enforce convergence to macrostructures with fully dense regions and the structural performance of intermediate densities cannot be accurately analyzed with the SIMP technique. Although not demonstrated in this work, the mesostructure tailored designs obtained by the HOMOGENEOUS-B algorithm may have several superior properties other than stiffness. For example, they may exhibit superior buckling strength, relative to non-mesostructured SIMP solutions of equivalent mass, due to distribution of material over a broader region and the large number of short cell walls available to distribute structural loads. The energy absorption and convective heat transfer of designed mesostructures could be advantageous, as well.

Overall the design tool was successful in enabling mesostructure tailored designs that are manufacturable solely through additive manufacturing methods. Towards this goal, this design tool has captured most of the current needs and serves as a framework that can be built upon with the ability to handle diverse mesostructure architectures in the future. A more detailed insight into the contributions of this work is presented next.

The biggest strength of the homogenization method is its capability to accurately estimate material properties of a macrostructure when it is composed of heterogeneous structures in the meso scale. However, the homogenization based design tool can only be used when the design variable values in the design domain are characterized by a smoothly varying locally periodic function. Therefore, there was a need to develop a smoothing mechanism to ensure satisfaction of this constraint. A challenge posed by the homogenization method is the large number of design variables it introduces for the

material optimization problem, requiring three variables shape, size and orientation for each mesostructure unit cell. Thus, as the number of unit cells within the structure increases the number of design variables increases three times as fast as the SIMP method. There is a definite need to explore design variable reduction methods and integrate them with the optimization routine.

The first important contribution of this work is the novel parametric smoothing scheme with B-spline surfaces for use with the homogenization routine to enforce local periodicity of design variables in the design domain. A surface parameterization of the design domain using cubic b-spline surface patches allows the density values of mesostructure units to be computed as the height of the surface at the centroid of these unit meso cells. Since a surface patch defined by the b-spline can be manipulated to possess a very high degree of continuity, the satisfaction of the homogenization assumption is automatically enforced.

A second advantage of a B-spline smoothing scheme lies in its ability to simultaneously offer a solution for the challenge of coping with large numbers of design variables during the optimization process. Since a b-spline surface is controlled by its control point locations, fewer control points than the actual number of design variables can be used as the field variables to drive the optimization routine. Thus, design variable reduction using the B-spline smoothing scheme is a second important contribution of this work.

The drawback of this method is that gradient computations are expensive with the B-spline scheme because each control point influences several surrounding mesostructure unit cells, which in turn influence the objective and constraint functions. Therefore, the B-spline smoothing scheme places a limit on the number of unit cells in the macrostructure if the optimization is led by gradient based algorithms. A non-gradient

based method would not require the computation of derivatives and would be one possible solution to this problem, although those approaches have heavy computational loads from their own algorithms. Again, in this work the number of unit cells and their minimum positive and negative feature sizes are constrained by the limits of the selective laser sintering fabrication method. Therefore, even if the surface parameterized homogenization method could computationally allow large number of small meso-cells, the solutions will be beyond manufacturable feasibility. Thus, the impact of this drawback is weakened by the fabrication limitations.

Though homogenization has been discussed extensively for mesostructure characterization, little focus has been devoted to studying the characteristics of actual parts that can be fabricated through additive manufacturing techniques. There is little reference in the literature to acceptable tolerances on CAD models of mesostructure designs and whether parts can be fabricated to within this tolerance in actual fabrication. The impact of these fabrication deviations needs to be very thoroughly understood to ensure that the numerical models for mesostructure tailored designs serve as a good approximation to actual part behaviors in practice. Thus, there is a need to experimentally validate the numerical model results for engineering problems.

Accordingly, a third important contribution of this work is the experimental validation of the developed design tool for mesostructure tailored designs. Design solutions from the homogenization based optimization with surface parameterization were fabricated using the selective laser sintering technique and experimentally tested using specially designed test fixtures. The observed maximum displacement values for the cantilever and three point bending problems were compared with numerical model displacement values and an overall deviation of less than 10% for displacements of the order of 1/10ths of a millimeter were obtained. Additionally, the widely publicized SIMP

solutions and their numerical models from Sigmund [44] were fabricated, tested and added to the comparison charts to validate testing procedures and determine the quality of the homogenization based solutions.

## **6.2 UNRESOLVED ISSUES ASSOCIATED WITH THE CURRENT WORK**

The sensitivity of the B-spline based design variable reduction on the quality of the final design solution is an unknown in this work and as a result there is no reference on how much reduction is ideal so that solution quality is not lost in the pursuit of decreasing computational load. An arbitrary reduction of 50% was chosen in this work i.e., the number of control points used to adjust the surface shape was exactly half the number of mesostructure unit cells (the number of holes) in the design domain. An ideal starting point to solve this issue would be to consider a small number of unit cells and solve the standard cantilever and three point bending problems without the surface parameterization scheme integration into the optimization routine. A second technique to achieve the same result is to allow the number of control points to be equal to the number of design variables initially and slowly decrease them to study their effect on the final solutions and deduce an acceptable reduction ratio.

A second unresolved issue with the current work is that the homogenization solutions are starting point dependent. Choosing a good starting point affects the computational time and the solution quality to some extent. Since this behavior was observed after the surface parameterization scheme was integrated, it implies that the design variable reduction can contribute to increased instances of local minima in the search space – an unwanted consequence for the optimization problem. A possible

solution to this issue would be to use multi-start gradient based algorithms or a GA approach to identify good starting points for a gradient based algorithm.

### **6.3 AVENUES FOR FUTURE WORK**

There are two directions that research can take from the conclusions of this work. A square mesostructure was studied in this work. Study of other regular shapes like hexagon, triangle, rectangle and kagome would be a very useful extension to this work. A library of such unit cells in material design would constitute a structure that is truly in the spirit of additive manufacturing and has the capability to spur the development of a wealth of design tools that can promise a solution with varied structural characteristics. It would also be interesting to transition from one type of unit cell to another (e.g., from triangular to rectangular).

The performance of fabricated parts was measured in the elastic region, but the failure limit of these structures was not investigated. Since the homogenized solutions include distributed cell voids and walls, it is highly possible that their failure limits are much better than the solid-void solutions. Buckling strength, for example, is likely to be higher for a thick mesostructured beam than a thin monolithic (solid-void beam). Thus, the performance criterion could be expanded to reflect some of the strengths of the mesostructure substituted designs and can be measured for comparison.

## Appendix A

### Plane Strain – Data Points for Homogenization( $\rho_h, E_1^H, \nu^H, G_{12}^H$ )

$\rho_h$	$\delta_1$	$\delta_2$	$E_1^H$	$\nu^H$	$\delta_3$	$G_{12}^H$
0.04	4.60E-07	-4.42E-09	2.17E+04	0.0096	1.14E-03	8.77E+00
0.08	2.26E-07	-4.50E-09	4.42E+04	0.0199	2.77E-04	3.62E+01
0.13	1.50E-07	-4.48E-09	6.65E+04	0.0298	7.99E-05	1.25E+02
0.15	1.12E-07	-4.47E-09	8.90E+04	0.0398	3.31E-05	3.02E+02
0.19	8.97E-08	-4.46E-09	1.12E+05	0.0498	1.66E-05	6.02E+02
0.23	7.45E-08	-4.46E-09	1.34E+05	0.0599	9.41E-06	1.06E+03
0.26	6.37E-08	-4.46E-09	1.57E+05	0.0700	5.81E-06	1.72E+03
0.29	5.56E-08	-4.45E-09	1.80E+05	0.0802	3.81E-06	2.62E+03
0.33	4.92E-08	-4.45E-09	2.03E+05	0.0904	2.62E-06	3.82E+03
0.36	4.42E-08	-4.45E-09	2.26E+05	0.1007	1.87E-06	5.35E+03
0.39	4.01E-08	-4.45E-09	2.50E+05	0.1111	1.37E-06	7.28E+03
0.42	3.66E-08	-4.48E-09	2.73E+05	0.1224	1.04E-06	9.65E+03
0.45	3.37E-08	-4.47E-09	2.97E+05	0.1327	7.97E-07	1.25E+04
0.48	3.12E-08	-4.45E-09	3.21E+05	0.1425	6.25E-07	1.60E+04
0.51	2.90E-08	-4.45E-09	3.44E+05	0.1531	4.97E-07	2.01E+04
0.54	2.71E-08	-4.45E-09	3.69E+05	0.1638	4.01E-07	2.49E+04
0.56	2.55E-08	-4.44E-09	3.93E+05	0.1745	3.27E-07	3.05E+04
0.59	2.40E-08	-4.44E-09	4.17E+05	0.1854	2.71E-07	3.69E+04
0.62	2.26E-08	-4.44E-09	4.42E+05	0.1962	2.26E-07	4.42E+04
0.64	2.15E-08	-4.44E-09	4.66E+05	0.2072	1.91E-07	5.24E+04
0.66	2.04E-08	-4.44E-09	4.91E+05	0.2180	1.63E-07	6.15E+04
0.69	1.94E-08	-4.45E-09	5.16E+05	0.2294	1.40E-07	7.16E+04
0.71	1.85E-08	-4.45E-09	5.41E+05	0.2406	1.21E-07	8.27E+04
0.73	1.76E-08	-4.44E-09	5.67E+05	0.2519	1.06E-07	9.47E+04
0.75	1.69E-08	-4.44E-09	5.92E+05	0.2632	9.29E-08	1.08E+05
0.77	1.62E-08	-4.44E-09	6.17E+05	0.2743	8.16E-08	1.23E+05
0.79	1.55E-08	-4.45E-09	6.46E+05	0.2873	7.30E-08	1.37E+05
0.81	1.49E-08	-4.44E-09	6.72E+05	0.2983	6.57E-08	1.52E+05
0.82	1.43E-08	-4.43E-09	6.99E+05	0.3093	5.96E-08	1.68E+05
0.84	1.38E-08	-4.40E-09	7.24E+05	0.3186	5.47E-08	1.83E+05
0.86	1.33E-08	-4.39E-09	7.52E+05	0.3303	5.00E-08	2.00E+05
0.87	1.28E-08	-4.37E-09	7.79E+05	0.3404	4.63E-08	2.16E+05
0.88	1.24E-08	-4.34E-09	8.06E+05	0.3496	4.31E-08	2.32E+05
0.90	1.20E-08	-4.32E-09	8.32E+05	0.3592	4.03E-08	2.48E+05
0.91	1.17E-08	-4.28E-09	8.57E+05	0.3665	3.80E-08	2.63E+05
0.92	1.13E-08	-4.25E-09	8.84E+05	0.3757	3.60E-08	2.78E+05
0.93	1.10E-08	-4.22E-09	9.09E+05	0.3836	3.42E-08	2.92E+05
0.94	1.07E-08	-4.19E-09	9.35E+05	0.3916	3.24E-08	3.09E+05



$\rho_h$	$\delta_1$	$\delta_2$	$E_1^H$	$\nu^H$	$\delta_3$	$G_{12}^H$
0.95	1.04E-08	-4.15E-09	9.62E+05	0.3990	3.15E-08	3.17E+05
0.96	1.02E-08	-4.11E-09	9.78E+05	0.4016	3.03E-08	3.30E+05
0.97	1.00E-08	-4.08E-09	1.00E+06	0.4078	2.94E-08	3.40E+05
0.97	1.00E-08	-4.08E-09	1.00E+06	0.4078	2.94E-08	3.40E+05
0.98	9.64E-09	-4.01E-09	1.04E+06	0.4162	2.80E-08	3.58E+05
1.00	9.10E-09	-3.90E-09	1.10E+06	0.4286	2.60E-08	3.85E+05

**Plane Stress – Data Points for Homogenized material model ( $\rho_h, E_1^H, \nu^H, G_{12}^H$ )**

$\rho_h$	$\delta_1$	$\delta_2$	$E_1^H$	$\nu^H$
0.04	4.98E-07	-3.70E-09	2.01E+04	0.007
0.08	2.48E-07	-3.68E-09	4.03E+04	0.015
0.13	1.65E-07	-3.66E-09	6.05E+04	0.022
0.15	1.24E-07	-3.64E-09	8.09E+04	0.029
0.19	9.86E-08	-3.63E-09	1.01E+05	0.037
0.23	8.19E-08	-3.62E-09	1.22E+05	0.044
0.26	7.00E-08	-3.62E-09	1.43E+05	0.052
0.29	6.11E-08	-3.62E-09	1.64E+05	0.059
0.33	5.42E-08	-3.61E-09	1.85E+05	0.067
0.36	4.86E-08	-3.61E-09	2.06E+05	0.074
0.39	4.41E-08	-3.61E-09	2.27E+05	0.082
0.42	4.03E-08	-3.61E-09	2.48E+05	0.090
0.45	3.71E-08	-3.61E-09	2.70E+05	0.097
0.48	3.43E-08	-3.61E-09	2.91E+05	0.105
0.51	3.20E-08	-3.60E-09	3.13E+05	0.113
0.54	2.99E-08	-3.60E-09	3.35E+05	0.121
0.56	2.81E-08	-3.60E-09	3.56E+05	0.128
0.59	2.64E-08	-3.60E-09	3.78E+05	0.136
0.62	2.50E-08	-3.60E-09	4.00E+05	0.144
0.64	2.37E-08	-3.60E-09	4.22E+05	0.152
0.66	2.25E-08	-3.61E-09	4.45E+05	0.161
0.69	2.14E-08	-3.60E-09	4.67E+05	0.168
0.71	2.04E-08	-3.60E-09	4.90E+05	0.177
0.73	1.95E-08	-3.60E-09	5.14E+05	0.185
0.75	1.86E-08	-3.60E-09	5.38E+05	0.194
0.77	1.78E-08	-3.60E-09	5.63E+05	0.203
0.79	1.70E-08	-3.61E-09	5.88E+05	0.213

$\rho_h$	$\delta_1$	$\delta_2$	$E_1^H$	$\nu^H$
0.81	1.63E-08	-3.60E-09	6.12E+05	0.220
0.82	1.57E-08	-3.59E-09	6.36E+05	0.228
0.84	1.52E-08	-3.55E-09	6.59E+05	0.234
0.86	1.46E-08	-3.55E-09	6.85E+05	0.243
0.87	1.41E-08	-3.52E-09	7.10E+05	0.250
0.88	1.36E-08	-3.49E-09	7.34E+05	0.256
0.90	1.32E-08	-3.46E-09	7.58E+05	0.262
0.91	1.28E-08	-3.41E-09	7.80E+05	0.266
0.92	1.24E-08	-3.39E-09	8.05E+05	0.273
0.93	1.21E-08	-3.35E-09	8.28E+05	0.277
0.94	1.18E-08	-3.30E-09	8.47E+05	0.280
0.95	1.15E-08	-3.27E-09	8.70E+05	0.284
0.96	1.12E-08	-3.23E-09	8.90E+05	0.287
0.97	1.10E-08	-3.19E-09	9.11E+05	0.291
0.98	1.06E-08	-3.12E-09	9.45E+05	0.295
1.00	1.00E-08	-3.00E-09	1.00E+06	0.300

Since there was not any significant difference in the computed  $G_{12}^H$  values of the plane strain model from the computed  $G_{12}^H$  values of the plane stress model, the plane stress  $G_{12}^H$  values were used for plane strain approximation cases.

## Appendix B

### Matlab Code for Homogenization Analysis

```
function
[StrainEnergyScaled, StrainEnergyDeriv]=TrialCSThmg4_2beamFLTR_DV(volvec
tor, GridSize, NoCells, PLoad)
%tic
%
% -----
SqBdry=[5 5; 5+GridSize(1) 5+GridSize(2)];
ElemSize = GridSize(1)/NoCells(1);
r=volvector;
a=10;
NoXPts = (SqBdry(2,1)- SqBdry(1,1))/ElemSize; %1 Element
NoYPts = (SqBdry(2,2)- SqBdry(1,2))/ElemSize; % 1 Element

% GENERATING NODES AND ASSIGNING NODE NUMBERS TO NODAL COORDINATES
% -----
ct = 1;
for i = 1: (NoXPts + 1)
    NodalXCoord(i) = SqBdry(1,1) + (i-1)*ElemSize;
    for j= 1:(NoYPts + 1)
        NodalYCoord(i,j) =SqBdry(1,2) + (j-1)*ElemSize;
        NodeNumber(ct,1:2) = [NodalXCoord(i) NodalYCoord(i,j)];
        ct = ct + 1;
    end
end
TotalNoNodes = ct-1;

% GENERATING ELEMENTS FROM NODES
% -----
ct = 1;
EStN = 0;
for i=1:NoXPts
    for j=1:NoYPts
        Element(ct,1:4) = [EStN+j EStN+j+1 NoYPts+1+EStN+j
NoYPts+1+EStN+j+1];
        ct= ct + 1;
    end
    EStN = EStN + NoYPts+1;
    Topnodes(i)= EStN;
end
%Topnodes
NoElements = ct-1;
```

```

% GENERATING STIFFNESS MATRIX FOR THE HOMOGENIZED ELEMENT
% -----

RD=[0.041 0.083 0.128 0.154 0.19 0.226 0.26 0.294 0.328...
    0.36 0.391 0.422 0.452 0.4820 0.51 0.538 0.564 0.59 ...
    0.616 0.64 0.664 0.686 0.708 0.73 0.75 0.7696 0.7884 ...
    0.8064 0.8236 0.84 0.8556 0.8704 0.8844 0.8976 0.91 ...
    0.9216 0.9324 0.9424 0.9516 0.96 0.9676 0.9804 1.0];

% PLANE STRAIN
% -----
% E= 15*[2.17 4.42 6.65 8.9 11.2 13.4 15.7 18 20.3 22.6 25 ...
%         27.3 29.7 32.1 34.4 36.9 39.3 41.7 44.2 46.6 49.1 ...
%         51.6 54.1 56.7 59.2 61.7 64.6 67.2 69.9 72.4 75.2 ...
%         77.9 80.6 83.2 85.7 99.4 90.9 93.5 96.2 97.8 100 106 110];
%
G=1600*power(10,-6)*[8.77 36.2 125 302 602 1060 1720 2620 3820 5350
7280 ...
    9650 12500 16000 20100 24900 30500 36900 44200 52400 ...
    61500 71600 82700 94700 108000 123000 137000 152000 ...
    168000 183000 200000 216000 232000 248000 263000 278000 ...
    292000 309000 317000 330000 340000 358000 385000];
%
% nu12=power(10,-3)*[9.6 19.9 29.8 39.8 49.8 60 70 80.2 90.4 101 ...
%                    111 122 133 143 153 164 175 185 196 207 218 ...
%                    229 241 252 263 274 287 298 309 319 330 340 ...
%                    350 359 367 376 384 392 399 402 408 414 422];
% -----

% PLANE STRESS
% -----
E = 16*[2.01 4.03 6.05 8.09 10.1 12.2 14.3 16.4 18.5...
    20.6 22.7 24.8 27 29.1 31.3 33.5 35.6 37.8 40.0 42.2 44.5...
    46.7 49.0 51.4 53.8 56.3 58.8 61.2 63.6 65.9 68.5 71.0 73.4...
    75.8 78.0 80.5 82.8 84.7 87.0 89.0 91.1 94.5 100 ];

nu12 =power(10,-3)*[7.43 14.8 22.1 29.5 36.8 44.2 51.7 59.2 66.7...
    74.3 81.9 89.5 97.2 105 113 121 128 136 144 152 161 168 177 ...
    185 194 203 213 220 228 234 243 250 256 262 266 273 277 280 ...
    284 287 291 295 300];
% -----

GlobalStfns = zeros(TotalNoNodes*2);

% COMPUTING THE GLOBAL STIFFNESS MATRIX
% -----
---
```

```

for i = 1:NoElements
```

```

    Ehomog =spline(RD,E,r(i));
    Ghomog =spline(RD,G,r(i));
    nu12hmg =spline(RD,nu12,r(i));
```

```

% PLANE STRAIN CONSTITUTIVE COEFFICIENTS
%-----
% C11 = Ehomog*(1-nu12hmg)/(1-nu12hmg - 2*nu12hmg*nu12hmg);
% C22 = Ehomog*(1-nu12hmg*nu12hmg)/[(1+nu12hmg)*(1-nu12hmg-
2*nu12hmg*nu12hmg)];
% C12 = nu12hmg*Ehomog/(1-nu12hmg - 2*nu12hmg*nu12hmg);

%PLANE STRESS CONSTITUTIVE COEFFICIENTS
%-----
C11 = Ehomog/(1-power(nu12hmg,2));
C12 = nu12hmg*C11;
C22 = C11;
C33 = Ghomog;
%C33 = Ehomog/(2*(1+nu12hmg));
C21 = C12;

b=a;
h=22; % Unit Cell thickness
K11 = h*(C11*b/(3*a) + C33*a/(3*b));
K12 = h*(C12/4 + C33/4);
K13 = h*(C11*b/(6*a) - C33*a/(3*b));
K14 = h*(-C12/4 + C33/4);
K15 = h*(-C11*b/(3*a) + C33*a/(6*b));
K16 = h*(C12/4 - C33/4);
K17 = h*(-C11*b/(6*a) - C33*a/(6*b));
K18 = h*(-C12/4 - C33/4);
K22 = h*(C22*a/(3*b) + C33*b/(3*a));
K23 = h*(C12/4 - C33/4);
K24 = h*(-C22*a/(3*b) + C33*b/(6*a));
K25 = h*(-C21/4 + C33/4);
K26 = h*(C22*a/(6*b) - C33*b/(3*a));
K27 = h*(-C21/4 - C33/4);
K28 = h*(-C22*a/(6*b) - C33*b/(6*a));
K33 = h*(C11*b/(3*a) + C33*a/(3*b));
K34 = h*(-C12/4 - C33/4);
K35 = h*(-C11*b/(6*a) - C33*a/(6*b));
K36 = h*(C12/4 + C33/4);
K37 = h*(-C11*b/(3*a) + C33*a/(6*b));
K38 = h*(-C12/4 + C33/4);
K44 = h*(C22*a/(3*b) + C33*b/(3*a));
K45 = h*(C21/4 + C33/4);
K46 = h*(-C22*a/(6*b) - C33*b/(6*a));
K47 = h*(C21/4 - C33/4);
K48 = h*(C22*a/(6*b) - C33*b/(3*a));
K55 = h*(C11*b/(3*a) + C33*a/(3*b));
K56 = h*(-C12/4 - C33/4);
K57 = h*(C11*b/(6*a) - C33*a/(3*b));
K58 = h*(C12/4 - C33/4);
K66 = h*(C22*a/(3*b) + C33*b/(3*a));
K67 = h*(-C21/4 + C33/4);
K68 = h*(-C22*a/(3*b) + C33*b/(6*a));
K77 = h*(C11*b/(3*a) + C33*a/(3*b));

```

```

K78 = h*(C12/4 + C33/4);
K88 = h*(C22*a/(3*b) + C33*b/(3*a));

KElStfns = [ K11 K12 K13 K14 K15 K16 K17 K18
             K12 K22 K23 K24 K25 K26 K27 K28
             K13 K23 K33 K34 K35 K36 K37 K38
             K14 K24 K34 K44 K45 K46 K47 K48
             K15 K25 K35 K45 K55 K56 K57 K58
             K16 K26 K36 K46 K56 K66 K67 K68
             K17 K27 K37 K47 K57 K67 K77 K78
             K18 K28 K38 K48 K58 K68 K78 K88];

ElementNodes(1:4) = Element(i,1:4);

for j = 1:4

    GlobalStfns((ElementNodes(j)*2-
1):(ElementNodes(j)*2), (ElementNodes(j)*2-1):(ElementNodes(j)*2)) =
GlobalStfns((ElementNodes(j)*2-
1):(ElementNodes(j)*2), (ElementNodes(j)*2-1):(ElementNodes(j)*2)) +
KElStfns((j*2-1):(j*2), (j*2-1):(j*2));
        for k=1:4
            if (j+k)>4
                break;
            end
            GlobalStfns((ElementNodes(j)*2-
1):(ElementNodes(j)*2), (ElementNodes(j+k)*2-1):(ElementNodes(j+k)*2)) =
GlobalStfns((ElementNodes(j)*2-
1):(ElementNodes(j)*2), (ElementNodes(j+k)*2-1):(ElementNodes(j+k)*2)) +
KElStfns((j*2-1):(j*2), ((j+k)*2-1):((j+k)*2));
            GlobalStfns((ElementNodes(j+k)*2-
1):(ElementNodes(j+k)*2), (ElementNodes(j)*2-1):(ElementNodes(j)*2)) =
GlobalStfns(((ElementNodes(j+k)*2-
1):((ElementNodes(j+k)*2), (ElementNodes(j)*2-1):(ElementNodes(j)*2)) +
KElStfns(((j+k)*2-1):((j+k)*2), (j*2-1):(j*2));

        end
    end
end

% FORMULATING THE FINITE ELEMENT PROBLEM WITH FORCES AND BOUNDARY
% CONDITIONS
% -----
% -----

% Applying Forces
% -----
ForceVector(2*(NoXPts+1)*(NoYPts+1)) = -0.5;%CellLoad/2;
ForceVector= ForceVector';

```

```

% Constraining Degrees of Freedom
% -----

alldofs = 1:2*TotalNoNodes;
fixedxdofs = [2*(NoXPts*(NoYPts+1))+1:2:2*(NoXPts+1)*(NoYPts+1)];
fixeddofs = [2
fixedxdofs];%2*NoXPts*(NoYPts+1)+1,2*NoXPts*(NoYPts+1)+2];
freedofs = setdiff(alldofs,fixeddofs);
FullDisplV(freedofs,:) =
GlobalStfns(freedofs,freedofs)\ForceVector(freedofs,1);
FullDisplV(fixeddofs,:) =0;

for i = 1:TotalNoNodes
    SolV(i,1) = i*power(10,-7);
    SolV(i,2) = FullDisplV(2*i-1);
    SolV(i,3) = FullDisplV(2*i);

end
subplot(2,1,2);colormap(gray); imagesc(-XYD_OLD);
axis equal; axis tight; axis off;pause(1e-6);

RD_Interval = [0.041 0.154;0.19 0.294;0.328 0.422;0.452 0.538;...
0.564 0.640;0.664 0.730;0.750 0.806;0.824 0.870;...
0.884 0.922;0.932 0.960;0.968 1.000];

RD_Boundary = [0.154 0.190;0.294 0.328;0.422 0.452;0.538 0.564;...
0.640 0.664;0.730 0.750;0.806 0.824;0.870 0.884;...
0.922 0.932;0.960 0.968];

function [Prop_der] = deriv(RD,P,elemr,interval)
    Prop_der = 0;
    for d_ctr = 1:2
        if(interval(d_ctr) == -1)
            Lagr = [0 0 0];
        elseif(interval(d_ctr)<11)
            dens_der = [RD(1,(interval(d_ctr)-
1)*4+1);RD(1,(interval(d_ctr)-1)*4+2);...
RD(1,(interval(d_ctr)-
1)*4+3);RD(1,(interval(d_ctr)-1)*4+4)];
            Prop = [P(1,(interval(d_ctr)-
1)*4+1);P(1,(interval(d_ctr)-1)*4+2);...
P(1,(interval(d_ctr)-
1)*4+3);P(1,(interval(d_ctr)-1)*4+4)];
            bas_1 = [3 -2*(dens_der(2)+dens_der(3)+dens_der(4)) ...
dens_der(2)*dens_der(3)+dens_der(3)*dens_der(4)+...
dens_der(4)*dens_der(2)];
            bas_1cons = (dens_der(1)-dens_der(2))*(dens_der(1)-
dens_der(3))*...
(dens_der(1)-dens_der(4));
            bas_2 = [3 -2*(dens_der(1)+dens_der(3)+dens_der(4)) ...

```

```

dens_der(1)*dens_der(3)+dens_der(3)*dens_der(4)+...
    dens_der(4)*dens_der(1)];
    bas_2cons = (dens_der(2)-dens_der(1))*(dens_der(2)-
dens_der(3))*...
    (dens_der(2)-dens_der(4));
    bas_3 = [3 -2*(dens_der(1)+dens_der(2)+dens_der(4))...

dens_der(1)*dens_der(2)+dens_der(2)*dens_der(4)+...
    dens_der(4)*dens_der(1)];
    bas_3cons = (dens_der(3)-dens_der(1))*(dens_der(3)-
dens_der(2))*...
    (dens_der(3)-dens_der(4));
    bas_4 = [3 -2*(dens_der(1)+dens_der(2)+dens_der(3))...

dens_der(1)*dens_der(2)+dens_der(2)*dens_der(3)+...
    dens_der(3)*dens_der(1)];
    bas_4cons = (dens_der(4)-dens_der(1))*(dens_der(4)-
dens_der(2))*...
    (dens_der(4)-dens_der(3));
    Lagr = ...
    (Prop(1)/bas_1cons)*bas_1 + (Prop(2)/bas_2cons)*bas_2
+ ...
    (Prop(3)/bas_3cons)*bas_3 + (Prop(4)/bas_4cons)*bas_4;
else
    dens_der = [RD(1, (interval(d_ctr)-
1)*4+1);RD(1, (interval(d_ctr)-1)*4+2);...
    RD(1, (interval(d_ctr)-1)*4+3)];
    Prop = [P(1, (interval(d_ctr)-
1)*4+1);P(1, (interval(d_ctr)-1)*4+2);...
    P(1, (interval(d_ctr)-1)*4+3)];
    bas_1 = [2 (-dens_der(2)-dens_der(3))];
    bas_1cons = (dens_der(1)-dens_der(2))*(dens_der(1)-
dens_der(3));
    bas_2 = [2 (-dens_der(1)-dens_der(3))];
    bas_2cons = (dens_der(2)-dens_der(1))*(dens_der(2)-
dens_der(3));
    bas_3 = [2 (-dens_der(1)-dens_der(2))];
    bas_3cons = (dens_der(3)-dens_der(2))*(dens_der(3)-
dens_der(1));
    Lagr = ...
    (Prop(1)/bas_1cons)*bas_1 + (Prop(2)/bas_2cons)*bas_2
+ ...
    (Prop(3)/bas_3cons)*bas_3;
end
if(numel(Lagr) ==2)
    Prop_der1 = Prop_der1+Lagr*[elemr;1];
else
    Prop_der1 = Prop_der1+Lagr*[elemr*elemr;elemr;1];
end
end
if(interval(2)~= -1)
    Prop_der1 = Prop_der1/2;

```



```

        end
end

% COMPUTING STRAIN ENERGY DERIVATIVE
% -----
for i= 1:NoElements

Ehomog =spline(RD,E,r(i));
nu12hmg =spline(RD,nu12,r(i));

% LOCATING THE DENS INTERVAL (POLYNOMIAL PIECE) FOR DERIVATIVE
COMPUTATION
% -----
---
for inter_no = 1:11

    if(r(i)<RD_Interval(1,1))
        Interval(1,1) = 1;
        Interval(2,1) = -1;
        break;
    elseif(r(i) >= 1.0000)
        Interval(1,1) = 11;
        Interval(2,1) = -1;
        break;
    elseif(r(i)>=RD_Interval(inter_no,1)&&
r(i)<=RD_Interval(inter_no,2))
        Interval(1,1) = inter_no;
        Interval(2,1) = -1;
        break;
    elseif(r(i)>RD_Boundary(inter_no,1)&& r(i)<RD_Boundary(inter_no,2))
        Interval(1,1) = inter_no;
        Interval(2,1) = inter_no+1;
        break;
    end
end

end
E_deriv = deriv(RD,E,r(i),Interval);
nu12_deriv = deriv(RD,nu12,r(i),Interval);
G_deriv = deriv(RD,G,r(i),Interval);

%PLANE STRESS CONSTITUTIVE COEFFICIENTS
% -----
% C11 = Ehomog/(1-power(nu12hmg,2));
% C12 = nu12hmg*C11;
% C22 = C11;
% C33 = Ghomog;
% %C33 = Ehomog/(2*(1+nu12hmg));
% C21 = C12;

%PLANE STRESS CONSTITUTIVE DERIVATIVE COEFFICIENTS
% -----

```

```

C11_der1 = ((1-power(nul2hmg,2))*E_der1 - (-
2*nul2hmg*nul2_der1)*Ehomog)/...
power((1-power(nul2hmg,2)),2);
C22_der1 = C11_der1;
C12_der1 = ((1-power(nul2hmg,2))*(nul2hmg*E_der1+Ehomog*nul2_der1) -
...
(-2*power(nul2hmg,2)*nul2_der1*nul2hmg*Ehomog))/power((1-
power(nul2hmg,2)),2);
C33_der1 = G_der1;
C21_der1 = C12_der1;

```

```

% ELEMENT STIFFNESS DERIVATIVE MATRIX
% -----

```

```

K11_der1 = h*(C11_der1*b/(3*a) + C33_der1*a/(3*b));
K12_der1 = h*(C12_der1/4 + C33_der1/4);
K13_der1 = h*(C11_der1*b/(6*a) - C33_der1*a/(3*b));
K14_der1 = h*(-C12_der1/4 + C33_der1/4);
K15_der1 = h*(-C11_der1*b/(3*a) + C33_der1*a/(6*b));
K16_der1 = h*(C12_der1/4 - C33_der1/4);
K17_der1 = h*(-C11_der1*b/(6*a) - C33_der1*a/(6*b));
K18_der1 = h*(-C12_der1/4 - C33_der1/4);
K22_der1 = h*(C22_der1*a/(3*b) + C33_der1*b/(3*a));
K23_der1 = h*(C12_der1/4 - C33_der1/4);
K24_der1 = h*(-C22_der1*a/(3*b) + C33_der1*b/(6*a));
K25_der1 = h*(-C21_der1/4 + C33_der1/4);
K26_der1 = h*(C22_der1*a/(6*b) - C33_der1*b/(3*a));
K27_der1 = h*(-C21_der1/4 - C33_der1/4);
K28_der1 = h*(-C22_der1*a/(6*b) - C33_der1*b/(6*a));
K33_der1 = h*(C11_der1*b/(3*a) + C33_der1*a/(3*b));
K34_der1 = h*(-C12_der1/4 - C33_der1/4);
K35_der1 = h*(-C11_der1*b/(6*a) - C33_der1*a/(6*b));
K36_der1 = h*(C12_der1/4 + C33_der1/4);
K37_der1 = h*(-C11_der1*b/(3*a) + C33_der1*a/(6*b));
K38_der1 = h*(-C12_der1/4 + C33_der1/4);
K44_der1 = h*(C22_der1*a/(3*b) + C33_der1*b/(3*a));
K45_der1 = h*(C21_der1/4 + C33_der1/4);
K46_der1 = h*(-C22_der1*a/(6*b) - C33_der1*b/(6*a));
K47_der1 = h*(C21_der1/4 - C33_der1/4);
K48_der1 = h*(C22_der1*a/(6*b) - C33_der1*b/(3*a));
K55_der1 = h*(C11_der1*b/(3*a) + C33_der1*a/(3*b));
K56_der1 = h*(-C12_der1/4 - C33_der1/4);
K57_der1 = h*(C11_der1*b/(6*a) - C33_der1*a/(3*b));
K58_der1 = h*(C12_der1/4 - C33_der1/4);
K66_der1 = h*(C22_der1*a/(3*b) + C33_der1*b/(3*a));
K67_der1 = h*(-C21_der1/4 + C33_der1/4);
K68_der1 = h*(-C22_der1*a/(3*b) + C33_der1*b/(6*a));
K77_der1 = h*(C11_der1*b/(3*a) + C33_der1*a/(3*b));
K78_der1 = h*(C12_der1/4 + C33_der1/4);
K88_der1 = h*(C22_der1*a/(3*b) + C33_der1*b/(3*a));

```

```

KElStfnsDeriv = [ K11_der1 K12_der1 K13_der1 K14_der1 K15_der1
K16_der1 K17_der1 K18_der1

```

```

        K12_der1 K22_der1 K23_der1 K24_der1 K25_der1
K26_der1 K27_der1 K28_der1
        K13_der1 K23_der1 K33_der1 K34_der1 K35_der1
K36_der1 K37_der1 K38_der1
        K14_der1 K24_der1 K34_der1 K44_der1 K45_der1
K46_der1 K47_der1 K48_der1
        K15_der1 K25_der1 K35_der1 K45_der1 K55_der1
K56_der1 K57_der1 K58_der1
        K16_der1 K26_der1 K36_der1 K46_der1 K56_der1
K66_der1 K67_der1 K68_der1
        K17_der1 K27_der1 K37_der1 K47_der1 K57_der1
K67_der1 K77_der1 K78_der1
        K18_der1 K28_der1 K38_der1 K48_der1 K58_der1
K68_der1 K78_der1 K88_der1];
    ElementNodes(1:4) = Element(i,1:4);
    for nodectr = 1:4
        Ue(2*nodectr-1) = SolV(ElementNodes(nodectr),2);
        Ue(2*nodectr) = SolV(ElementNodes(nodectr),3);
    end
    StrainEnergyDeriv(i) = power(10,5)*Ue*KELStfnsDeriv*Ue';
end

% CALCULATING STRAIN ENERGY
% -----
StrainEnergy = FullDisplV(freedofs,:) '*GlobalStfns(freedofs,freedofs)*
FullDisplV(freedofs,:);
if(StrainEnergy<0)
    StrainEnergy = .0002+rand*0.00005;
end
SolV
min(SolV(:,3))
StrainEnergy
StrainEnergyScaled = StrainEnergy*100000;

fid = fopen('RFnlHomog20x6.txt','w');
for i =NoCells(1)*NoCells(2):-1:1;
    fprintf(fid, '%6.4f\n',r(i));
end

fclose(fid);
%time_fem = toc
end

```

## Matlab Code for Density Computation on Parametric Surface

```

function [RelDen,QPtVal]=
NurbsTrial2_XY_DV2InterpKnotLR(NoC,ZVec,NoCells)

```

```

NoCtrlPts = NoC;
n_x = NoCtrlPts(1) - 1;
n_y = NoCtrlPts(2) - 1;
OrderX = 3;%NoC(1)-1;
OrderY = 3;%NoC(2)-1;
IsoPLines = NoCtrlPts;
NoXKnots = n_x + OrderX + 1;
NoYKnots = n_y + OrderY + 1;

% STORING THE COORDINATES OF THE CONTROL VERTICES OF THE CONTROL NET
% -----
index = 1;
for i = 1:IsoPLines(1)
    for j = 1:IsoPLines(2)
        CtrlNet(index,1) = i-1;
        CtrlNet(index,2) = j-1;
        CtrlNet(index,3) = ZVec(index);
        index = index+1;
    end
end
CtrlGrid = [min(CtrlNet(:,1)) min(CtrlNet(:,2));...
            max(CtrlNet(:,1)) max(CtrlNet(:,2))];
% KNOT VECTOR IN EACH DIRECTION
% -----
% CtrlNet
for i = 1:NoXKnots
    if(i <= OrderX)
        KnotVectorX(i) = 0;
    elseif ((NoXKnots - i) < OrderX)
        KnotVectorX(i) = n_x - OrderX + 2 ;
    else
        KnotVectorX(i) = i - OrderX;
    end
end

end

%KnotVectorX

for i = 1:NoYKnots
    if(i <= OrderY)
        KnotVectorY(i) = 0;
    elseif ((NoYKnots - i) < OrderY)
        KnotVectorY(i) = n_y - OrderY + 2 ;
    else
        KnotVectorY(i) = i - OrderY;
    end
end

end

%KnotVectorY
%getchar = input('knots');

```

```

% GENERATING THE CURVE FOR DIFFERENT PARAMETRIC VALUES
% -----

% COMPUTING THE BASIS FUNCTIONS
% -----
Nbasis = @(ctrx,ordr,u,upb) basis(ctrx,ordr,u,upb,KnotVectorX);
function NCtrxOrdr = basis(ctrx,ordr,u,upb,KnotVector)
    for i_b = ctrx:ctrx+ordr-1
        if(upb ==0)
            if (u >= KnotVector(i_b) && u < KnotVector(i_b+1))
                NCurrentik(i_b,1) = 1;
            else
                NCurrentik(i_b,1) = 0;
            end
        elseif(upb ==1)
            if (u >= KnotVector(i_b) && u <= KnotVector(i_b+1))
                NCurrentik(i_b,1) = 1;
            else
                NCurrentik(i_b,1) = 0;
            end
        end
    end
    for j_b = 2:ordr
        for i_b = ctrx:ctrx+ordr-1-j_b+1
            if((KnotVector(i_b+j_b-1) - KnotVector(i_b)) ~= 0 &&...
                (KnotVector(i_b+j_b) - KnotVector(i_b+1)) ~= 0)
                NCurrentik(i_b,j_b) = (u - KnotVector(i_b))/...
                    (KnotVector(i_b+j_b-1) -
KnotVector(i_b))*NCurrentik(i_b,j_b-1)...
                    + (KnotVector(i_b+j_b) - u)/...
                    (KnotVector(i_b+j_b) -
KnotVector(i_b+1))*NCurrentik(i_b+1,j_b-1);
                elseif((KnotVector(i_b+j_b-1) - KnotVector(i_b)) == 0
&&...
                    (KnotVector(i_b+j_b) - KnotVector(i_b+1))==0)
                    NCurrentik(i_b,j_b)= 0;
                elseif((KnotVector(i_b+j_b-1) - KnotVector(i_b)) == 0)
                    NCurrentik(i_b,j_b) = (KnotVector(i_b+j_b) - u)/...
                        (KnotVector(i_b+j_b) -
KnotVector(i_b+1))*NCurrentik(i_b+1,j_b-1);
                elseif((KnotVector(i_b+j_b) - KnotVector(i_b+1)) == 0)
                    NCurrentik(i_b,j_b) = (u - KnotVector(i_b))...
                        / (KnotVector(i_b+j_b-1) -
KnotVector(i_b))*NCurrentik(i_b,j_b-1);
                end
            end
        end
        NCtrxOrdr = NCurrentik(ctrx,ordr);
    end

Mbasis = @(ctry,ordr,u,upb) basis(ctry,ordr,u,upb,KnotVectorY);

```

```

% COMPUTING THE DATUM PLANE XY POINTS TO EVALUATE FOR CELL DENSITIES
% -----
TNoCellsOneX = NoCells(1);
TNoCellsOneY = NoCells(2);
PlaneZ = 0;
Ctr = 1;

for i = 1:TNoCellsOneX
    for j = 1:TNoCellsOneY
        PlaneXY(Ctr,1) = Ctr;
        PlaneXY(Ctr,2) = (i-1)*(CtrlGrid(2,1) - CtrlGrid(1,1) - 0.4)...
                        / (TNoCellsOneX-1) + 0.2;
        PlaneXY(Ctr,3) = (j-1)*(CtrlGrid(2,2) - CtrlGrid(1,2) - 0.4)...
                        / (TNoCellsOneY-1) + 0.2;

        Ctr = Ctr + 1;
    end
end
% PlaneXY
% getchar = input ('hello');
global QSURFACEZVAL;
%FUNCTION TO COMPUTE COORDINATES FROM BASIS FUNCTIONS
% -----
function [DiffQSurfaceVal]= ComputeCord(parvalue,BND,ActXYval)
    QSurfaceVal = [0 0];
    QSURFACEZVAL = 0;
    %tic
    for i = 1:NoCtrlPts(1)
        N(i) = Nbasis(i,OrderX,parvalue(1,1),BND);
        for j = 1:NoCtrlPts(2)
            M(j) = Mbasis(j,OrderY,parvalue(1,2),BND);
            QSurfaceVal(1,1) = QSurfaceVal(1,1) + CtrlNet(j+(i-
1)*IsoPLines(2),1)*N(i)*M(j);
            QSurfaceVal(1,2) = QSurfaceVal(1,2) + CtrlNet(j+(i-
1)*IsoPLines(2),2)*N(i)*M(j);
            QSURFACEZVAL = QSURFACEZVAL + CtrlNet(j+(i-
1)*IsoPLines(2),3)*N(i)*M(j);
        end
    end
    %time_computecord = toc
    DiffQSurfaceVal = QSurfaceVal- ActXYval;
end
UPPERBNDN = 0;
PtIndx = 1;
options = optimset('Display','off');
timesum =0;
init_x = 0;
init_y = 0;
if (TNoCellsOneX*TNoCellsOneY<100)
for cindex = 1:TNoCellsOneX*TNoCellsOneY
    tic
    QSurfaceXYval(1,1) = PlaneXY(cindex,2);
    QSurfaceXYval(1,2) = PlaneXY(cindex,3);

```

```

%   uwvalue = [0.2 0.2];
init_x = floor(cindex/TNoCellsOneY);
init_y = rem(cindex,TNoCellsOneY);
if(init_y ==0)
    init_x = init_x - 1;
    init_y = TNoCellsOneY;
end
if(init_y==1)
    init_y = 0.05;
end
uwvalue = [0.03+init_x*KnotVectorX(NoXKnots)/(TNoCellsOneX+1)...
           0.03+init_y*KnotVectorY(NoYKnots)/(TNoCellsOneY+1)];

uwvalue =
fsolve(@(uwvalue)ComputeCord(uwvalue,UPPERBNDN,QSurfaceXYval),uwvalue,options);
%   time_fsolve = toc;
%getchar = input('uw');
%   timesum = timesum +time_fsolve;

    if(uwvalue(1,1) == max(KnotVectorX))
        UPPERBNDN = 1;
    else
        UPPERBNDN = 0;
    end

    if(uwvalue(1,2) == max(KnotVectorY))
        UPPERBNDM = 1;
    else
        UPPERBNDM = 0;
    end

    QPtVal(PtIndx,1) = PtIndx;
    QPtVal(PtIndx,2) = QSurfaceXYval(1,1);
    QPtVal(PtIndx,3) = QSurfaceXYval(1,2);
    QPtVal(PtIndx,4) = QSURFACEZVAL;
    Paramroots(PtIndx,1) = PtIndx;
    Paramroots(PtIndx,2) = uwvalue(1,1);
    Paramroots(PtIndx,3) = uwvalue(1,2);
    PtIndx = PtIndx + 1;
end
else

    u_Bnd = 0;
    surf_pt = 1;
    Surfgen_Val(:,1:3) = 0;
    %tic
    GenASurfPDiv = 40;
    for u_param = 0:max(KnotVectorX)/GenASurfPDiv:max(KnotVectorX)
        if(u_param == max(KnotVectorX))

```

```

        u_Bnd = 1;
    end
    w_Bnd = 0;
    for w_param = 0:max(KnotVectorY)/GenASurfPDiv:max(KnotVectorY)
        if(w_param == max(KnotVectorY))
            w_Bnd = 1;
        end
        Surfgen_Val(surf_pt,1:3) = 0;
        for i = 1:NoCtrlPts(1)
            N(i) = Nbasis(i,OrderX,u_param,u_Bnd);
            for j = 1:NoCtrlPts(2)
                M(j) = Mbasis(j,OrderY,w_param,w_Bnd);
                Surfgen_Val(surf_pt,1) = Surfgen_Val(surf_pt,1) +
CtrlNet(j+(i-1)*IsoPLines(2),1)*N(i)*M(j);
                Surfgen_Val(surf_pt,2) = Surfgen_Val(surf_pt,2) +
CtrlNet(j+(i-1)*IsoPLines(2),2)*N(i)*M(j);
                Surfgen_Val(surf_pt,3) = Surfgen_Val(surf_pt,3) +
CtrlNet(j+(i-1)*IsoPLines(2),3)*N(i)*M(j);
            end
        end
        surf_pt = surf_pt + 1;
    end
end
%Surfgen_Val
%time_surggen = toc
Surfgen_pts = surf_pt - 1;
PtIndx = 1;
for cindex = 1:TNoCellsOneX*TNoCellsOneY
    QSurfaceXYVal(1,1) = PlaneXY(cindex,2);
    QSurfaceXYVal(1,2) = PlaneXY(cindex,3);

    for i = 1:GenASurfPDiv+1:Surfgen_pts-GenASurfPDiv
        if((QSurfaceXYVal(1,1)<=Surfgen_Val(i+GenASurfPDiv+1,1))&&
(QSurfaceXYVal(1,1)>=Surfgen_Val(i,1)))
            neighbx(1,1) = Surfgen_Val(i,1);
            neighbx(1,2) = Surfgen_Val(i+GenASurfPDiv+1,1);
        for j = 2:GenASurfPDiv

if((QSurfaceXYVal(1,2)<=Surfgen_Val(j,2))&&(QSurfaceXYVal(1,2)>=Surfgen
_Val(j-1,2)))
            neighby(1,1) = Surfgen_Val(j-1,2);
            neighby(1,2) = Surfgen_Val(j,2);
            FourZpts = [Surfgen_Val(i+j-2,3);Surfgen_Val(i+j-
1,3);Surfgen_Val(i+GenASurfPDiv+1+j-
2,3);Surfgen_Val(i+GenASurfPDiv+1+j-1,3)];
            break;
        end
    end
    break;
end
end
    QPtVal(PtIndx,1) = cindex;

```



```

    QPtVal(PtIndx,2) = QSurfaceXYVal(1,1);
    QPtVal(PtIndx,3) = QSurfaceXYVal(1,2);
    if (neighbx(1,1)==neighbx(1,2))
        bt = 0;
    else
        bt = abs(QSurfaceXYVal(1,1) -
neighbx(1,1))/abs(neighbx(1,1)-neighbx(1,2));
    end
    if (neighbx(1,1)==neighbx(1,2))
        bw = 0;
    else
        bw = abs(QSurfaceXYVal(1,2) -
neighbx(1,1))/abs(neighbx(1,1)-neighbx(1,2));
    end

    QPtVal(PtIndx,4) = (1-bt)*(1-bw)*FourZpts(1,1)+(1-
bt)*bw*FourZpts(2,1)+...
                                bt*(1-bw)*FourZpts(3,1)+
bt*bw*FourZpts(4,1);

    PtIndx = PtIndx + 1;

end
% QPtVal
% getchar = input('hello');
end

%timesum
NoSurfPts = PtIndx - 1;

% PLOTTING THE SURFACE
% -----
index = 1;
for i = 1:NoCtrlPts(1)
    for j = 1:NoCtrlPts(2)

        PlotCPolygon(i,j) = CtrlNet(index,3);
        index = index +1;
    end
end

index = 1;
for i = 1:TNoCellsOneX
    for j = 1:TNoCellsOneY
        PlotBSurface(i,j) = QPtVal(index,4);
        index = index +1;
    end
end

subplot(2,1,1);surf(PlotBSurface);
GTHT = 1*0.965; %CORRESPONDS TO MAX UPPERBOUND DEFINED IN "OPTROUT.M"

```

```

for i = 1:TNoCellsOneX*TNoCellsOneY
    RelDen(i,1) = abs(QPtVal(i,4)/GTHT);
    if(RelDen(i,1)>1)
        RelDen(i,1) = 1;
    elseif(RelDen(i,1)<0.02)
        RelDen(i,1) = 0.02;
    end
end

global RHOVEC;
RHOVEC = RelDen;
End

```

## Matlab Code for Generating Patch and Vertex Information for STLConversion

```

function n=dens2stl(pixel,d,filename,nomirror);
%density matrix to stl conversion
%mat is the density matrix, pixel is pixel length/width(in mm), d is
depth of
%extrusion, if nomirror is 1 then it will not mirror the matrix about
the y axis
%filename should have a '.stl' appended to the end

%example
%mat=[0.4,0.4,0.4;1,0,0.8;0.8,0,0.4;]
%dens2stl(5,3,'test2.stl')
%Author: Charlie Manion 6/22/10
NoCells = [16;10];
fid = fopen('CantiR16x10MMA.txt','r');
x(1:NoCells(2),1:NoCells(1)) =0;
for x_ictr = 1:NoCells(1)
    for x_jctr = 1:NoCells(2)
        x(x_jctr,x_ictr) = fscanf(fid,'%f',[1 1]);
        %x(x_jctr,x_ictr) = sqrt(x(x_jctr,x_ictr));
        fscanf(fid,'\n');
    end
end
fclose(fid);
mat = x;
holemin=0.5;%minimum hole size in mm
holemax=pixel-holemin*2;%maximum hole size in mm
if (ischar(filename)==0)
    error( 'Invalid filename');
end

density1=(pixel^2-holemin^2)/pixel^2;%maximum density
density2=(pixel^2-holemax^2)/pixel^2;%minimum density
input=flipud(mat);

```

```

if exist('nomirror')==0 | nomirror==0
input=[fliplr(input),input];%mirror to make symmetrical
end

s=size(input);

vert=[];
face=[];

clf
for i=s(1,1):-1:1
    for j=s(1,2):-1:1
        dens=input(i,j);
        hole=sqrt(pixel^2-dens*pixel^2);
        if hole<holemin
            hole=0;
        end

        px1=pixel*(j-1);%pixel edge points
        py1=pixel*(i-1);
        px2=pixel*(j-1)+pixel;
        py2=pixel*(i-1)+pixel;
        px=[px1,py1,0; px1,py2,0; px2,py1,0; px2,py2,0; px1,py1,d;
px1,py2,d; px2,py1,d; px2,py2,d];

        for m=1:8
            if findin(px(m,1),px(m,2),px(m,3),vert)==0
                vert=[vert;px(m,1:3)];
            end
            end%find if point already exist in vertex matrix, if it does
            then don't put it in the vertex matrix

            if hole<=holemax & hole>0
                thick=(pixel-hole)/2;
                x=thick+(j-1)*pixel;
                y=thick+(i-1)*pixel;
                h=hole;
                w=h;
                r=[x,y,w,h];
                rectangle('Position', r);
                hx1=(pixel*(j-1))+thick;%hole edge points
                hy1=(pixel*(i-1))+thick;
                hx2=(pixel*(j-1))+thick+hole;
                hy2=(pixel*(i-1))+thick+hole;
                vert=[vert; hx1,hy1,0; hx1,hy2,0; hx2,hy1,0; hx2,hy2,0;
hx1,hy1,d; hx1,hy2,d; hx2,hy1,d; hx2,hy2,d];

                trap1=[hx1,hy2,0; hx1,hy1,0; px1,py1,0; px1,py2,0];%trapezoid
            definitions
            trap2=[hx2,hy2,0; hx2,hy1,0; px2,py1,0; px2,py2,0];

```

```

trap3=[hx2,hy1,0; hx1,hy1,0; px1,py1,0; px2,py1,0;];
trap4=[hx2,hy2,0; hx1,hy2,0; px1,py2,0; px2,py2,0;];
trap5=[hx1,hy2,d; hx1,hy1,d; px1,py1,d; px1,py2,d;];
trap6=[hx2,hy2,d; hx2,hy1,d; px2,py1,d; px2,py2,d;];
trap7=[hx2,hy1,d; hx1,hy1,d; px1,py1,d; px2,py1,d;];
trap8=[hx2,hy2,d; hx1,hy2,d; px1,py2,d; px2,py2,d;];

hole1=[hx1,hy1,0; hx1,hy1,d; hx2,hy1,d; hx2, hy1,0;];
hole2=[hx1,hy2,0; hx1,hy2,d; hx2,hy2,d; hx2, hy2,0;];
hole3=[hx2,hy1,0; hx2,hy1,d; hx2,hy2,d; hx2, hy2,0;];
hole4=[hx1,hy1,0; hx1,hy1,d; hx1,hy2,d; hx1, hy2,0;];%hole
definitions
trap=[trap1; trap2; trap3; trap4; trap5; trap6; trap7; trap8;
hole1; hole2; hole3; hole4];
tri=traptotri(trap);

for k=1:3:size(tri,1)
    tr=[tri(k:k+2,1:3)];
    for v=1:3
        fa(1,v)=findin(tr(v,1),tr(v,2),tr(v,3),vert);
    end

    face=[face; fa(1,1:3)];
end

elseif hole>0
    trap=[];
    if i>1 & input(i-1,j)>density2
        %line([pixel*(j-1),pixel*(j-1)+pixel],[pixel*(i-
1),pixel*(i-1)])
        trap=[trap; px1,py1,0; px1,py1,d; px2,py1,d; px2,
py1,0;];
    end
    if i<s(1,1) & input(i+1,j)>density2
        %line([pixel*(j-1),pixel*(j-
1)+pixel],[pixel*(i),pixel*(i)]);
        trap=[trap; px1,py2,0; px1,py2,d; px2,py2,d;
px2,py2,0;];
    end
    if j>1 & input(i,j-1)>density2
        %line([pixel*(j-1),pixel*(j-1)],[pixel*(i-1),pixel*(i-
1)+pixel]);
        trap=[trap; px1,py1,0; px1,py1,d; px1,py2,d;
px1,py2,0;];
    end
    if j<s(1,2) & input(i,j+1)>density2
        %line([pixel*(j),pixel*(j)],[pixel*(i),pixel*(i)-
pixel]);

```

```

                trap=[trap; px2,py1,0; px2,py1,d; px2,py2,d;
px2,py2,0;];
            end
            tri=traptotri(trap);
            for l=1:3:size(tri,1)
                tr=[tri(l:l+2,1:3)];
                for v=1:3
                    fa(1,v)=findin(tr(v,1),tr(v,2),tr(v,3),vert);
                end
                face=[face; fa(1,1:3)];
            end
        end
        trap=[];
        if hole==0
            trap=[trap; px1,py1,0; px2,py1,0; px2,py2,0; px1, py2,0; px1,py1,d;
px2,py1,d; px2,py2,d; px1, py2,d;];
        end
        if j==s(1,2) & input(i,j)>density2
            %line([pixel*(j),pixel*(j)], [pixel*(i),pixel*(i)-pixel])
            trap=[trap; px2,py1,0; px2,py1,d; px2,py2,d; px2, py2,0;];

        end
        if j==1 & input(i,j)>density2
            %line([pixel*(j-1),pixel*(j-1)], [pixel*(i-1),pixel*(i-
1)+pixel]);
            trap=[trap; px1,py1,0; px1,py1,d; px1,py2,d; px1, py2,0;];
        end
        if i==1 & input(i,j)>density2
            %line([pixel*(j-1),pixel*(j-1)+pixel], [pixel*(i-1),pixel*(i-
1)]);
            trap=[trap; px1,py1,0; px1,py1,d; px2,py1,d; px2, py1,0;];
        end
        if i==s(1,1) & input(i,j)>density2
            %line([pixel*(j-1),pixel*(j-1)+pixel], [pixel*(i),pixel*(i)]);
            trap=[trap; px1,py2,0; px1,py2,d; px2,py2,d; px2, py2,0;];
        end
        tri=traptotri(trap);
        for l=1:3:size(tri,1)
            tr=[tri(l:l+2,1:3)];
            for v=1:3
                fa(1,v)=findin(tr(v,1),tr(v,2),tr(v,3),vert);
            end
            face=[face; fa(1,1:3)];
        end
    end

end

axis equal
grid

```

```
p=patch('Faces', face, 'Vertices', vert, 'FaceColor', 'r')
p=struct('faces', face, 'vertices', vert)
```

```
patch2stl(filename, p, 'ascii')
```

```
function n=findin(x,y,z,vert)
```

```
n=0;
for i=1:size(vert,1)
    if vert(i,1:3)==[x,y,z;]
        n=i;
        break
    end
end
```

```
function tri=traptotri(trap)
tri=[];
for i=1:4:size(trap,1)
    tr=[trap(i:i+3,1:3)];
    tri=[tri; tr(1,1:3); tr(3,1:3); tr(2,1:3); tr(1,1:3); tr(3,1:3);
tr(4,1:3)];
end
```

## APDL Code for Hole Geometry Generation in ANSYS Mechanical 12.1

### *Sample Case – MBB Beam*

```
*Dim, density, array, 120, 1, 1
*vread, density, 120, 1, 1, 'density.txt', (F5.4)
ctr=1
*do, I, 1, 20
    *do, j, 1, 6
x1=5+(i-1)*cellsize+cellsize*(1-sqrt(1-density(120-ctr+1)))/2
x2=x1+cellsize*sqrt(1-density(120-ctr+1))
*enddo
y1=5+(i-1)*cellsize+cellsize*(1-sqrt(1-density(120-ctr+1)))/2
y2=y1+cellsize*sqrt(1-density(120-ctr+1))
retcng, x1, x2, y1, y2
ctr = ctr+1
*enddo
```

## References

- [1] Pham, D. T., & Gault, R. S. (1998, October). A comparison of rapid prototyping technologies. *International Journal of Machine Tools and Manufacture*, 38(10-11), 1257-1287. doi:10.1016/S0890-6955(97)00137-5.
- [2] Yan, X., & Gu, P. (1996, April). A review of rapid prototyping technologies and systems . *Computer-Aided Design*, 28(4), 307-318. doi:10.1016/0010-4485(95)00035-6.
- [3] Kruth, J. P., Leu, M. C., & Nakagawa, T. (1998). Progress in additive manufacturing and rapid prototyping. *CIRP Annals - Manufacturing and Technology*, 47(2), 525-540. doi:10.1016/S0007-8506(07)63240-5.
- [4] Hull, C. W. (1986). *U.S. Patent No. 4,575,330*. Washington, DC: U.S. Patent and Trademark Office.
- [5] Melchels, F., Feijen, J., & Grijpma, D. (2010, August). A review on stereolithography and its applications in biomedical engineering. *Biomaterials*, 31(24), 6121-6130 . doi:10.1016/j.biomaterials.2010.04.050.
- [6] Sachs, E. M., Haggerty, J. S., Cima, M. J., & Williams, P. A. (1993). *U.S. Patent No. 5,204,055*. Washington, DC: U.S. Patent and Trademark Office.
- [7] Weeren, R. V., Agarwala, M., Jamalabad, V. R., & Bandyopadhyay, A. (1995, August). Quality of parts processed by fused deposition. *Proceedings of the 6th Solid Freeform Fabrication Symposium*, 314-321.
- [8] Sachs, E. M., Haggerty, J. S., Cima, M. J., & Williams, P. A. (1993). *U.S. Patent No. 5,204,055*. Washington, DC: U.S. Patent and Trademark Office.
- [9] Dimitrov, D., Beer, K., & De, N. (2006). Advances in three dimensional printing – state of the art and future perspectives. *Rapid Prototyping Journal*, 12(3), 136-147. doi:10.1108/13552540610670717.
- [10] Deckard, C. R. (1989). *U.S. Patent No. 4,863,538*. Washington, DC: U.S. Patent and Trademark Office.
- [11] Agarwala, M., Bourell, D., Beamann, J., Marcus, H., & Barlow, J. (1995). Direct selective laser sintering of metals. *Rapid Prototyping Journal*, 1(1), 26-36. doi:10.1108/13552549510078113.
- [12] Kruth, J., Wang, X., Laoui, T., & Froyen, L. (2003). Lasers and materials in selective laser sintering. *Assembly Automation* , 23(4), 357-371. doi:10.1108/01445150310698652.

- [13] Pham, D. T., Dimov, S., & Lacan, F. (1999). Selective laser sintering: applications and technologies. *Proceedings of the Institution of Mechanical Engineers, Part B: Journal of Engineering Manufacture*, 213(5), 435-449. doi:10.1243/0954405991516912.
- [14] Raghunath, N., & Pandey, P. (2006, May). Improving accuracy through shrinkage modelling by using Taguchi method in selective laser sintering. *International Journal of Machine Tools and Manufacture*, 47(6), 985-995. doi:10.1016/j.ijmachtools.2006.07.001.
- [15] Karapatis, N. P., Egger, G., Gygax, P. E., & Glardon, R. (1999). Optimization of powder layer density in selective laser sintering. *Proceedings of the 9th Solid Freeform Fabrication Symposium*, 255-64.
- [16] Wang, X. (1999). Calibration of shrinkage and beam offset in SLS process. *Rapid Prototyping Journal*, 5(3), 129-133. doi:10.1108/13552549910278955.
- [17] Kruth, J. P., Vandenbroucke, B., Vaerenbergh, J. V., & Mercelis, P. (2005, April). Benchmarking of different SLS/SLM processes as rapid manufacturing techniques. *Proceedings of 1st International Conference of Polymers and Mould Innovations*.
- [18] Choi, S., & Samavedam, S. (2002, January). Modelling and optimization of rapid prototyping. *Computers in Industry*, 47(1), 39-53. doi:10.1016/S0166-3615(01)00140-3.
- [19] Wang, R. J., Wang, L., Zhao, L., & Liu, Z. (2007). Influence of process parameters on part shrinkage in SLS. *The International Journal of Advanced Manufacturing Technology*, 33(5-6), 498-504. doi:10.1007/s00170-006-0490-x.
- [20] Pham, D. T., & Gault, R. S. (1998, October). A comparison of rapid prototyping technologies. *International Journal of Machine Tools and Manufacture*, 38(10-11), 1257-1287. doi:10.1016/S0890-6955(97)00137-5.
- [21] Rosenkrantz, J., & Rosenberg, J. L. (n.d.). *Cell cycle line* [Test pieces using SLS]. Retrieved from <http://design-milk.com/deconstruction-cell-cycle-by-nervous-system/>.
- [22] Faustini, M., Lokhande, M., Crawford, R., Rogers, W., Gitter, A., & Bosker, G. (2001). Finite element structural analysis of prosthesis sockets for below-the-knee amputees manufactured using SLS. *Proceedings of the Solid Freeform Fabrication*, 381-391.
- [23] Seepersad, C. C. (n.d.). *Carolyn Seepersad, Recipient of the International Outstanding Young Researcher in Freeform and Additive Manufacturing Award* [Display of SLS Parts]. Retrieved from [http://www.me.utexas.edu/news/2009/0809\\_seepersad\\_lff\\_award.php](http://www.me.utexas.edu/news/2009/0809_seepersad_lff_award.php).



- [24] Hague, R., Campbell, I., & Dickens, P. (2003). Implications on design of rapid manufacturing . *Proceedings of the Institution of Mechanical Engineers, Part C: Journal of Mechanical Engineering Science*, 217(1), 25-30. doi:10.1243/095440603762554587.
- [25] Crawford, R. H., Beamann, J., Cavello, C., Jackson, J., & Sequin, C. (1999, February). Solid freeform fabrication. *IEEE Spectrum*, 34-45.
- [26] Hutmacher, D. W., Sittering, M., & Risbud, M. V. (2004, July). Scaffold-based tissue engineering: rationale for computer-aided design and solid free-form fabrication systems. *Trends in Biotechnology*, 22(7), 354-362. doi:10.1016/j.tibtech.2004.05.005.
- [27] Cheah, C. M., Chua, C. K., Leong, K. F., & Chua, S. W. (2003). Development of a tissue engineering scaffold structure library for rapid prototyping. part 1: Investigation and classification. *The International Journal of Advanced Manufactuirng Technology*, 21(4), 291-301. doi:10.1007/s001700300034.
- [28] Cheah, C. M., Chua, C. K., Leong, K. F., & Chua, S. W. (2003). Development of a tissue engineering scaffold structure library for rapid prototyping. part 2: Parametric library and assembly program. *The International Journal of Advanced Manufactuirng Technology*, 21(4), 302-312. doi:10.1007/s001700300035.
- [29] *The search for the ultimate military tire* [Hexagonal cell structures for robust tires]. (n.d.). Retrieved from <http://bayourenaissanceman.blogspot.com/2009/05/search-for-ultimate-military-tire.html>.
- [30] Maheshwaraa, U., Seepersad, C., & Bourell, D. (2007). Design and freeform fabrication of deployable structures with lattice skins. *Rapid prototyping journal*, 13(4), 213-225.
- [31] Sypeck, D. J. (2005). Corrugated truss core sandwich structures. *Applied Composite Materials*, 12, 229-246. doi:10.1007/s10443-005-1129-z.
- [32] Bendsoe, M., & Sigmund, O. (Eds.). (2003). *Topology optimization Theory, methods and applications* (2nd ed.). Germany: Springer.
- [33] Seepersad, C. (2004). *A robust topological preliminary design exploration method with materials design applications* (Unpublished doctoral dissertation). Georgia Institute of Technology, Atlanta, Georgia.
- [34] Dorn, W., Gomory, R., & Greenberg, M. (1964). Automatic design of optimal structures. *J. de Mecanique*, 3, 25-52.
- [35] Kirsch, U. (1989, August). Optimal topologies of structures. *Applied Mechanics Reviews*, 42(8), 223-239. doi:10.1115/1.3152429.

- [36] Bendsoe, M., Ben-Tal, A., & Zowe, J. (1994, April). Optimization methods for truss geometry and topology design. *Structural and Multidisciplinary Optimization*, 7(3), 141-159. doi:10.1007/BF01742459.
- [37] Rozvany, G. (Ed.). Shape and layout optimization of structural systems and optimality. *CISM Lecture Notes, No.325*. Vienna: Springer.
- [38] Rozvany, G. (Ed.). (1997). *Topology optimization in structural mechanics*. Italy: Springer-Verlag.
- [39] Bendsoe, M. (1989, December). Optimal shape design as a material distribution problem. *Structural and Multidisciplinary optimization*, 1(4), 193-202.
- [40] Bendsoe, M., & Kikuchi, N. (1988, November). Generating optimal topologies in structural design using a homogenization method. *Computer Methods in Applied Mechanics and Engineering*, 71(2), 197-224. doi:10.1016/0045-7825(88)90086-2.
- [41] Rozvany, G., Zhou, M., & Birker, T. (1992, September). Generalized shape optimization without homogenization. *Structural and Multidisciplinary Optimization*, 4(3-4), 250-252. doi:10.1007/BF01742754.
- [42] Allaire, G., Bonnetier, E., Francfort, G., & Jouve, F. (1997). Shape optimization by the homogenization method. *Numerische Mathematik*, 76(1), 27-68. doi:10.1007/s002110050253.
- [43] Hassani, B., & Hinton, E. (1999). Solution to topology optimization by homogenization. In *Homogenization and structural topology optimization* (pp. 32-64). Springer.
- [44] Sigmund, O. (2001). A 99 line topology optimization code written in Matlab. *Structural and Multidisciplinary Optimization*, 21(2), 120-127. doi:10.1007/s001580050176.
- [45] Svanberg, K. (1987, February). The method of moving asymptotes—a new method for structural optimization. *International Journal for Numerical Methods in Engineering*, 24(2), 359-373. doi:10.1002/nme.1620240207.
- [46] Oshner, S., & Sethian, J. A. (1988, November). Fronts propagating with curvature dependent speed: Algorithms based on Hamilton-Jacobi formulations. *Journal of Computational Physics*, 79(1), 12-49. doi:10.1016/0021-9991(88)90002-2.
- [47] Allaire, G., Jouve, F., & Toader, A.-M. (2002). A level set method for shape optimization. *Comptes Rendus Mathématique*, 334(12), 1125-1130. doi:10.1016/S1631-073X(02)02412-3.
- [48] Norato, J., Bendsoe, M., Haber, R. B., & Tortorelli, D. (2007). A topological derivative method for topology optimization. *Structural and*

*Multidisciplinary Optimization*, 33(4-5), 375-386. doi:10.1007/s00158-007-0094-6.

- [49] Allaire, G., Jouve, F., & Toader, A.-M. (2004, February). Structural optimization using sensitivity analysis and a level set method. *Journal of Computational Physics*, 194(1), 363-393. doi:10.1016/j.jcp.2003.09.032.
- [50] Xie, Y., & Steven, G. (1993, December). A simple evolutionary procedure for structural optimization. *Computers and Structures*, 49(5), 885-896. doi:10.1016/0045-7949(93)90035-C.
- [51] Rozvany, G. (2001). Stress ratio and compliance based methods in topology optimization – a critical review. *Structural and Multidisciplinary Optimization*, 21, 109-119.
- [52] Chapman, C., Saitou, K., & Jakiela, M. (1994, December). Genetic algorithms as an approach to configuration and topology design. *Journal of Mechanical Design*, 116(4), 1005-1012. doi:10.1115/1.2919480.
- [53] Kane, C., & Schoenauer, M. (1996). Topological optimum design using genetic algorithms. *Control and Cybernetics*, 25(5).
- [54] Jakiela, M., Chapman, C., Duda, J., Adewuya, A., & Saitou, K. (2000, June). Continuum structural topology design with genetic algorithms. *Computer Methods in Applied Mechanics and Engineering*, 189(2-4), 339-356. doi:10.1016/S0045-7825(99)00390-4.
- [55] Wang, S., & Tai, K. (2005, September). Structural topology design optimization using genetic algorithms with a bit-array representation. *Computer Methods in Applied Mechanics and Engineering*, 194(36-38), 3749-3770. doi:10.1016/j.cma.2004.09.003.
- [56] Chen, Z., Gao, L., Qiu, H., & Shao, X. (2009, October 16). Combining genetic algorithms with optimality criteria method for topology optimization. *Proceedings of the Fourth International Conference on Bio-Inspired Computing*, 1-6. doi:10.1109/BICTA.2009.5338131.
- [57] Dutta, D., Kikuchi, N., & Papalambros, P. (1992). Project MAXWEL: Towards Rapid Realization of Superior Products. *Proceedings of Solid Freeform Fabrication*, 54-62.
- [58] Johanson, R., Kikuchi, N., Papalambros, P., Prinz, F., & Weiss, L. (1993). Homogenization design and layered manufacturing of lower control arm in project MAXWEL. *Proceedings of the Solid Freeform Fabrication*, 186-192.
- [59] Hollister, S., Maddox, R., & Taboas, J. (2002, October). Optimal design and fabrication of scaffolds to mimic tissue properties and satisfy biological constraints. *Biomaterials*, 23(20), 4095-4103. doi:10.1016/S0142-9612(02)00148-5.

- [60] Seepersad, C., Allen, J., & McDowell, D. (2006, November). Robust design of cellular materials with topological and dimensional imperfections. *Journal of Mechanical Design*, 128(6), 1285-1287. doi:10.1115/1.2338575.
- [61] Wang, H. V., Williams, C., & Rosen, D. W. (2006). Design synthesis of adaptive mesoscopic cellular structures with unit truss approach and particle swarm optimization algorithm. *Proceedings of the solid freeform fabrication*, 433-445.
- [62] Rosen, D. W. (2007). Design for additive manufacturing: A method to explore unexplored regions of the design space. *Proceedings of the solid freeform fabrication*, 402-415.
- [63] Wang, H. V. (2001). *Computer Aided design methods for additive fabrication of truss structure* (Unpublished doctoral dissertation). Georgia Institute of Technology, Atlanta, Georgia.
- [64] Gibson, L., & Ashby, M. (1997). *Cellular solids: Structures and properties* (2nd ed.). Cambridge, United Kingdom: Cambridge University Press. (Original work published 1988).
- [65] Chen, Y., & Wang, S. (2008). Computer aided product design with performance tailored mesostructures. *Computer Aided Design and Applications*, 5(1-4), 565-576.
- [66] Sanchez-Palencia, E. (1983). Homogenization method for the study of composite media. *Mathematics and Statistics*, 985, 192-214. doi:10.1007/BFb0062368.
- [67] Sun, C., & Vaidya, R. (1996). Prediction of composite properties from a representative volume element. *Composites Science and Technology*, 56(2), 171-179. doi:10.1016/0266-3538(95)00141-7.
- [68] Hassani, B., & Hinton, E. (1999). Appendix B. In *Homogenization and structural topology optimization: Theory, practice and software* (p. 229). Springer.
- [69] Hayes, A., Wang, A., Dempsey, B., & McDowell, D. (2004, August). Mechanics of linear cellular alloys. *Mechanics of materials*, 36(8), 691-713. doi:10.1016/j.mechmat.2003.06.001.
- [70] Berkes, U. (1990, December). Efficient optimization of aircraft structures with a large number of design variables. *Journal of Aircraft*, 27(12), 1073-1078.
- [71] Parnas, L., Oral, S., & Cehyan, U. (2003, May). Optimum design of composite structures with curved fiber courses. *Composites Science and Technology*, 63(7), 1071-1082. doi:10.1016/S0266-3538(02)00312-3.
- [72] Rogers, D. (2001). *An introduction to NURBS with historical perspective*. San Diego, CA: Morgan Kaufmann.

- [73] *CADauno at a glance* [B-spline surface]. (n.d.). Retrieved from <http://cadauno.sourceforge.net/features.php>
- [74] Rozvany, G. (1998). Exact analytical solutions for some popular benchmark problems in topology optimization . *Structural and Multidisciplinary Optimization*, 15(1), 42-48. doi:10.1007/BF01197436.
- [75] *Nodal based evolutionary structural optimization* [Illustration of topology optimization]. (n.d.). Retrieved from <http://www.soton.ac.uk/~cedc/posters.html>.
- [76] Lewinski, T., Zhou, M., GI, & Rozvany, G. (1994, May). Extended exact solutions for lest-weight truss layouts - Part I: cantilever with horizontal axis of symmetry. *International journal of mechanical sciences* , 36(5), 375-398. doi:10.1016/0020-7403(94)90043-4.
- [77] Holcombe, S. (n.d.). patch2stl [Computer program]. Retrieved from <http://www.mathworks.com/matlabcentral/fileexchange/20922-patch2stl>
- [78] ANSYS, Inc. (n.d.). ANSYS Mechanical (Version 12.1) [Computer software].
- [79] Gibson, I., Rosen, D., & Stucker, B. (2010). *Additive manufacturing technologies: Rapid prototyping to direct digital manufacturing*. New York: Springer.

## **Vita**

Vikram Gopalakrishnan Sundararajan was born in Madras in the state of TamilNadu in India. He studied at the Vanavani School of Matriculation and graduated from High school in the year of 2003. He completed his Bachelors in Engineering in Mechanical Engineering with a dual major in Information Technology from the College of Engineering Guindy, Anna University, in the year 2008. He entered the Masters program in Mechanical Engineering at The University of Texas at Austin in 2008. He graduated from The University of Texas in 2010.

Permanent address (or email): 1100 E 32<sup>nd</sup> St.

Apt #101

Austin, TX 78722

This thesis was typed by the author.